UNIVERSITY OF CALIFORNIA
RIVERSIDE

Optimized Designs and Materials for Nanostructure Based Solar Cells

A Dissertation submitted in partial satisfaction
of the requirements for the degree of

Doctor of Philosophy

in

Electrical Engineering

by

Qinghui Shao

December 2009

Dissertation Committee:

Dr. Alexander A. Balandin, Chairperson
Dr. Sakhrat Khizroev
Dr. Mihri Ozkan

The Dissertation of Qinghui Shao is approved:

_____

_____

_____

Committee Chairperson

University of California, Riverside

ACKNOWLEDGEMENTS

I would like to express my profound gratitude and appreciation to my research advisor, Dr. Alexander A. Balandin for his consistent guidance, encouragement and support during my PhD study. It is a great experience for me to work with Dr. Balandin on this project. I have been always inspired and amazed by his exceptional perception and dedication to the field of nano-structured semiconductors and devices. I am also grateful for the support of my PhD committee members, Dr Mihri Ozkan and Dr. Sakhrat Khizroev.

I also acknowledge the support and facilities from Center for Nanoscale Science and Engineering, University of California Riverside.

Specifically I would like to thank Dr. Vladimir A. Fonoberov, Dr. Denis L. Nika, and Dr. Dmitri Kotchetkov for their valuable advice and help on the computational method, technical writing and data analysis.

I am thankful to my friends and colleagues, Dr. Irene Calizo, Ms. Suchismita Ghosh, Mr. Guanxiong Liu and other members at Nano-Device Laboratory for their good wishes, valuable discussions, experiment assistance and memorable days shared together.

Finally, I am indebted to my wife and my parents for their extensive support during my study in the United States.

To my dear wife,

Bei

ABSTRACT OF THE DISSERATION

Optimized Design and Materials for Nanostructure Based Solar Cells

by

Qinghui Shao

Doctor of Philosophy, Graduate Program in Electrical Engineering
University of California, Riverside, December 2009
Dr. Alexander A. Balandin, Chairperson

Nanostructure-based solar cells are attracting significant attention as possible candidates for drastic improvement in photovoltaic (PV) energy conversion efficiency. Although such solar cells are expected to be more expensive there is growing need for the efficient and light-weight solar cells in aero-space and related industries. In this dissertation I present results of the theoretical, computational and experimental investigation of novel designs for quantum dot superlattice (QDS) based PV elements and advanced materials for transparent solar cells. In the first part of the dissertation I describe possible implementation of the intermediate-band (IB) solar cells with QDS. The IB cells were predicted to have PV efficiency exceeding the Shockley-Queisser limit for a single junction cell. The parameters of QDS structure have to be carefully tuned to achieve the desired charge carrier dispersion required for the IB operation. The first-principles models were used to calculate the electrical properties and light absorption in QDS. This approach allowed me to determine the dimensions of QDS for inducing the mini-band which plays the role of the IB. Using the detailed balance theory it was determined that the upper-bound PV efficiency of such IB solar cells can be as

high as ~51%. The required QDS dimensions on the basis of InAsN/GaAsSb are technologically challenging but feasible: ~2-6 nm. Using the developed simulation tools I proposed several possible designs of QDS solar cells including one, which combined the benefits of the IB concept and the advanced tandem cell design. The second part of the dissertation presents a study of graphene layers as transparent electrodes for the PV cells. The graphene layers were mechanically exfoliated from bulk graphite and characterized with micro-Raman spectroscopy. It was found that graphene electrodes have good electrical conductivity, which reveals unusual temperature dependence beneficial for the proposed application. The decrease in resistance with temperature was explained by the thermal generation of the electron-hole pairs in the conditions when the carrier mobility is limited by the defect scattering. The final part of the dissertation presents simulation results of electrical current transport in graphene ribbons, which can be used as transparent electrodes or interconnects.

TABLE OF CONTENTS

LIST OF FIGURES

LIST OF TABLES

CHAPTER 1

INTRODUCTION

1.1 Solar energy: renewable and non-polluting alternative

With growing world energy needs and increasing environmental concern nowadays, alternative energy sources taking place of conventional and polluting fossil fuels have attracted more and more research interest. One such alternative is solar energy. Solar energy is renewable energy produced directly by the Sun and used by many traditional ways for centuries. The Sun creates its energy through a thermonuclear process that converts hundred million tons of hydrogen to helium every second. The process creates heat and electromagnetic radiation. The heat remains in the Sun and maintains the thermonuclear reaction. The electromagnetic radiation (including visible light, infrared light, and ultraviolet radiation) streams out into space in all directions. Only a very small fraction of the total radiation produced reaches the Earth, but this energy received by earth in one hour is more than the world uses in a whole year.

The solar energy flux represents the largest energy input into the terrestrial system. Despite its relatively low power density, the solar resource could potentially satisfy the global energy need on its own. The PV industry has grown into a multi-billion dollar business and production of PV modules exceeds hundreds of MWs, surpassed the 1 GW for the first time in 2004 and is expected to reach 3 GW by 2010. The market has been growing at double digit rates over recent years (20 ~ 40% annually).

There are several ways to convert sunlight into useful energy. One method used for many centuries is to convert sunlight into heat, which can then be used for building heating or water heating. Two common examples of solar energy into heat are solar pool heating and solar water heaters. There are also two ways to convert sunlight into electricity. One is solar thermal electricity generation, which uses much of the technology from conventional utility electricity generation. In most utility electricity generation, heat is generated by burning a fuel such as coal or by a nuclear reaction, and this heat is turned into electricity. In solar thermal generating systems, the heat is created by focusing sunlight onto a spot rather than burning fuels, but the remainder of the electricity generation process is the same as conventional utility generation. Another mechanism for converting sunlight into electricity is solar cells. Solar cells are fundamentally different in that they convert sunlight directly into electricity by photovoltaic effect. Solar cells produce direct current power, which could be converted into alternating current power via an inverter. The solar cell is the basic building block of photovoltaic systems. The cell is acting as a diode in the dark and output power to a load connected when charged by Sun. The typical output voltage of a silicon based solar cell is smaller than one volt, corresponding to its bandgap. A solar module consists of a certain amount of cells in series, to generate a larger DC output voltage under standard illumination conditions. The modules can be used independently or connected in parallel and series into an array to output higher voltage and current in the need of various applications. Increasing efforts are directed towards enhancing the performance of solar cells as well as towards reducing their fabrication and installation costs so that these systems can be deployed at a larger

scale. The overall energy conversion efficiency of solar cells increased steadily in the last decade through enhanced photon absorption and charge carrier transport. III-V based photovoltaic devices have some advantages over silicon cells for space applications, e.g. higher efficiencies, better power/weight ratios and better radiation resistance [1-2]. Quantum dot superlattices are proposed in recent years for their inherently high radiation tolerance and power conversion efficiency for outer space applications [3-4]. Continuous development of novel device concepts, materials, and fabrication processes contributes to lowering the cost of solar power and hence to making it more competitive.

1.2 The third generation solar cells

Solar cells may be formed using a p-n junction, a Schottky barrier, or a metal–insulator semiconductor structure based on various semiconductor materials, such as crystalline silicon, amorphous silicon, germanium, III-V compounds, quantum wells and quantum dots structure. III-V compound semiconductor such as gallium arsenide and indium phosphide have near optimum direct energy band gaps, high optical absorption coefficients and good values of minority carrier lifetimes and mobilities making them better materials than silicon for making high efficiency solar cells.

The most developed solar cells are based on the silicon, both in crystalline and polycrystalline form. Despite the low optical absorption coefficient resulting from the indirect bandgap of silicon, the mature of crystal growth and fabrication process of silicon semiconductors ensures well control on minimizing defect density, thus minority carriers generated by photons can diffuse into depletion region without excessive losses

due to non-radiative recombination. Solar cells can also be made of III-V compound semiconductors, e.g., gallium arsenide (GaAs) and indium phosphide (InP). The materials have high optical absorption coefficient due to their direct bandgaps and near optimal bandgap ~1.4 eV for solar energy conversion. But the high cost of the ingots and processing limits their applications. In aim to reduce the production cost, thin film solar cells with only a few microns materials are developed. They can be formed by sequentially depositing thin layers of semiconductor materials on cheap substrates. Most progress has been made using hydrogenated amorphous silicon (α -Si:H), cadmium telluride (CdTe) and the copper gallium indium diselenide (CIGS). All these materials require low cost process and therefore overall cost of production is greatly decreased, but the efficiency is usually lower than that of crystalline solar cell because of their low material quality and high defect densities. Known as the third generation solar cells, novel solar concepts are proposed to further increase the power conversion efficiency using the low-dimensional structures including hot carriers cell, tandem cell, multiple quantum wells (MQW) cell and intermediate band solar cell. III-V quantum dot superlattice based solar cells are proposed because of their promising potentials in high power conversion efficiency application. The intermediate band solar cell (IBSC) pursues the enhancement of efficiency through the absorption of below bandgap energy photons and production of additional corresponding photocurrent without degrading its output voltage. There are two ways to form the intermediate band. One way is impurity band resulting from highly doped impurities in semiconductors. High density of impurities is required to form third energy band. However, the introduction of a large mount of

impurities can degrade the carrier mobility significantly. The other way is by utilizing quantum dot superlattices. Quantum dot technique has been implemented in IBSC due to its advantage of the discrete nature of the carrier density of states in a 0-dimension nano-structure, an essential property for realizing the IB concept. In the QDS-IBSC, the IB arises from the confined electron states in an array of quantum dots. Antonio Luque's research group [5-10] has discussed the mechanisms of photo-generated carriers transport in intermediate band and efficiency enhancement in detail.

1.3 Quantum dot solar cells for efficiency enhancement

Conversion efficiency is one of the most important parameters to optimize for implementing photovoltaic and photochemical cells on large scale. Fig. 1.1 shows the energy band diagram of a simple p-n junction solar cell under illumination. The major photon absorption and energy loss processes are indicated.

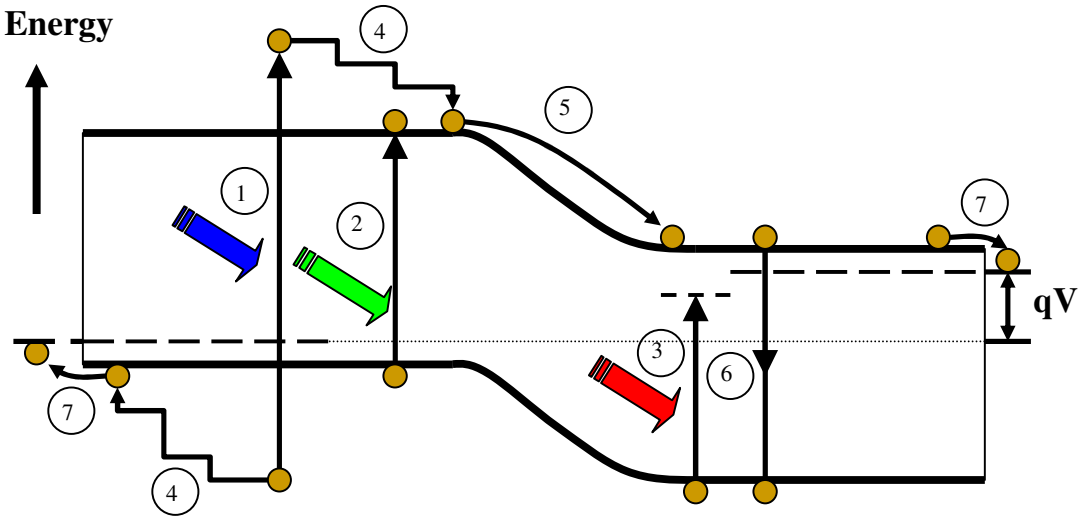

Fig. 1.1 Energy loss in conventional p-n junction solar cell: (1) high energy photon absorption; (2) matching energy photon absorption; (3) low energy photon loss; (4)

thermal relaxation of photo-generated carriers; (5) energy loss by traversing the junction; (6) energy loss by recombination; (7) energy loss at contacts.

During the operation of a standard solar cell, sunlight is absorbed by exciting an electron from valence band to conduction band. Electrons (holes) in conduction (valence) band quickly loss any energy received from high energy photons, in excess of the semiconductor bandgap, and relax back to the edge of conduction (valence) band. There are additional energy losses as the photo-generated carriers cross the junction, traveling in emitter and contact regions (processes 5, 6, and 7 in Fig. 1.1) [11]. Therefore, there exists a strong motivation to investigate new material system and structure design to avoid these losses and improve the device efficiency.

Shockley and Queissar calculated the maximum thermodynamic efficiency to be about 30% for the conversion of unconcentrated solar irradiance into a p-n junction solar cell for an energy gap of 1.1eV in 1961 [12]. To exceed the Shockley-Queissar limit, several design schemes have been proposed. These approaches include tandem cells [13-14], impacting ionization solar cells producing multiple electron-hole pairs per photon [15-16], multiband and impurity-band solar cells [17-18], and quantum dot superlattice cells [19-20].

A major factor limiting the conversion efficiency to 31% is that the absorbed photon energy above the band gap is lost as heat through electron-phonon scattering and subsequent phonon emission. A stack of cascaded multiple junctions with band gap better matched to the solar spectrum has been used to solve this problem. With this approach, the ultimate conversion efficiency at one-sun intensity can be about 66% theoretically.

Another approach used for efficiency purpose is to extract the hot carriers before they relax to band edge via phonon emission. There are two basic ways to achieve that goal. One way aiming at enhanced photo-voltage requires that the carriers be extracted before they cool down. The rates of photo-generated carrier separation and transport must be faster than the rate of carrier cooling. The other way aiming at enhanced photocurrent requires the energetic hot carriers to produce a second or more electron-hole pairs through impact ionization. In this case, the rate of impact ionization must be greater than the rate of carrier cooling and other relaxation processes. Quantization effect in low dimensional structures could help suppress hot carrier's cooling. The quantum well p-i-n solar cell was the first low-dimensional structure proposed by Barnham and Duggan [22] as an alternative to conventional tandem structures to higher conversion efficiency.

QDs are preferred over other low dimensional quantum structures because only QDs provide a true 0-density of states between the confined states and the conduction band. In QWs, due to symmetry selection rules, optical transitions from the confined states to the conduction band are forbidden for light incidence normally on the plane of growth, a highly undesirable feature for a solar cell. The 0-density of states is also believed to prevent quick relaxation of electrons from the conduction band to the confined states [23]. A schematic of the considered supra-crystal structure with the periodically arranged quantum dots is shown in Fig. 1.2. QDS is sandwiched between *p* and *n* type layers. The quantum dots serve as potential well for electrons. The energy levels of an electron in such a well are quantized.

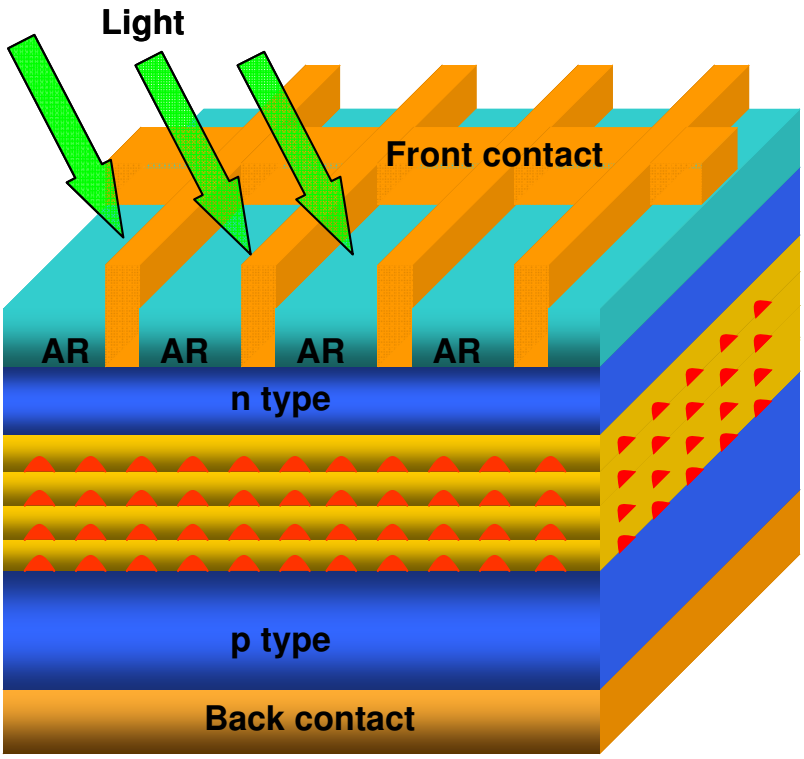

Fig. 1.2 Schematic of quantum dot superlattices based solar cell

The energies of these levels are inversely related to the size of the particles according to the equation (1.1) [24]. Therefore, the size of the particle will indicate the absorbed light energy.

$$\Delta E_g = \frac{h^2}{8d_{QD}^2}\left(\frac{1}{m_e^*}+\frac{1}{m_h^*}\right) \tag{1.1}$$

where ΔE_g is the band gap difference between quantum dot and bulk material, d_{QD} is the diameter of quantum dot, m_e^* and m_h^* are effective mass of electron and hole respectively.

The quantum dots of variable sizes maximize absorption of different light wavelength.

The engineering of the effective band gap (transition energy between the first confined hole level 1h and the first electron level 1e) by tuning dot sizes can be done in a very wide range shown in Figure 1.3. The controlled QD size variation allows one to cover the entire PV light frequency range and tune to the optimum band gap for a given set of parameters.

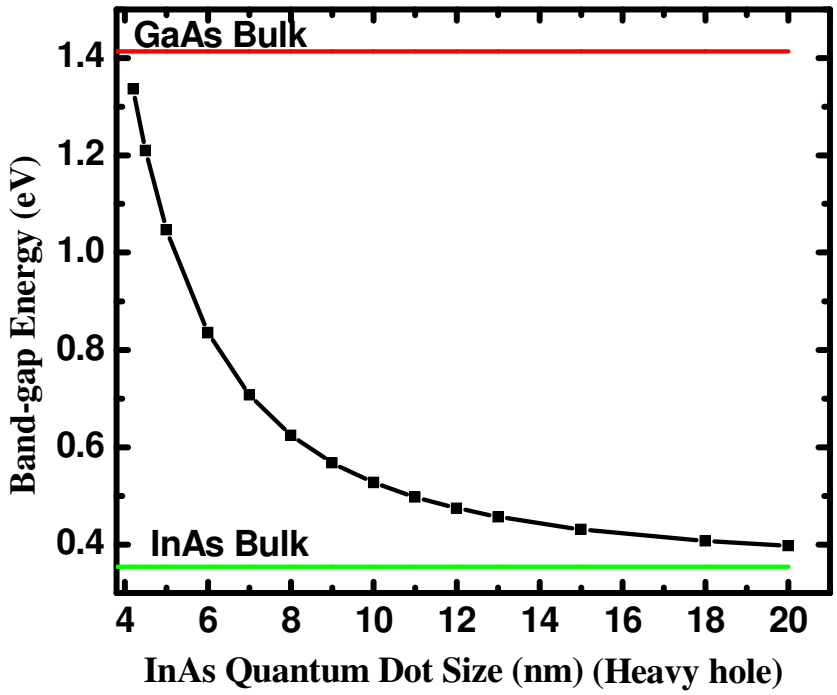

Fig. 1.3 Calculated effective band gap of the QD layers as a function of the dot size

The major photon-generated carrier transport processes are indicated in Fig. 1.4 and Fig. 1.5 for randomly dispersed quantum dots and highly ordered quantum dots respectively.

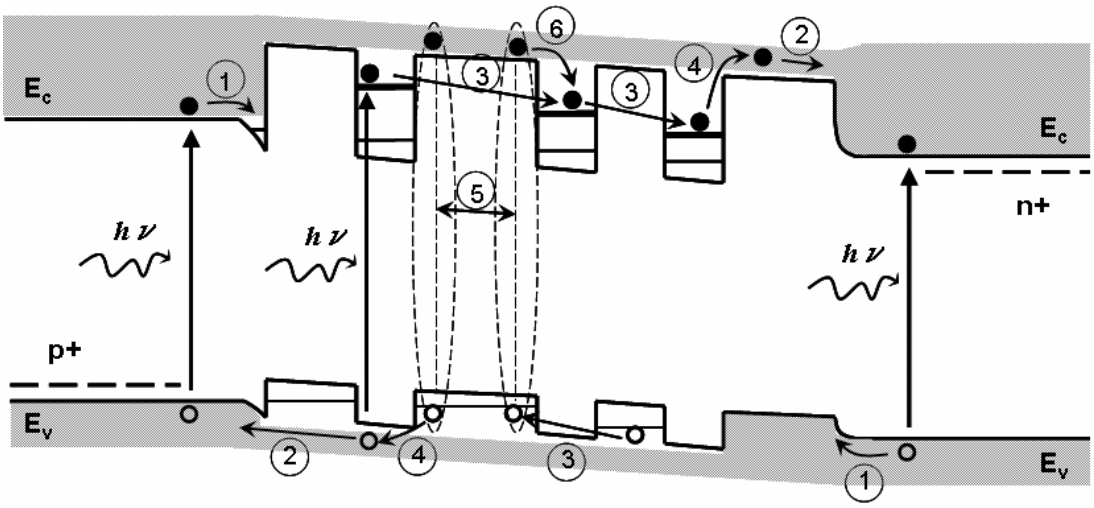

Fig. 1.4 Carrier transport mechanism in randomly dispersed quantum dots: (1) charge carrier diffusion; (2) band type conduction, drift; (3) phonon assisted tunneling (hopping conduction); (4) thermionic emission; (5) exciton diffusion; (6) exciton dissociation

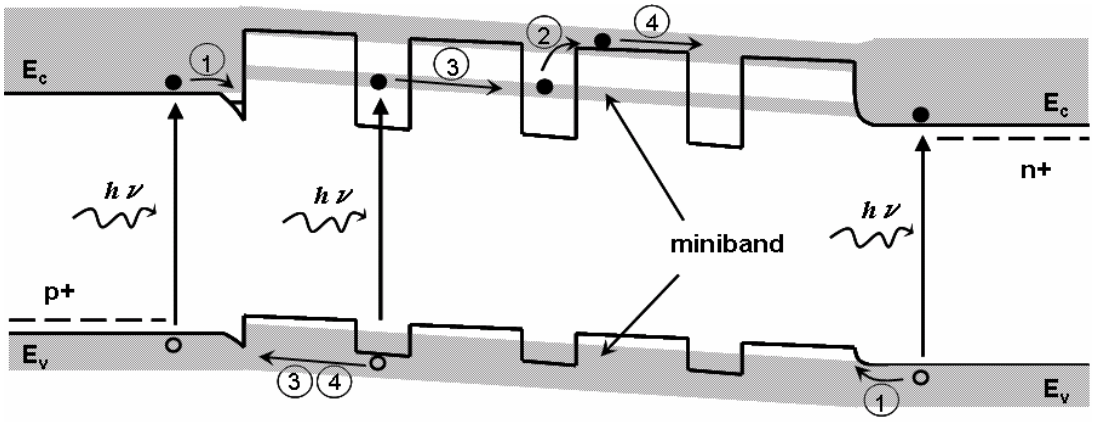

Fig. 1.5 Carrier transport mechanism in high ordered quantum dots: (1) charge carrier diffusion; (2) thermionic emission; (3) mini-band conduction; (4) band type conduction

In highly ordered quantum dot arrays, when the quantum dots are very close, the electron wavefunctions at the neighbor quantum wells are strongly coupling to each other, and overlap to form a third energy level, called mini-band. The mini-band formation can help QDS solar cell to harvest a large portion of photons whose energies are lower than the bandgap of host material. Fig. 1.6 shows the basic optical transitions in QDS solar cell. Low energy photons can be absorbed by two-step process, first excited to miniband in the potential well from valence band, second, excited to conduction band from that miniband. By this way, the output voltage is maintained, and photo-current is increased. Therefore, the overall power conversion efficiency is enhanced.

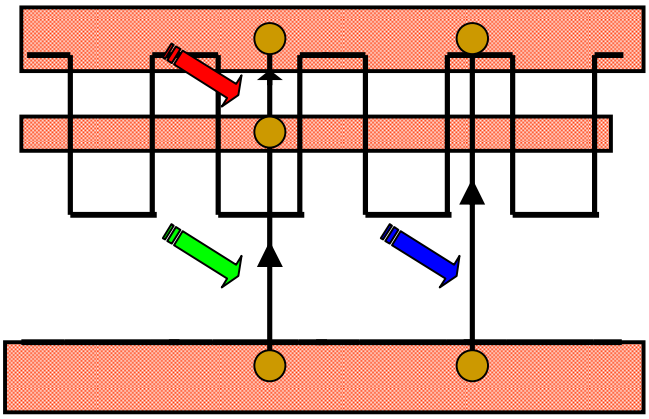

Fig. 1.6 QDS solar cell with enhanced power conversion efficiency

1.4 Quantum dot solar cells for radiation hardness

Space solar cells have been used for power sources by satellites, and played an important role in a wide rang of communications, broadcast, metrological, resource investigation, scientific research and space development applications. The fundamental

objectives for space solar cells are to improve power conversion efficiency, increase BOL (beginning of life) and EOL (end of life), reduce mass, and reduce cost.

In outer-space, the solar cell is struck by fluxes of electrons and protons which are trapped in the electromagnetic field of earth. When slowed down in matter, most of the energy of the incident particles is dissipated by interaction with electron cloud. A relatively small fraction of this energy is dissipated in collision with the nuclei, resulting in the formation of lattice displacement when energy is in excess of some minimum value, e.g. E_d. At high energy, a proton creates simple point defects (interstitials and vacancies, possibly in a multiple form). If these defects are mobile at the irradiation temperature, they may combine or form complexes with impurities present in the semiconductor. The observed damage then depends on temperature, as well as on the impurity composition and content in the semiconductor [25]. Many of the resulting defects introduce energy levels deep into the band gap of the semiconductor, which are effective recombination centers for minority carriers created by light. Thus it provides a shunt path for the electrical current. Minority diffusion length decreasing and recombination current in space charge region are major sources of performance degradation of solar cells.

The radiation tolerance of the QD-based solar cells can be up to two orders of magnitude higher than that of the conventional solar cells which are proved by the study of the influence of electron irradiation on the photoluminescence of InAs/GaAs QD structures [26-27].

Another paper reported by R. Leon et al [28] demonstrated the superior radiation tolerance of QD-related structures (InGaAs/GaAs QDs) over QW-related structures under

proton irradiation by investigating integrated PL intensities from QWs and QDs (normalized to the non-irradiated values) as a function of proton dose. InGaAs QDs are seen to be more radiation tolerant than QWs.

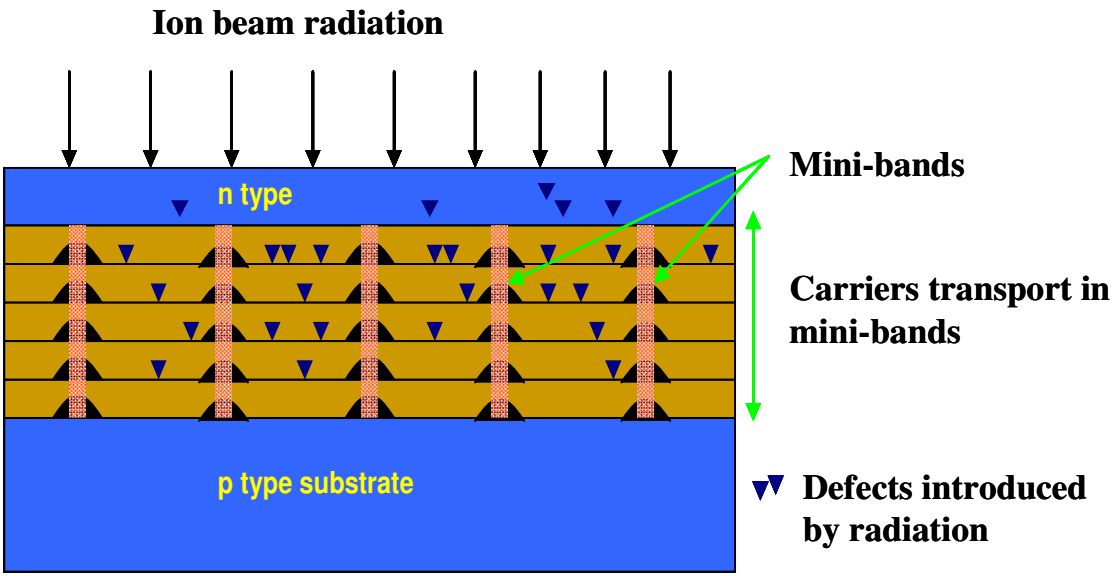

Fig. 1.7 QDS-based solar cell with high radiation tolerance

Exact mechanisms for QD's enhanced radiation hardness are not well known yet. Possible process leading to the quenching of PL intensity upon particle irradiation was proposed by N. A. Sobolev [26]. Photo-generated carriers near defects in the GaAs barrier layers get captured and nonradiative recombined. This process should influence the QWs and QDs to the same extent. However, as shown in Fig. 1.7, the photo-generated carries are highly localized in the quantum dot regime which leaves a very small chance for them to be captured by large amount of defects residing in the host matrix materials. By this way, the radiation tolerance can be readily increased.

References

[1] F. Guffarth, R. Heitz, M. Geller, C. Kapteyn, H. Born, R. Sellin, A. Hoffmann, D. Bimberg, N. A. Sobolev, and M. C. Carmo, "Radiation hardness of InGaAs/GaAs quantum dots," Appl. Phys. Lett. 82, 1941 (2003).

[2] V. V. Ursaki, I. M. Tiginyanu, O. Volciuc, V. Popa, V. A. Skuratov, and H. Morkoc, "Nanostructuring induced enhancement of radiation hardness in GaN epilayers," Appl. Phys. Lett. 90, 161908 (2007).

[3] W. V. Schoenfeld, C. H. Chen, P. M. Petroff, and E. L. Hu, "Argon ion damage in self-assembled quantum dots structures," Appl. Phys. Lett. 73, 2935 (1998).

[4] P. G. Piva, R. D. Goldberg, I. V. Mitchell, D. Labrie, R. Leon, S. Charbonneau, Z. R. Wasilewski, and S. Fafard, "Enhanced degradation resistance of quantum dot lasers to radiation damage," Appl. Phys. Lett. 77, 624 (2000).

[5] L. Cuadra, A. Marti and A. Luque, "Present status of intermediate band solar cell research," Thin Solid Films, 451-452, pp. 593-599 (2004).

[6] A. Marti, L. Cuadra and A. Luque, "Design constrains of the quantum-dot intermediate band solar cell," Physica E, 14, pp. 150-157 (2002) .

[7] L. Cuadra, A. Marti, and A. Luque, "Influence of the overlap between the absorption coefficients on the efficiency of the intermediate band solar cell," IEEE Trans. Electron Devices, 51, 1002 (2004).

[8] A. Luque, A. Marti, C. Stanley, N. Lopez, L. Cuadra, D. Zhou, J. L. Pearson, and A. McKee, "General equivalent circuit for intermediate band devices: Potential, currents and electroluminescence," J. Appl. Phys. 96, 903 (2004).

[9] A. Luque, A. Marti, N. Lopez, E. Antolin, E. Canovas, C. Stanley, C. Farmer, and P. Diaz, "Operation of the intermediate band solar cell under nonideal space charge region conditions and half filling of the intermediate band," J. Appl. Phys. 99, 094503 (2006).

[10] A. Luque, A. Marti, N. Lopez, E. Antolin, E. Canovas, C. Stanley, C. Farmer, L. J. Caballero, L. Cuadra, and J. L. Balenzategui, "Experimental analysis of the quasi-Fermi

level Split in quantum dot intermediate-band solar cells," Appl. Phys. Lett. 87, 083505 (2005).

[11] M. A. Green, "Prospects for photovoltaic efficiency enhancement using low-dimensional structures," Nanotechnology, 11, 401 (2000).

[12] W. Shockley and H. J. Queisser, "Detailed balance limit of efficiency of p-n junction solar cells," J. Appl. Phys. 32, 510 (1961).

[13] J. Yang, A. Banerjee, and S. Guha, "Triple-junction amorphous silicon alloy solar cell with 14.6% initial and 13.0% stable conversion efficiencies," Appl. Phys. Lett. 70, 2975 (1997).

[14] T. Takamoto, E. Ikeda, H. Kurita, and M. Ohmori, "Over 30% efficient InGaP/GaAs tandem solar cells," Appl. Phys. Lett. 70, 381 (1997).

[15] P. T. Landsberg, H. Nussbaumer and G. Willeke, "Band-band impact ionization and solar cell efficiency," J. Appl. Phys. 74, 1451 (1993).

[16] S. Kolodinski, J. H. Werner, T. Wittchen, and H. J. Queisser, "Quantum efficiencies exceeding unity due to impact ionization in silicon solar cells," Appl. Phys. Lett. 63, 2405 (1993).

[17] A. S. Brown, M. A. Green, and R. P. Corkish, "Limiting efficiency for a multi-band solar cell containing three and four bands," Physica E, 14,121-125 (2002).

[18] A. Luque and A. Marti, "Increasing the efficiency of ideal solar cells by photon induced transitions at intermediate levels," Phys. Rev. Lett. 78, 5014 (1997).

[19] A. Alguno, N. Usami, T. Ujihara, K. Fujiwara, G. Sazaki, K. Nakajima, and Y. Shiraki, "Enhanced quantum efficiency of solar cells with self-assembled Ge dots stacked in multilayer structure," Appl. Phys. Lett. 83, 1258 (2003).

[20] V. Aroutiounian, S. Petrosyan, and A. Khachatryan, "Quantum dot solar cells," J. Appl. Phys. 89, 2268 (2001).

[21] K. Barnham and G. Duggan, "A new approach to high-efficiency multi-band-gap solar cells," J. Appl. Phys. 67, 3490 (1990).

[22] A. Marti, N. Lopez, E. Antolin, E. Canovas, C. Stanley, C. Farmer, L. Cuadra and A. Luque, "Novel semiconductor solar cell structures: The quantum dot intermediate band

solar cell," Thin Solid Films, 511-512, 638-644 (2006).

[23] S. Sinharoy, M. O. Patton, T. M. Valko, and V. G. Welzer, "The potential of III-V semiconductors as terrestrial photovoltaic devices," Progr. In Photovoltaics: Res. & Appl. 10, 427 (2002).

[24] J. T. Gudmundsson, H.G. Svavarsson, S. Gudjonsson, H.P. Gislason, "Frequency-dependent conductivity in lithium-diffused and annealed GaAs," Physica B: Condensed Matter 340, 324-328 (2003).

[25] N. A. Sobolev, A. Cavaco, M. C. Carmo, M.Grundmann, F. Hienrichsdorff and D. Bimberg, "Enhance radiation hardness of InAs/GaAs quantum dot structures," Phys. Stat. Sol. (b) 224, No.1, 93-96 (2001).

[26] A. I. Fedoseyev, M. Turowski, Q. Shao, and A. A. Balandin, "Solar cell nanotechnology for improved efficiency and radiation hardness," Proceedings of *SPIE*, Vol. 6308, 630806, August 2006.

[27] R. Leon, G. M. Swift, B. Magness, W. A. Taylor, Y. S. Tang, K. L. Wang, P. Dowd and Y. H. Zhang, "Changes in luminescence emission induced by proton irradiation: InGaAs/GaAs quantum wells and quantum dots," Appl. Phys. Lett. 76, 2074 (2000)

CHAPTER 2

THEORETICAL FORMALISM

2.1 Basics of solar irradiation and solar cells

The irradiance of the sun on the outer atmosphere when the sun and earth are spaced at 1 AU - the mean distance of 149,597,890 kilometer between Sun and Earth - is called the solar constant. The solar constant is the total integrated irradiance over the entire Sun's spectrum.Currently accepted values for solar constant are about 1360 W/m^2. For solar concentration level, it is convenient to describe the irradiance in "suns." One "sun" is equivalent to irradiance of one solar constant. All the radiation that reaches the ground passes through the atmosphere, which modifies the spectrum by absorption and scattering. Atomic and molecular oxygen and nitrogen absorb very short wave radiation, effectively blocking radiation with wavelengths smaller than 190 nm. Ozone strongly absorbs longer wavelength ultraviolet in the band from 200 - 300 nm and weakly absorbs visible radiation. Water vapor, carbon dioxide, and to a lesser extent, oxygen, selectively absorb in the near infrared. The ground level spectrum also depends on how far the Sun's radiation must pass through the atmosphere. AM is defined by the secant of the angle between the sun and the zenith. With the Sun overhead, direct radiation that reaches the ground passes straight through the entire atmosphere, all of the air mass, overhead. This radiation is called "Air Mass 1 Direct" (AM 1.0 D) radiation. The global radiation with the sun overhead is similarly called "Air Mass 1 Global" (AM 1.0 G) radiation. The

outer-space spectrum is called the "Air Mass 0" spectrum because it passes through no air mass, as shown in Fig. 2.1. The atmospheric path for any zenith angle is simply described relative to the overhead air mass. Since the solar spectra depend on so many variables, standard spectra have been developed to provide a basis for theoretical evaluation of the effects of solar radiation. The conditions for the AM 1.5 spectra were chosen as widely used standard spectra for solar cell testing because they are representative of average conditions in the 48 contiguous states of the United States [1].

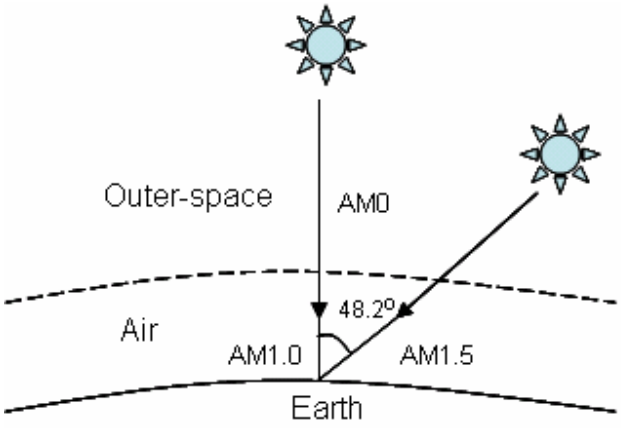

Fig. 2.1 Air mass of solar irradiation

The generated photocurrent in a solar cell under illumination at short circuit is dependent on the incident light wavelength and intensity. The short circuit current can be expressed by equation 2.1

$$J_{sc} = q\int b_s(E)QE(E)dE \tag{2.1}$$

where *QE(E)* is the quantum efficiency, the probability that an incident photon of energy E will deliver one electron to external circui, and $b_s(E)$ is the incident spectral photon

flux density, the number of photons of energy in the range E to $E+dE$ which are incident on unit area in unit time and q is the electronic charge. Quantum efficient is dependent on the absorption coefficient of the material, the efficiency of charge separation and collection. As we know that, for an ideal diode the dark current density $J_{dark}(V)$ is defined as

$$J_{dark}(V) = J_o(e^{qv/k_BT} - 1) \tag{2.2}$$

where J_o is a constant, k_B is Boltzmann's constant and T is the absolute temperature. The overall current of a solar cell under illumination can be approximated as the sum of short circuit current and dark current, which can be expressed as equation (2.3).

$$J_V = J_{sc} - J_{dark}(V) \tag{2.3}$$

When the cell is isolated, the potential difference will reach its maximum, the open-circuit voltage, under a certain level of illumination. This is corresponding to the equivalent condition that the short circuit current is exactly equal to the dark current.

$$V_{oc} = \frac{k_B T}{q} \ln(\frac{J_{sc}}{J_o} + 1) \tag{2.4}$$

The solar cell delivers power in the bias range from 0 to V_{oc}. The out-put power of a cell reachs its maximum at the optimum operating point. This occurs at some voltage V_m with a corresponding current J_m as shown in Fig. 2.2. The fill factor is defined as the ratio of maximum power to the product of open circuit voltage and short circuit current.

$$FF = \frac{J_m V_m}{J_{sc} V_{oc}} \tag{2.5}$$

The cell efficiency is the power density delivered at operating point as a fraction of the total incident light power density, P_s.

$$\eta = \frac{FF \cdot J_{sc} \cdot V_{oc}}{P_s} \tag{2.6}$$

All these four quantities, V_{oc}, J_{sc}, FF, η, are essential parameters for solar cell characterization [2].

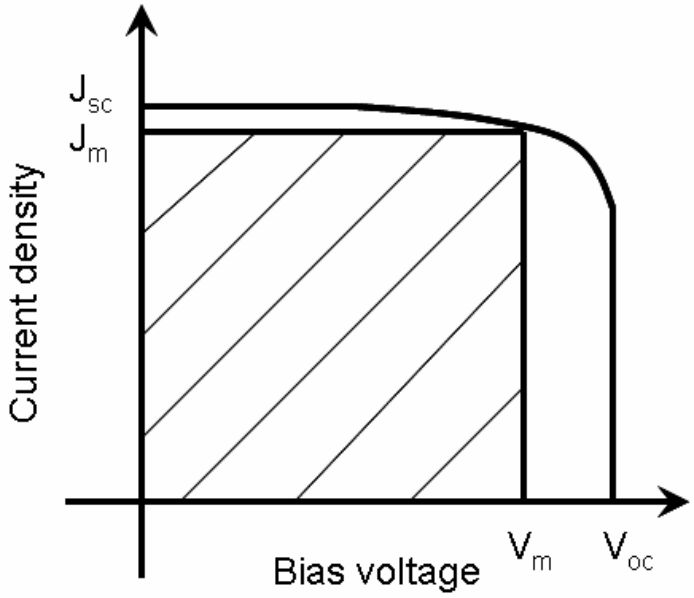

Fig. 2.2 Current-voltage characteristics of an ideal solar cell

2.2 Modeling of quantum dot superlattices

During typical operation of solar cells, there exist two basic processes to convert sunlight power to electrical power. The first one is sunlight absorption and photo-generated Electron-Hole Pairs' (EHP) creation. The second one is the EHP separation and generated carriers transport through or extraction from the device to form

the photo-current. We applied our model to simulate processes of both light absorption and carrier transport in QDS-based solar cell by modulating the dimensions of dot size and dot spacing. The optimum structure of QDS-solar cell is proposed to get the maximum power conversion efficiency over 50% for the given material system (InAsN/GaAsSb). In this part, the electron transport properties are addressed including the energy dispersion, density of states, and electrical conductivity, followed by the photon absorption and efficiency optimization in intermediate band solar cell.

Unlike conduction band and valence band, the third energy level-intermediate band (IB) is not directly electrically contacted, although the radiative transitions between IB and other two bands are allowed. IB helps to harvest photons with the energy less than the bandgap of host material via a two-step process, which allows one to improve the short circuit current without degrading the open circuit voltage. The difficulty of IB approach is how to practically obtain the required exact energy spacing among all three bands. The original proposal of the PV efficiency enhancement via IB and the work that followed assumed that all optimum bands and energy separations are given [3-5]. No semiconductor superlattice structure with exactly defined parameters, which would allow one to implement the IB approach, has been so far specified. In this part, we show that a quantum dot superlattice (QDS) with three-dimensionally (3D) ordered quantum dots can provide the electron and hole energy dispersion, which are suitable for implementing the IB solar cell, and find the exact parameters of QDS required to operate in the IBSC regime.

In order to design and model QDS solar cells, the unique physical and electrical properties of QDS have to be understood. We consider an orthorhombic three dimensionally regimented quantum dot superlattices (Fig. 2.3) and assume that the conditions for formation of the extended minibands are satisfied. The basis of the analysis is the effective mass or envelope function approach [6]. In this approach, the one-electron Schrödinger equation is replaced by an effective mass equation involving the envelope of the electron wave function. The effect of the background atomic potential is interpreted as an effective mass for the electron moving under the influence of macroscopic potential perturbations. The numerical solution scheme can be readily applied to dots of arbitrary geometry. This semianalytical method has already been accomplished by Lazarenkova and Balandin [7-9].

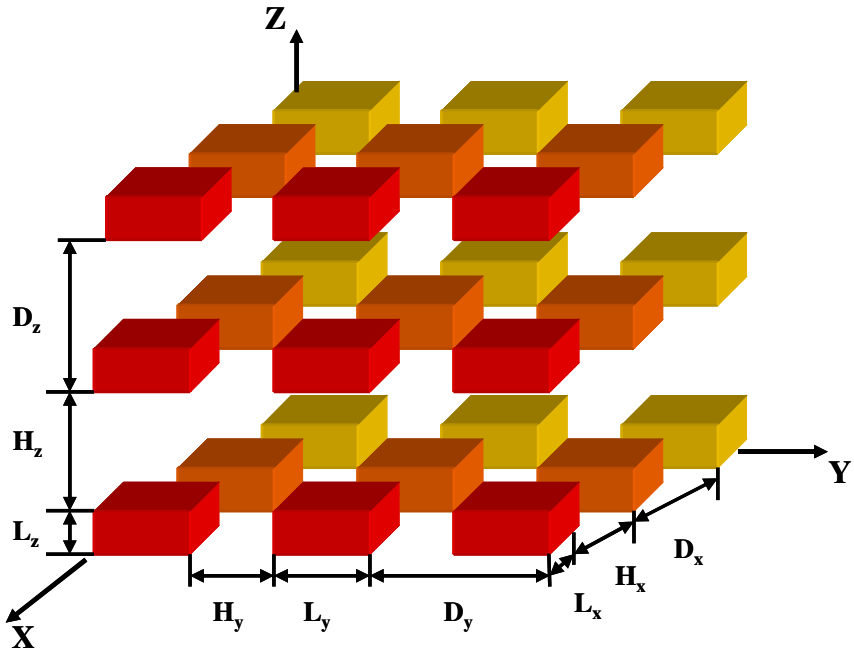

Fig. 2.3 Schematic structure of the orthorhombic quantum dot superlattices

The electron motion in a host crystal experiences the presence of the additional potential $V(\mathbf{r})$. The Schrödinger equation that describes the motion of a charge carrier in such a system can be written in the following form

$$\left[-\frac{\hbar^2}{2}\nabla_{\mathbf{r}}\frac{1}{m^*(\mathbf{r})}\nabla_{\mathbf{r}}+V(\mathbf{r})\right]\varphi(\mathbf{r})=E\varphi(\mathbf{r}) \quad . \tag{2.7}$$

where $m^*(r)$ is the effective mass tensor, E is the total energy, and $\varphi(r)$ is the envelop function of the electron. $V(r)$ is the microscopic potential perceived by the electron, corresponding to the potential change from the change of material composition of the structure. The potential $V(\mathbf{r})$ corresponds to an infinite sequence of quantum dots of size L_x, L_y, and L_z separated by the barriers of thickness H_x, H_y, and H_z shown in Fig. 2.3. We assume that it is written as a sum of three independent periodic functions of coordinates x, y, and z with periods of d_x, d_y, and d_z ($d_\xi = L_\xi + H_\xi$) so that

$$V(\mathbf{r}) = V_x(x) + V_y(y) + V_z(z), \tag{2.8}$$

where

$$V_\xi(\xi)=\begin{cases}0 & if \quad \left|\xi-\eta_\xi d_\xi\right|\le L_\xi/2\\ V_0 & if \quad \left|\xi-\eta_\xi d_\xi\right|> L_\xi/2\end{cases}, \tag{2.9}$$

where η_ξ are the integer numbers and subscript ξ denotes a particular coordinate axis. Fig. 2.4 shows the two-dimensional potential distribution. Inside quantum dot, the potential is zero. Potential V_0 and $2V_0$ are found between dots and at the corner of dots respectively. This choice of potential allows us to separate the carrier motion along three coordinate axes. The three-dimensional Schrödinger equation decouples in this case into

three identical one-dimensional quantum-well superlattice equations. The 3D envelope wave function $\varphi(\mathbf{r})$ is therefore can be presented as a product of three one-dimensional eigenfunctions χ_ξ in the following way

$$\varphi(r) \equiv \varphi_{n_x,n_y,n_z}(x,y,z) = \chi_{n_x}(x)\chi_{n_y}(y)\chi_{n_z}(z), \tag{2.10}$$

where n_ξ denote the quantum number. The total energy spectrum for this wave function is given by

$$E_{n_x n_y n_z} = E_{n_x} + E_{n_y} + E_{n_z}. \tag{2.11}$$

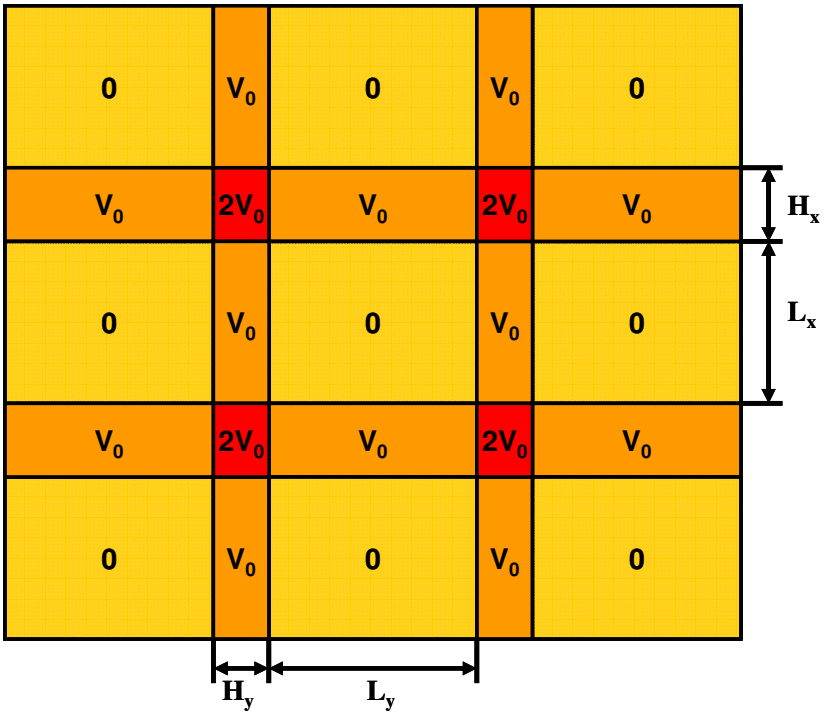

Fig. 2.4 Two dimensional model of potential distribution

For the chosen geometry of QDS and band offsets the carrier wave functions and energy spectrum are mostly determined by the nearest-neighbor interaction between dots separated by the potential barrier V_0. The corner potentials induce only minor corrections,

which are particularly small for the below-the-barrier states. Thus, the solution for the given potential of equations (2.8-2.9) presents a very good approximation for more realistic QDS potentials with the constant barrier height. The more accurate modeling and calculation for higher-index minibands are addressed by D.L. Nika et al [10].

The solution of equation (2.7) with the potential of equations (2.8-2.9) has the Kronig-Penny-like form

$$\cos\left(q_\xi d_\xi\right)=\cos\left(k_\xi^W L_\xi\right)\cos\left(k_\xi^B H_\xi\right)- \frac{1}{2}\left(\frac{k_\xi^B m_W^*}{k_\xi^W m_B^*}+\frac{k_\xi^W m_B^*}{k_\xi^B m_W^*}\right)\sin\left(k_\xi^W L_\xi\right)\sin\left(k_\xi^B H_\xi\right) \quad \text{if} \quad E_\xi \geq V_0, \tag{2.12,a}$$

$$\cos\left(q_\xi d_\xi\right)=\cos\left(k_\xi^W L_\xi\right)\cosh\left(k_\xi^B H_\xi\right)- \frac{1}{2}\left(-\frac{k_\xi^B m_W^*}{k_\xi^W m_B^*}+\frac{k_\xi^W m_B^*}{k_\xi^B m_W^*}\right)\sin\left(k_\xi^W L_\xi\right)\sinh\left(k_\xi^B H_\xi\right) \quad \text{if} \quad 0 < E_\xi < V_0, \tag{2.12,b}$$

where

$$k_\xi^B=\frac{\sqrt{2m_B^*\left|E_\xi - V_0\right|}}{\hbar}, \qquad k_\xi^W=\frac{\sqrt{2m_W^*\left|E_\xi\right|}}{\hbar}. \tag{2.13}$$

The effective masses m^*_B and m^*_W used in equations (2.12-2.13) depend on the crystallographic orientation of the quantum dot interfaces. These equations allow us to calculate the carrier dispersion relation in QDS. Since for each given value of q_ξ there are infinite solutions, we use the mini-band index n_ξ to label the carrier energy.

Reference

[1] ***http://www.newport.com/Introduction-to-Solar-Radiation/411919/1033/catalog.aspx***

[2] Jenny Nelson, The physics of solar cells, page 7, chapter 1, Imperial College Press; 1 edition (September 5, 2003)

[3] M. A. Green, "Prospects for photovoltaic efficiency enhancement using low-dimensional structures," Nanotechnology, 11, 401 (2000).

[4] A. S. Brown, M. A. Green, and R. P. Corkish, "Limiting efficiency for a multi-band solar cell containing three and four bands," Physica E, 14,121-125 (2002).

[5] A. Luque and A. Marti, "Increasing the efficiency of ideal solar cells by photon induced transitions at intermediate levels," Phys. Rev. Lett. 78, 5014 (1997).

[6] G. Bastard, "Theoretical investigation of superlattice band structure in the envelop-function approximation," Phys. Rev. B 25, 7584 (1982).

[7] O. L. Lazarenkova, and A. A. Balandin, "Miniband formation in a quantum dot crystal," J. Appl. Phys. 89, 5509 (2001).

[8] O. L. Lazarenkova, and A. A. Balandin, "Electron and phonon energy spectra in a three-dimensional regimented quantum dot superlattice," Phys. Rev. B 66, 245319 (2002).

[9] O. L. Lazarenkova, and A. A. Balandin, "Quantum dot crystals: Electron band structure and electrical conductivity," Proceedings of Electrochemical Society, 19, pp. 238-250 (New Jersey, 2001).

[10] D. L. Nika, E. P. Pokatilov, Q. Shao, and A. A. Balandin, "Charge carrier states and light absorption in the ordered quantum dot superlattices," Phys. Rev. B. 76, 125417 (2007).

CHAPTER 3

DESIGN, RESULTS AND DISCUSSION

3.1Electrical properties of InAs/GaAs QDS

3.1.1 Energy dispersion relation

We carried out the analysis of the 3D minibands in the QDS of InAs/GaAs system, because the InAs/GaAs systems are most widely used for the application of high efficiency solar cells [1-5]. The conduction band offset for electron is about 0.45eV, and we used the following values for effective masses $m^*_{InAs} = m^*_W = 0.04m_0$ and $m^*_{GaAs} = m^*_B = 0.0665m_0$ where m_0 is the electron rest mass. The Fig. 3.1, Fig. 3.2 and Fig. 3.3 show the dispersion relation in the cubical InAs/GaAs QDS structure along [[100]], [[110]], and [[111]] quasi-crystallographic directions respectively. The energy level in units of eV is counted from the bottom of the electron potential well. The dot size is $L_x = L_y = L_z = 10nm$ and the inter-dot distance is $H_x = H_y = H_z = 5nm$. The carrier wave vector is denoted by q with subscript showing the particular quasi-crystallographic direction. The energy bands are specified by three quantum numbers $n_x\ n_y\ n_z$ with the superscript indicating the degeneracy of the band. The spin degeneracy is not counted. The highest, sixfold, degeneracy is achieved in miniband 123 along [[111]] quasi-crystallographic direction. It is accomplished when both the quantum dot sizes and inter-dot distances are equal along all three axes.

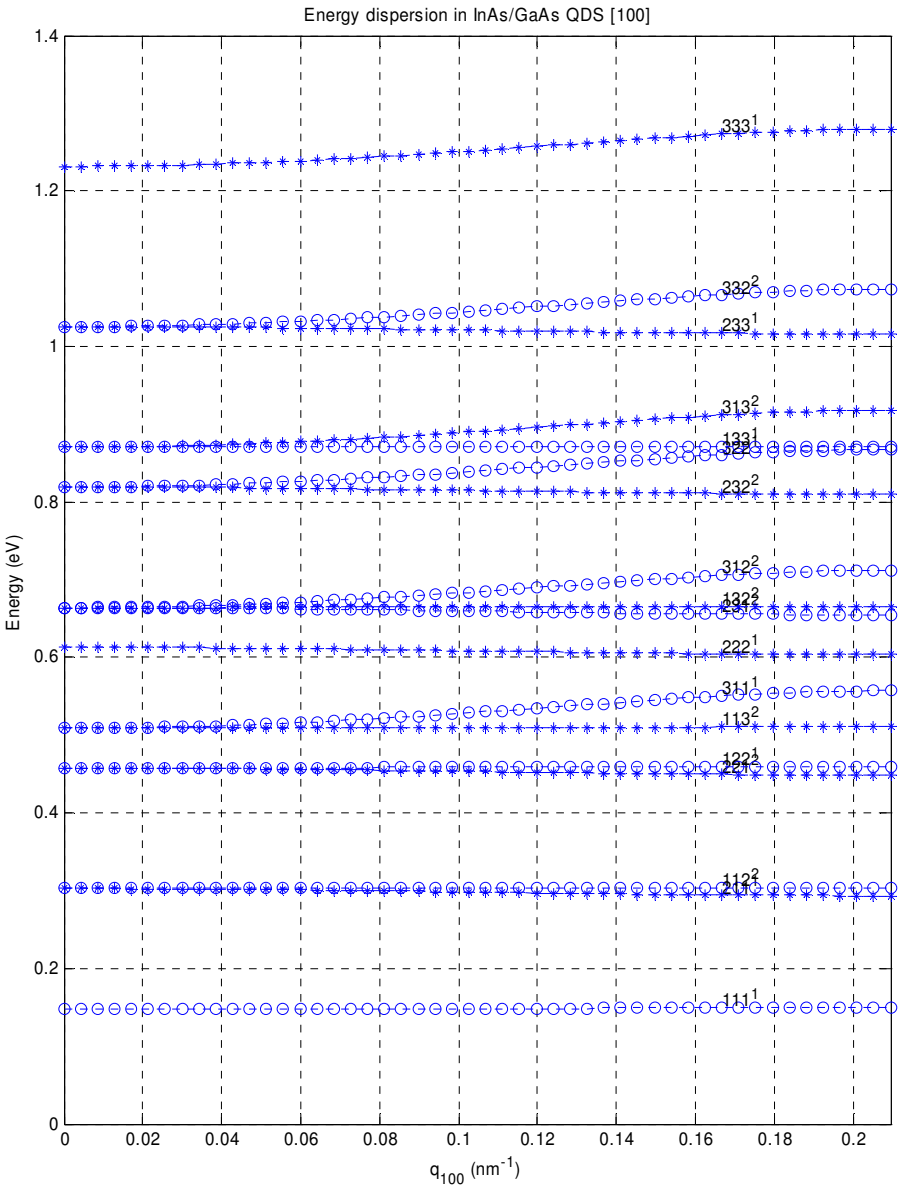

Fig. 3.1 Electron dispersion relation of a cubic QDS of InAs/GaAs along [[100]] quasi-crystallographic direction

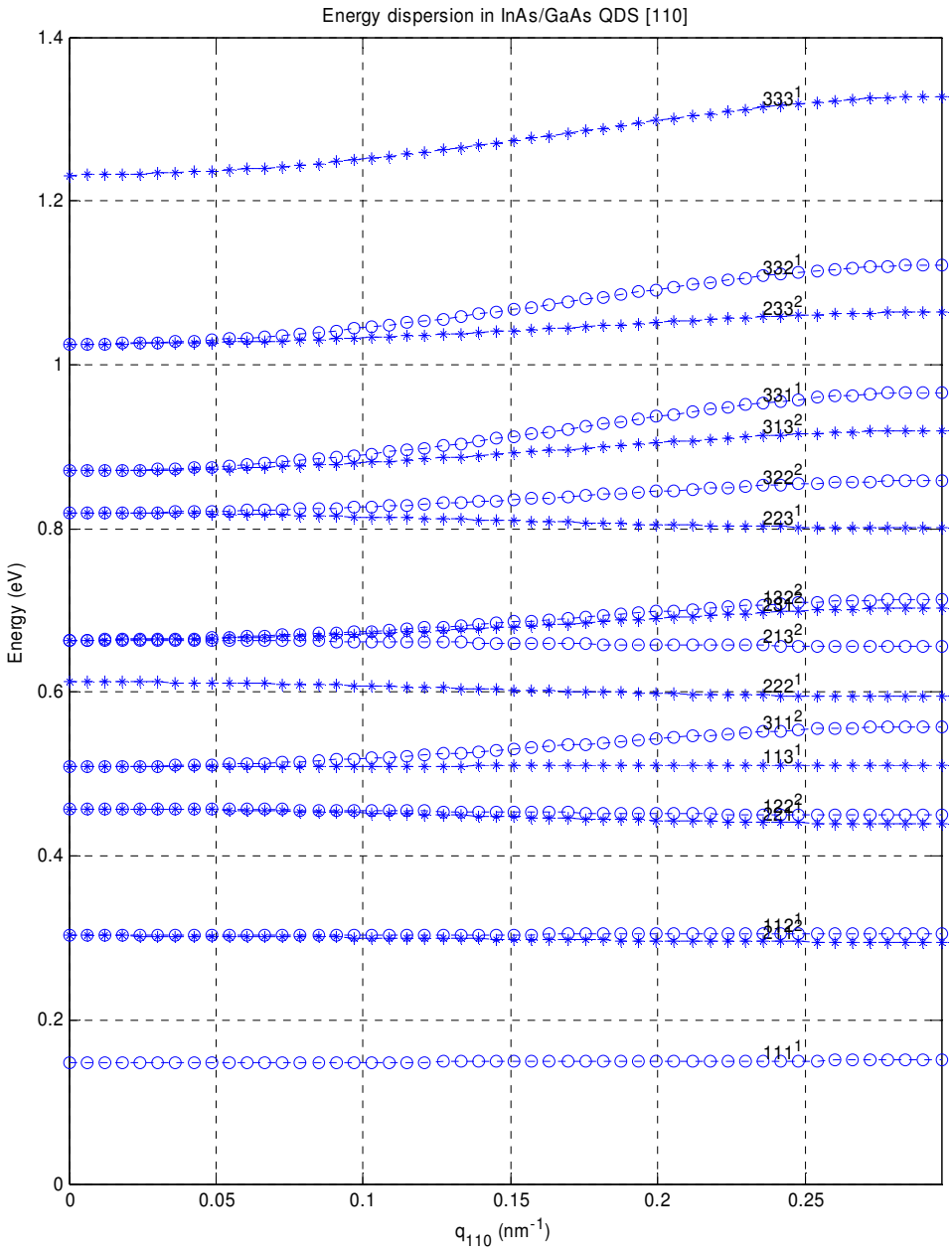

Fig. 3.2 Electron dispersion relation of a cubic QDS system of InAs/GaAs along [[110]] quasi-crystallographic direction

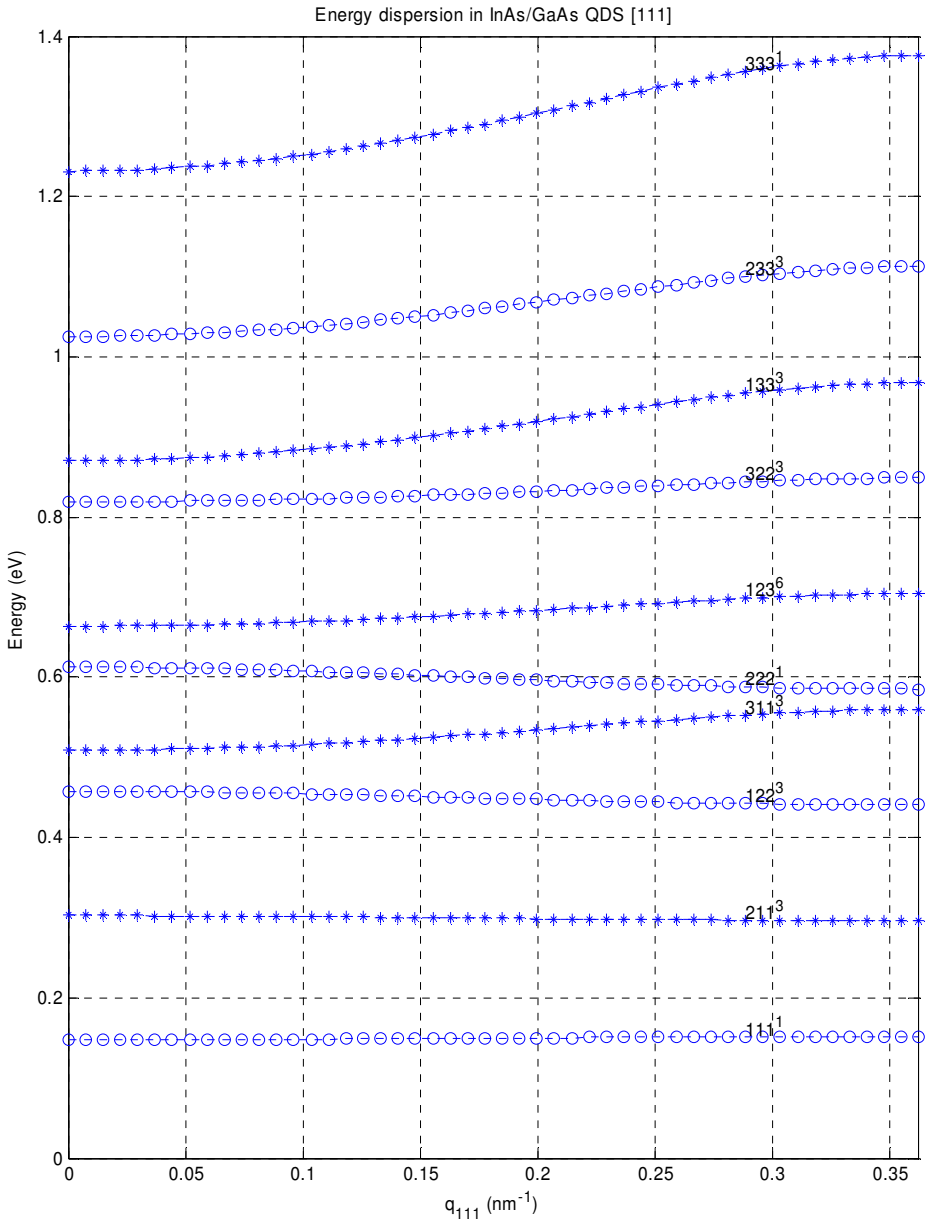

Fig. 3.3 Electron dispersion relation of a cubic QDS system of InAs/GaAs along [[111]] quasi-crystallographic direction

3.1.2 Miniband formation

When quantum dots are brought closely to each other, the electron wave functions in the neighbor wells will couple strongly, and minibands are formed. Fig. 3.4 and Fig. 3.5 show the effect of inter-dot distance and dot size on the bandwidth and energy level in InAs/GaAs QDS, respectively. It is apparent that inter-dot distance is an important parameter in controlling the bandwidth, and the dot size has greater influence on the band energy level rather than the bandwidth. The effect of barrier height on bandwidth and band energy level is illustrated in Fig. 3.6. It shows that the lower barrier height produces broader bands. The band energy level is not sensitive to the barrier height in the range of 0.4 ~ 0.5 eV. It is more sensitive to the change in dot size.

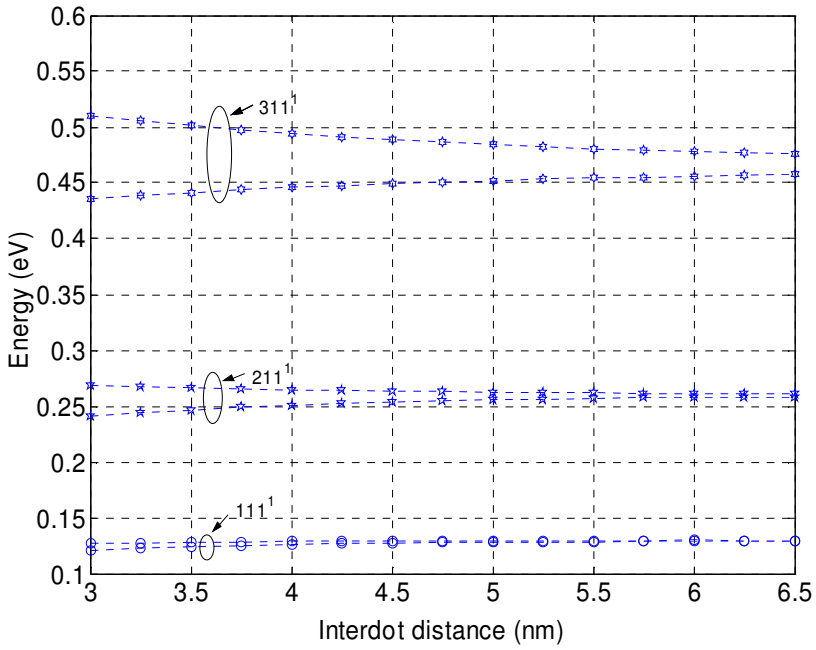

Fig. 3.4 Effect of inter-dot distance on bandwidth and energy level with 10 nm dot size

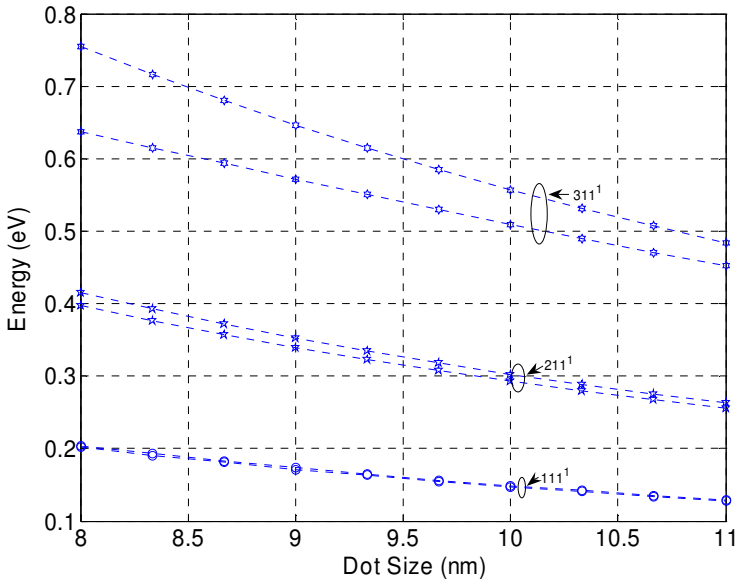

Fig. 3.5 Effect of dot size on bandwidth and energy level with 5 nm dot spacing

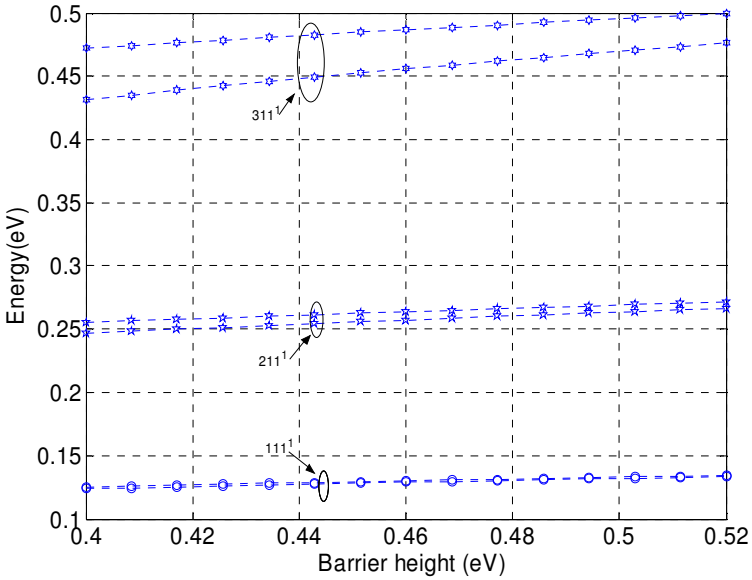

Fig. 3.6 Effect of barrier height on bandwidth and energy level with 10 nm dot size and 5nm dot spacing

3.1.3 Electron Density of States

The density of states, which is a number of carrier states allowed per unit volume per unit energy interval, is an important parameter for electrical and optical applications of semiconductor structures. Mathematically it is give by

$$DOS(E) = \frac{2}{(2\pi)^3} \int_v \delta(E - E_n(\vec{q}))d\vec{q} \tag{3.1}$$

where the integration is carried over the whole Brillouin zone. The factor means the twofold electron spin. Fig. 3.7 (a)-(d) present the electron density of states for the corresponding minibands. The shape of DOS is defined by the relation of three quantum numbers. The ones shown in Fig. 3.7 (a) and (b) correspond to quantum numbers $n_x = n_y = n_z$ and $n_x = n_y < n_z$, $n_x > n_y = n_z$, or $n_x = n_z < n_y$ respectively; while the ones in Fig. 3.7 (c) and (d) correspond to quantum numbers $n_x = n_y > n_z$, $n_x < n_y = n_z$, or $n_x = n_z > n_y$ and $n_x \neq n_y \neq n_z$ respectively. Notice that the areas under each DOS curve, i.e. integral of each DOS over energy range, are all same and approximately equal to two times dot density theoretically. The obtained DOS is drastically different from those in conventional quantum well superlattices or single quantum dot.

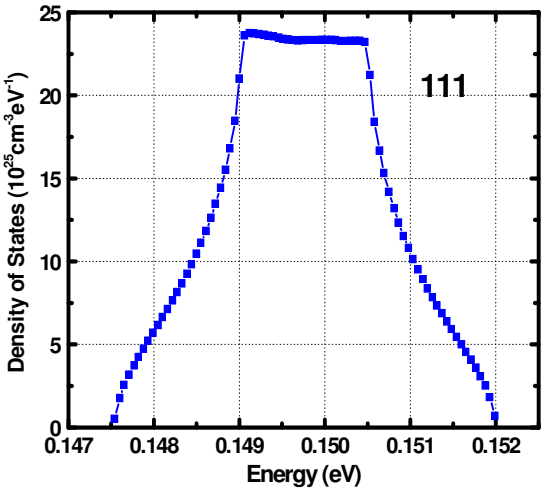
111
Density of States (10^{25}cm^{-3}eV^{-1})
Energy (eV)
0
5
10
15
20
25
0.147
0.148
0.149
0.150
0.151
0.152

(a)

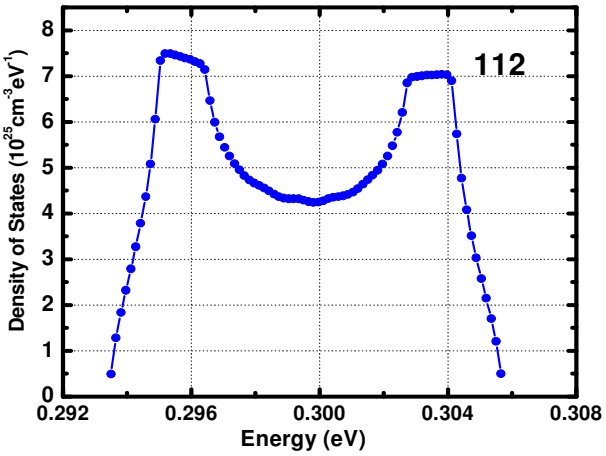
112
Density of States (10^{25}cm^{-3}eV^{-1})
Energy (eV)
0
1
2
3
4
5
6
7
8
0.292
0.296
0.300
0.304
0.308

(b)

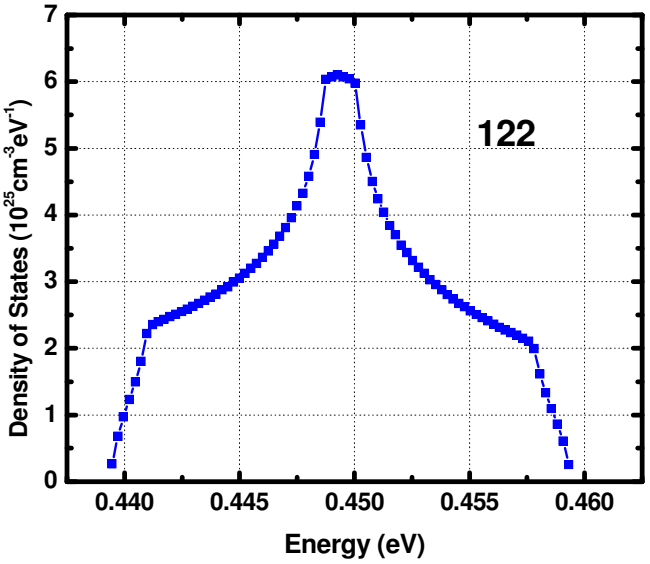

(c)

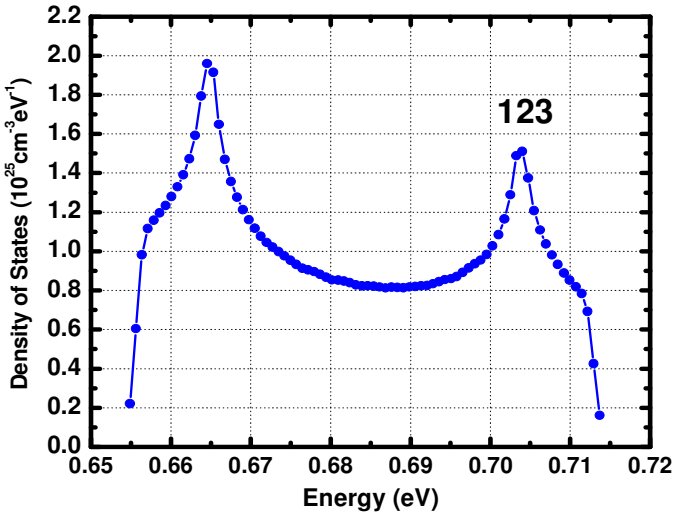

(d)

Fig. 3.7 DOS in a cubical InAs/GaAs QDS for minibands (a) 111, (b) 112, (c)122, and (d) 123, respectively. The dot size is 10nm and inter-dot distance is 5 nm.

3.1.4 Electrical conductivity

We calculate the conductivity tensor of InAs/GaAs QDS by taking into account contributions of all mini-bands in the conduction band of the structure

$$\boldsymbol{\sigma} = \sum_{n} \boldsymbol{\sigma}^{(n)}, \tag{3.2}$$

where the tensor components are given by

$$\sigma_{ij}^{(n)} = \frac{e^2 \tau_0}{4\pi^3 k_B T} \int_{QBZ} v_i^{(n)}(\mathbf{q}) v_j^{(n)}(\mathbf{q}) \frac{\exp\left[\dfrac{E^{(n)}(\mathbf{q}) - E_F}{k_B T}\right]}{\left\{\exp\left[\dfrac{E^{(n)}(\mathbf{q}) - E_F}{k_B T}\right] + 1\right\}^2} d\mathbf{q}. \tag{3.3}$$

where e is the charge of an electron, k_B is the Boltsman constant, T is the temperature, $\mathbf{v}^{(n)}$ is the group velocity vector, E_F is Fermi's energy of an electron, and $\mathbf{q}$ is the electron wave vector. Index n indicates a particular mini-band. The integration in Eq. (3.3) is carried over the whole Quasi Brillouin Zone (QBZ). For simplicity we assume that the relaxation time τ_0 is constant and equal to a value characteristic for given materials, e.g., $\tau_0 = 10^{-12}$ sec [6]. Since the relaxation time is limited at room temperature by optical and acoustic phonon scattering this assumption is rather accurate as a first approximation. From Eq. (3.3) one can see that electron dispersion and the position of Fermi level determine the electrical conductivity tensor. The electron group velocity that explicitly enters Eq. (3.3) is defined by the mini-band structure and electron dispersion in QDS. In general, the components of carrier velocity $\mathbf{v}^{(n)}$ in the n-th subband are written as

$$v_i^{(n)}(\mathbf{q}) = \frac{1}{\hbar} \frac{\partial E^{(n)}(\mathbf{q})}{\partial q_i}. \tag{3.4}$$

where $E^{(n)}$ are eigenvalues of the one-dimensional Schrodinger's equation. In the case of cubical symmetry the relation has $\sigma_{xx}=\sigma_{yy}=\sigma_{zz}$. In order to calculate components of the electrical conductivity tensor, we have to determine group velocity from the energy dispersion relation first. One can see that the group velocity is strongly dependent on the miniband index show in Fig. 3.8. The group velocity increases as miniband index increases at the same electron wave vector.

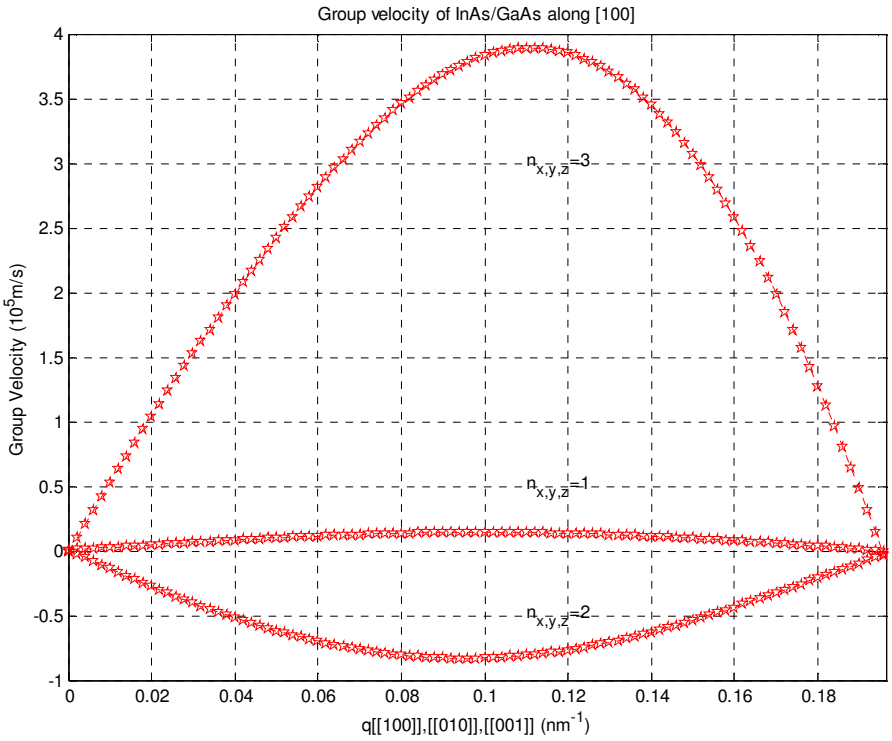

Fig. 3.8 Electron group velocity in InAs/GaAs QDS along quasi-crystallographic direction [[001]]

The low field electrical conductivity from the individual miniband as a function of quasi-Fermi energy is presented in Fig. 3.9. Comparing this figure with Fig. 3.1, one can see that the conductivity peak appears when the quasi-Fermi level is aligned to the corresponding miniband. Therefore, one can make appropriate δ doping in the host

material to achieve a good conductivity to assist the carrier transport in the miniband. In our device structure, we need align the quasi-Fermi level to the fist miniband 111, because other bands have to be squeezed out of the potential well to increase the light absorption coefficient. Adding up all the components of individual bands, the total electrical conductivity is obtained shown in Fig. 3.10. The nonlinear behavior (Negative Differential Resistance like) is explained by different number of mini-bands contributing to the conductivity as the Fermi levels shifts up in energy. The quantum dot size and inter-dot distance dependences of electrical conductivity are also investigated which are shown in Fig. 3.11 (a), (b) for dot size 6 nm, and 7 nm respectively. Generally, with the same quantum dot size, the smaller dot spacing, the bigger electrical conductivity. Because the smaller dot spacing gives broader bandwidth of miniband, and that increases the electron mobility and conductivity in QDS since mobility is proportional to the bandwidth in Feynman model. Quantum dot size and inter-dot distance can be optimized to get the maximum electrical conductivity of the InAs/GaAs QDS solar cells.

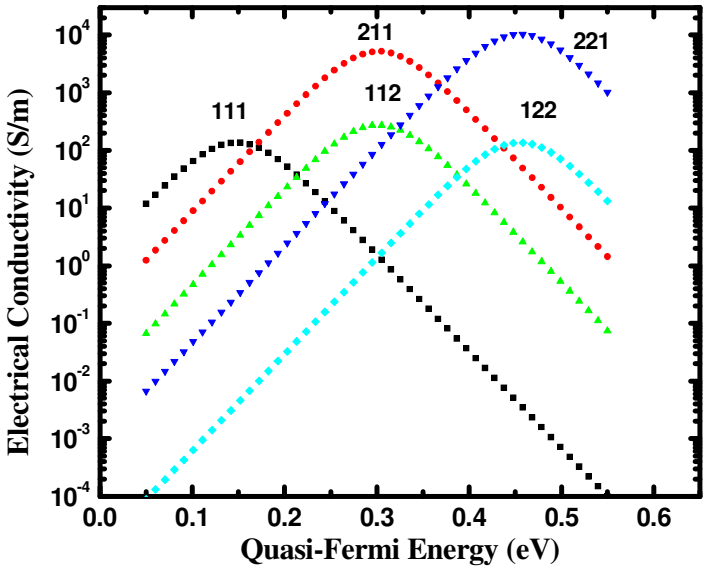

Fig. 3.9 Contribution of individual miniband to the electrical conductivity of InAs/GaAs QDS, Dot size is 10nm and dot spacing is 5nm.

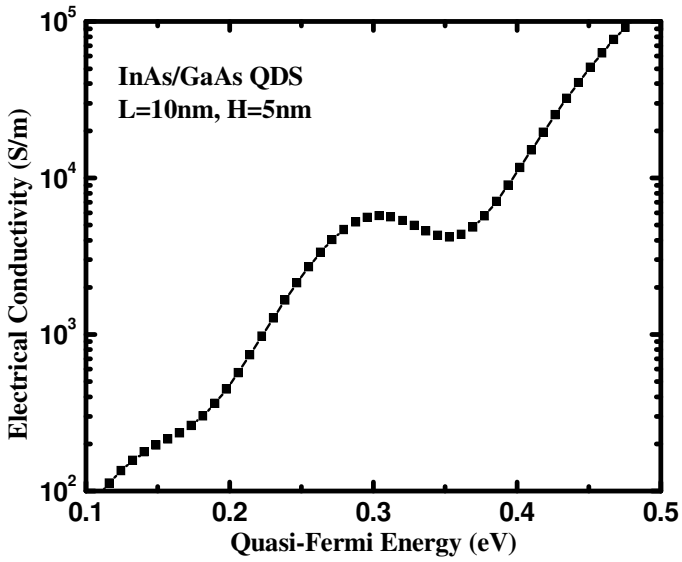

Fig. 3.10 Electrical conductivity of cubical InAs/GaAs QDS as a function of the quasi-Fermi energy at room temperature

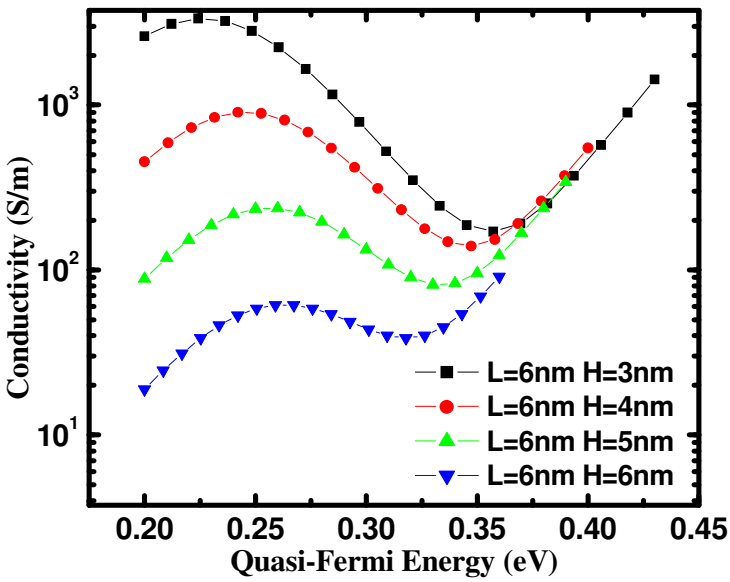

(a)

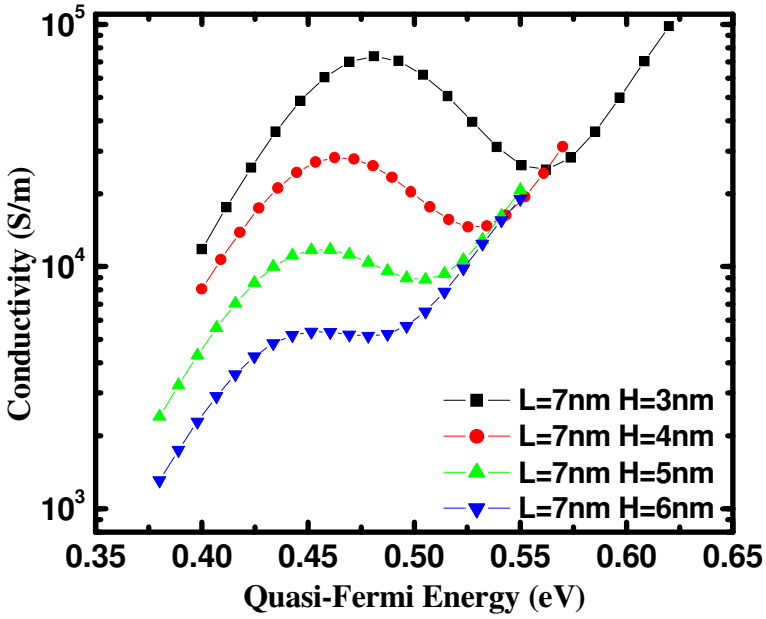

(b)

Fig. 3.11 Quantum dot size and inter-dot distance dependence of electrical conductivity of InAs/GaAs QDS at room temperature

One can modulate the composition of quantum dot or host material to tune the potential well and energy levels of minibands as well. As shown in Eq. 3.3, the electrical conductivity is dependent on both $E_q^{(n)}$ and E_F. The corresponding physical parameters for $E_q^{(n)}$ and E_F are energy levels of minibands and doping concentration in host material respectively. Fig. 3.12 examines the composition and doping concentration dependency of electrical conductivity of QDS. One can tell that conductivity curves are nonlinear for the QDS with given composition and conductivity curve shifts to right as composition of

GaAs in GaInAs increases. The smaller interval of adjacent peaks of conductivity results from the compact piled minibands in the lower potential well.

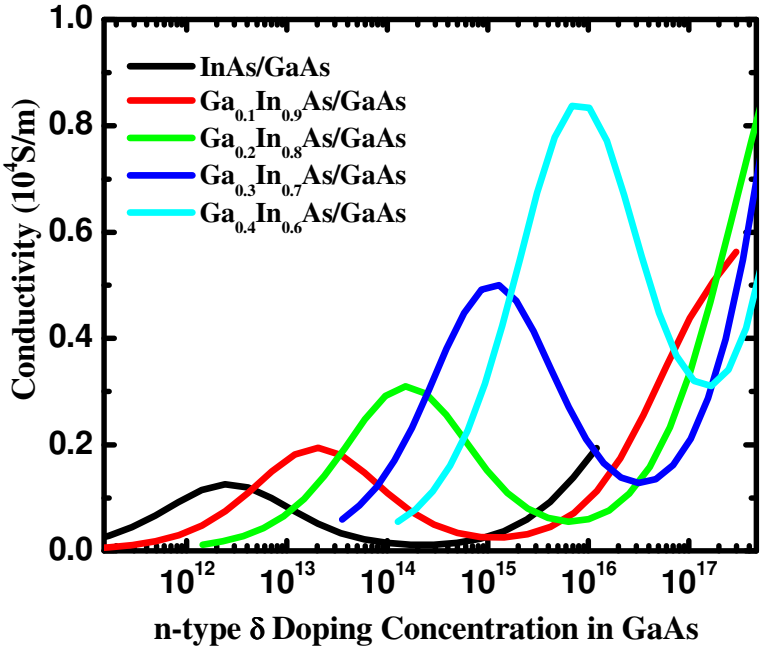

Fig. 3.12 Doping concentration dependency of electrical conductivity for InAs/GaAs QDS with dot size 10 nm, and dot spacing 5 nm

3.2 Optimization of photon absorption and efficiency in IBSC

The energy conversion efficiency is a key parameter in the photovoltaic (PV) solar cell technology. It is defined as

$$\eta = \frac{FF \cdot V_{oc} \cdot J_{sc}}{P_{in}}, \tag{3.5}$$

where FF is the fill factor, V_{oc} is the open circuit voltage, J_{sc} is the short circuit current density, and P_{in} is the incident power per unit area. The performance of the conventional bulk semiconductor cells is limited to about 33% [7]. The theoretical

thermodynamic limit on the conversion of sunlight to electricity is much higher, about 93% [8]. Thus, there is a very strong motivation for finding new approaches, which would allow one to increase the solar cell efficiency.

Luque and Marti [9] have theoretically shown that introduction of the intermediate energy level between the valence band (VB) and conduction band (CB) of a regular semiconductor can increase the efficiency up to ~63%. Practically, IB can be created through the introduction of an impurity band in regular bulk semiconductors, e.g. similar to the earlier proposal by Wolf [10], or formation of a miniband in a superlattice-type structure [11].The extra empty minibands formed inside the potential well will act much like recombination centers rather than generation centers shown in Fig. 3.13(a). The efficiency will be decreased in this case. To avoid this problem, QDS with negligible valence band offset is required like the one shown in Fig. 3.13(b). The first miniband 111 which is half occupied by electrons through appropriate delta doping acts as the IB and second or higher index minibands act like CB. In this case, no extra empty bands exist in potential well, and the efficiency enhancement can be obtained.

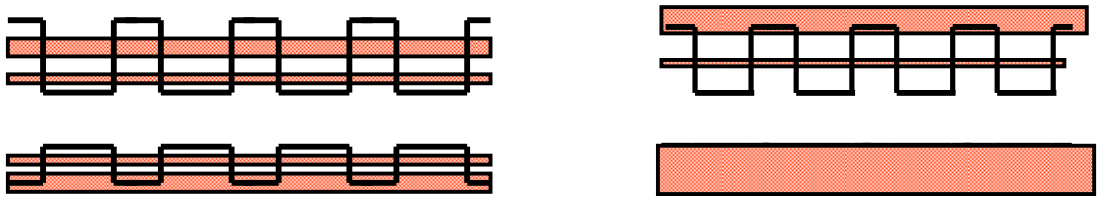

(a) (b)

Fig. 3.13 Band diagram of conventional quantum well superlattices (a) and quantum dot superlattices with negligible valence band offset (b).

We consider 3D-ordered QDS with the closely spaced quantum dots and high quality interfaces, which allow for the strong wave function overlap and formation of minibands

[12]. In such structures, the quantum dots play a role similar to that of atoms in real crystals. To distinguish such nanostructures from the disordered multiple arrays of quantum dots we refer to them as quantum dot supra-crystals. Here we do not address the technological issues of fabricating such supra-crystals but rather examined the possibilities they offer in PV cell design if implemented. At the same time, there have been already a number of reports of 3D-ordered QDS [13-16] as well as in-plane 2D-ordered [17-18] and vertically 1D-ordered [19] QDS. One should expect that further progress in epitaxial growth and self-assembly will deliver more ordered QDS with closely spaced quantum dots. Previous studies confirm the formation of minibands in QDS [20] similar to those in quantum well superlattices (QWS).

A schematic of the considered energy band diagram of IBSC with the periodically arranged quantum dots is shown in Fig. 3.14. The photons which have lower energy than the band-gap of host material will be absorption by two-step process. First, the electron will be excited from VB to IB by absorbing one photon, then excited from IB to CB by absorbing another photon. By this way, the photo-generated current will be increased without degrading the open circuit voltage. E_{FC}, E_{FI} and E_{FV} are the quasi-Fermi levels for CB, IB and VB respectively. IB has to be half-filled with electrons which could be achieved by modulation doping at the barrier region [21]. By engineering the QDS parameters such as quantum dot size, shape, inter-dot separation, dot arrangement, one can optimize IB position and width to achieve the maximum efficiency. The first step for demonstrating a possibility of forming optimum IB is to calculate the electron dispersion in such structure by solving the Schrodinger equation. It has been accomplished following Lazarenkova and Balandin [12] semi-analytical approach, which is addressed

in the part of theoretical formulation. The accuracy of this semi-analytical solution has been later verified by the finite-element simulations [20, 22].

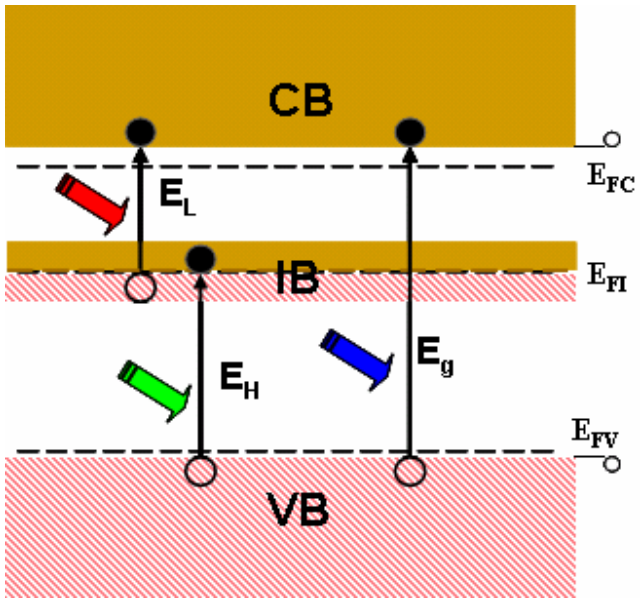

Fig. 3.14 Band diagram of a intermediate band solar cell

For an ideal solar cell, the photon-generated current is proportional to the difference between the number of photons absorbed by the device and the number of photons emitted from the device. In the IB solar cell, the short-circuit current density J_{SC} can be written as [9]

$$J_{SC}/q = [\dot{N}(E_{13},\infty,T_s,0) - \dot{N}(E_{13},\infty,T_a,\mu_{CV})] + [\dot{N}(E_{23},E_{12},T_s,0) - \dot{N}(E_{23},E_{12},T_a,\mu_{CI})] \quad (3.6)$$

where T_s is the temperature of the Sun (6000 K), T_a is the temperature of the solar cell (300 K), $\dot{N}$ is the flux of photons absorbed by or emitted from the semiconductor, and E_{13} E_{23} E_{12} are energy spacing among three energy levels. In thermodynamic equilibrium, $\dot{N}$ is given by [23]

$$\dot{N}(E_l, E_h, T, \mu) = \frac{2\pi}{h^3 c^2} \int_{E_l}^{E_h} \frac{E^2 dE}{e^{(E-\mu)/k_B T} - 1} \tag{3.7}$$

where E_l and E_h are the lower and upper energy limit of the photon flux for the corresponding transitions, respectively, μ is the chemical potential of the transition, k_B is Boltzmann constant, E is the photon energy, h is Planck constant, and c is speed of light. The output voltage can be described as the difference of the chemical potentials between CB and VB, i.e. $qV_{OC} = \mu_{CV} = \mu_{CI} + \mu_{IV}$. By this detailed balance principle, we plotted the conversion efficiency limit for different structured solar cells shown in Fig. 3.15. IBSC has the highest efficiency of 63.1% with the optimum E_I of 0.71 eV and E_G of 1.95 eV instead of 40.7% which is the Shockley-Queisser limit for single gap cells [24].

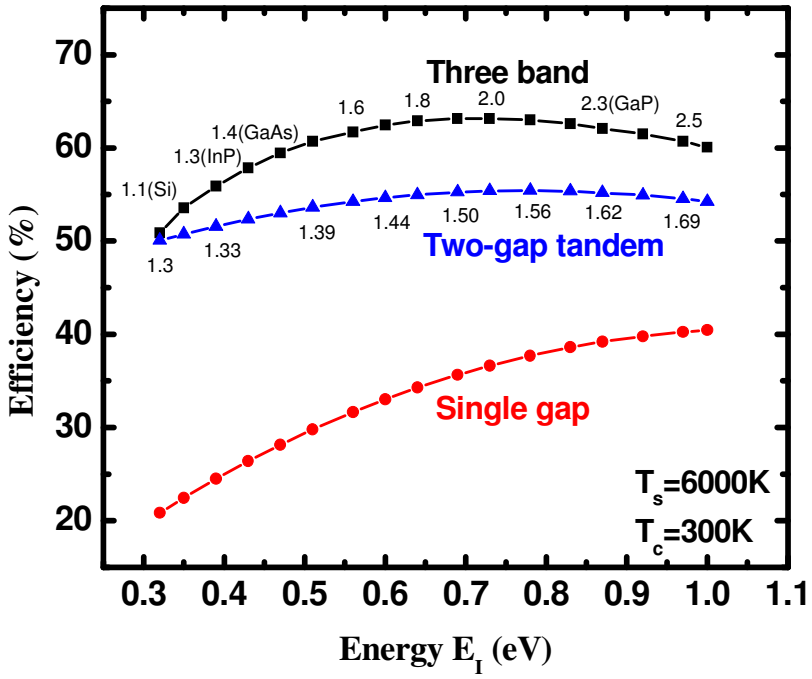

Fig. 3.15 Efficiency limit for a three-band solar cell and for a two gap tandem cell, in both cases vs the lowest band gap E_I, and for a single gap cell. The corresponding values

of the highest band gap (E_G) in cells with intermediate band and in tandem cells, for maximum efficiency, are also presented.

The above calculation does not consider the effect of IB bandwidth on efficiency. The IB bandwidth is a natural consequence when spacing of quantum dot array is small enough to be comparable to electron wavelength. We investigated bandwidth effect analysis on the QDS sample made of $InAs_{0.9}N_{0.1}/GaAs_{0.98}Sb_{0.02}$ material system. The valence band offsets are negligible in this system and the conduction band offset is equal to $E_{barrier}\approx 1.29eV$ [25]. The values for the electron effective masses, $m^*_{InAsN} = 0.0354m_0$ and $m^*_{GaAsSb} = 0.066m_0$ (m_0 is the electron rest mass) and other band parameters have been taken from Ref. [26]. The band gap of $GaAs_{0.98}Sb_{0.02}$ is 1.48eV. From Fig. 3.15 one can read that the maximum efficiency is around 60.4% with the optimum E_I of 0.51eV and zero bandwidth for IBSC. Fig. 3.16 shows the bandwidth of IB effect on efficiency for the given material system. We made one assumption in our calculation of efficiency with finite bandwidth. The photon energy which is bigger than the transition energy E_{12} and smaller than the transition energy E_{13} will have to participate in E_{12} transition (see Fig. 3.17). The tendency is found that if $E_I + BW < E_I(optimum)$, the efficiency will increase as the bandwidth increases; if $E_I + BW > E_I(optimum)$, the efficiency will decrease as the bandwidth increases.

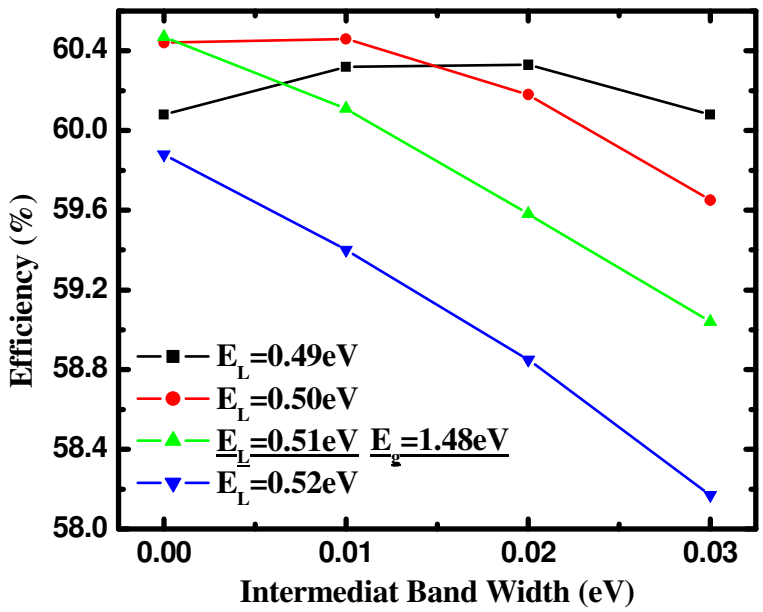

Fig. 3.16 Bandwidth effect on conversion efficiency for $InAs_{0.9}N_{0.1}/GaAs_{0.98}Sb_{0.02}$ based IBSC. The dot size of 4.5 nm and dot spacing is 2 nm.

Fig. 3.17 shows the calculated electron energy dispersion *E(q)* in the simple cubic (SC) QDS with the quantum dot size L = 4.5 nm and the inter-dot distance H = 2 nm. The minibands are labeled by the quantum numbers $n_x\, n_y\, n_z$, which define the total energy of an electron as the sum of its component along three axes [12]. The dispersion is shown for the electron wave vector *q* along [[100]] quasi-crystallographic direction in the coordinate system formed by the quantum dots in the supra-crystal (we retained the notations proposed by Lazarenkova and Balandin [12, 20]). The [[100]] direction is the most important one since it defines the charge carrier transport in the vertical direction to *n* and *p* type layers.

One can see from Fig. 3.18 that the band-widths of the minibands are 0.03 eV for the band 111 and 0.2 eV for the overlapping minibands 211 and 112. The higher-index

minibands whose energies are higher than $E_{barrier}$ are mutually overlapping or very close to each other. For these reasons we consider the higher-energy minibands as a quasi-continuum CB. In Fig. 3.18 we depict the real-space band diagram for our proto-type structure with the calculated energies and miniband widths. Here, the miniband 111 acts as IB while the overlapping minibands 211 and 112 act as the band analogous to CB from where the generated electrons are extracted as a current flow. The VB in our structure is the same as in bulk semiconductors owing to the small valence band offset.

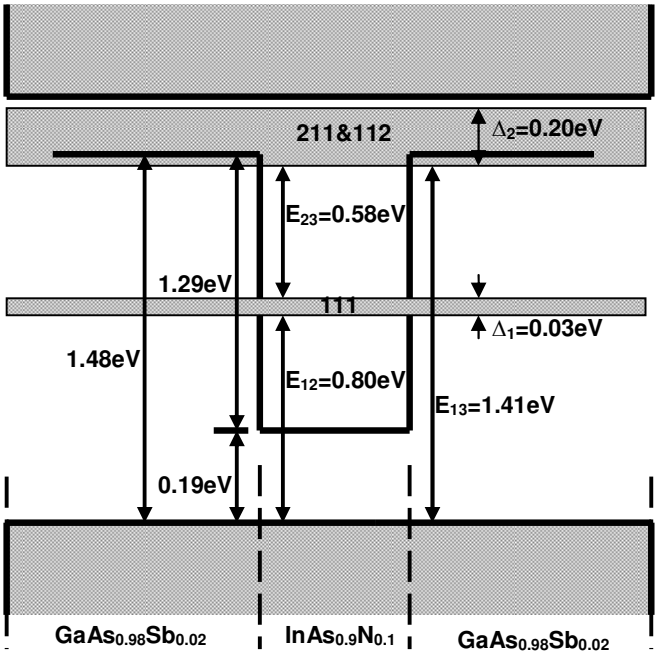

Fig. 3.17 Electron dispersion in $InAs_{0.9}N_{0.1}/GaAs_{0.98}Sb_{0.02}$ quantum dot supra-crystal along [[100]] quasi-crystallographic direction. Results are shown for the simple cubic QDS with the quantum dot size L = 4.5 nm and inter-dot spacing H = 2 nm along all directions. The energy in units of eV is counted from the bottom of the potential well.

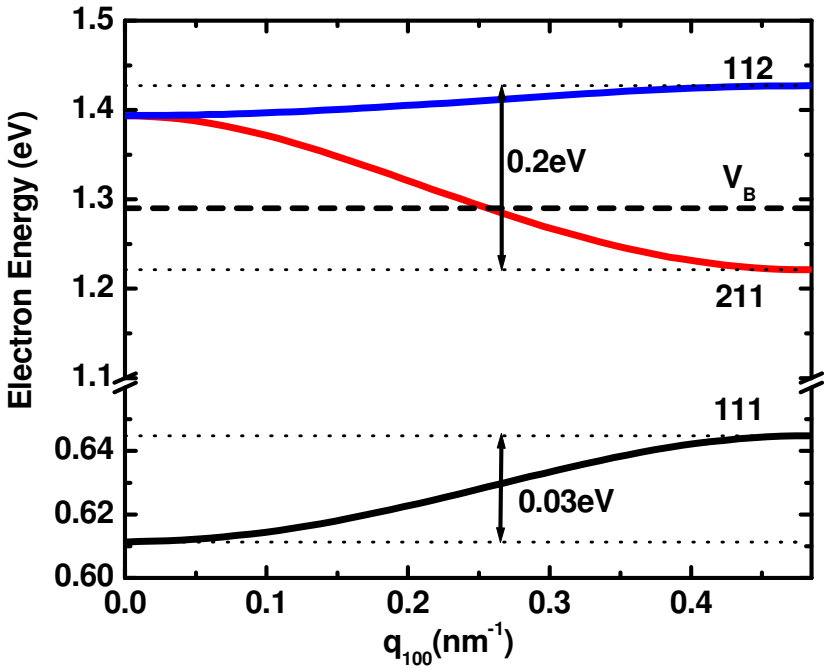

Fig. 3.18 Energy diagram showing minibands formed in the same structure

The values of L and H, which led to the dispersion and band diagram, are not arbitrary. They were chosen after simulating the electron energy dispersion as those, which give the transition energies E_{13}=1.41 eV, E_{23}=0.58 eV, E_{12}=0.80 eV, and the IB (miniband 111) width Δ_1=0.03 eV. These energy separations between CB and IB and between IB and VB are very close to those determined by Levy *et al* [25] for the same material system. Assuming as given the optimum energy band parameters (E_{13}=1.48 eV, E_{23}=0.51 eV, E_{12}=0.97 eV, and Δ_1=0), Levy *et al* [25] calculated the maximum IB solar cell efficiency of ~60.5%. Thus, we have demonstrates that SC arrangement of quantum dots in the supra-crystal is versatile enough to provide the miniband, which act as IB and lead to the efficiency enhancement.

The theoretical limit for the PV efficiency of IB solar cell determined in Ref. [25] has been calculated for the idealized band structure with the zero IB width (Δ_1=0) and optimum E_{23} of 0.51 eV. In our case, all band parameters are defined by the actual electron dispersion in QDS and cannot be tuned independently. For these reason E_{23} and E_{12} slightly deviate from the optimum values. In order to determine the actual PV efficiency of our supra-crystal with IB we follow the detailed balance theory of Shockley and Queisser [24]. The calculations are performed under the standard assumptions of the ideal solar cell specified by Luque and Marti, i.e., nonradiative transitions are forbidden, the quasi-Fermi levels are constant throughout the whole cell volume, PV cell is thick enough to assure full absorption of the photons with enough energy to induce any of the transitions depicted in Fig. 3.17, and Ohmic contacts are applied in such a way that only electrons (holes) can be extracted from the conduction (valence) band to form the external current.

The properties of IB itself deserve a special consideration. The electron density of states (DOS) in IB has to be as high as possible in order to pin the IB quasi-Fermi level at its equilibrium position. DOS for IB (111 miniband) in the SC supra-crystal is presented in Fig. 3.19. As one can see DOS in QDS is very different from that in conventional QWS or bulk crystals. The area under the DOS curve is 7.395×10^{18} cm^{-3}, which is of the same order of magnitude as DOS in VB and CB and provides sufficient IB quasi-Fermi level pinning.

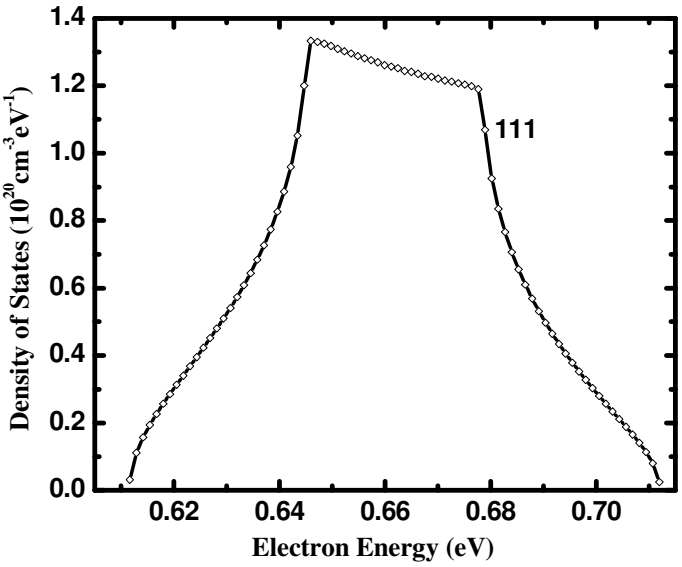

Fig. 3.19 DOS in the miniband 111 serving as a IB in the supra-crystal solar cell

For the intermediate band solar cell application, it is important to know the effective mass of electrons. While in single quantum dots the effective mass will be mostly defined by the material of the dot, crystallographic direction and the strain distribution, in QDS it will strongly depend on the periodicity and regimentation of the dots in the artificial crystal. A reciprocal effective mass tensor in QDS is defined as

$$(\frac{m_0}{M^*})_{\alpha\beta} = \frac{m_0}{\hbar^2}\frac{\partial^2 E}{\partial q_\alpha \partial q_\beta} \tag{3.8}$$

The average scattering time is 50fs in typical III-V compounds. Therefore we can obtain the band edge mobility of ~ 731 cm^2/Vs in IB. There exists a tradeoff between bandwidth and efficiency. A large bandwidth is necessary to improve the mobility. The typical value of mobility in IB to avoid resistive losses under 1 sun illumination is around 100 cm^2/Vs. However, the large bandwidth will cause the carrier relaxation in IB to loss energy.

The effective mass in band 111 and 211, 112 along [[100]], [[110]], and [[111]] are shown in Fig. 3.20. In [[100]] direction, the electron effective mass in IB at band edge is $0.12m_0$. The average scattering time is 50fs in typical III-V compounds. Therefore we can get the band edge mobility in IB is ~ 731 cm^2/Vs. There exists a trade off between bandwidth and efficiency. A big bandwidth is necessary to improve the mobility. The typical value of mobility in IB to avoid resistive losses under 1 sun illumination is around 100 cm^2/Vs. However, the wide bandwidth will cause the carrier relaxation in IB to loss energy.

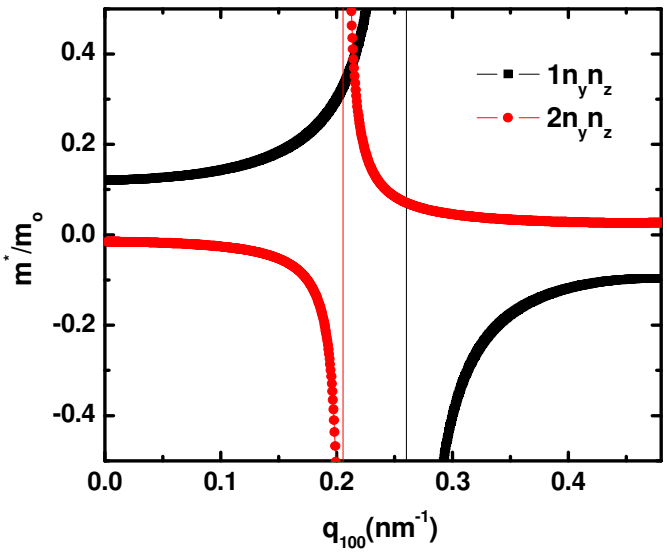

(a)

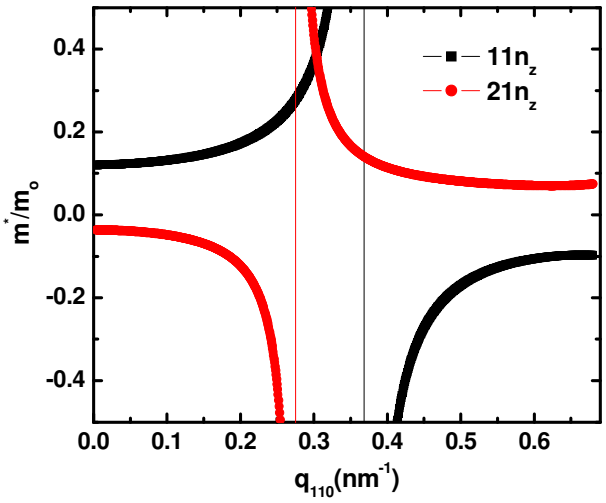

(b)

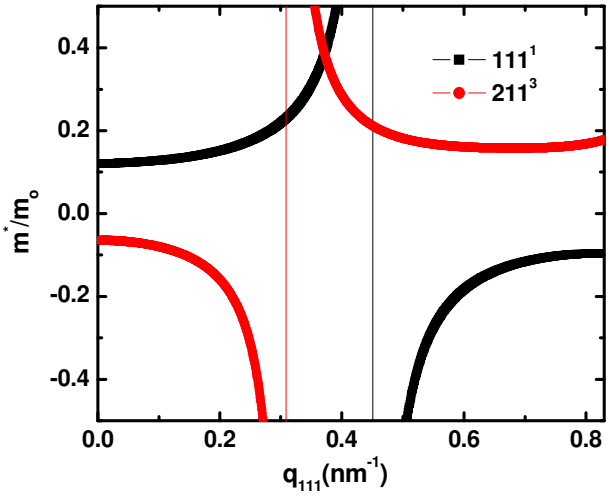

(c)

Fig. 3.20 (a) (b) (c) Electron effective mass in cubical QDS along [[100]], [[110]], and [[111]] quasi-crystallographic directions. The dot size is 4.5nm and dot spacing is 2nm.

Assuming that in Eq. (3.5) the fill factor is unity and the incident power is $P_{in} = \sigma T_s^4$ (here σ is the Stefan-Boltzmann constant) one can calculate the efficiency upper limit for the optimum QDS parameters. Fig. 3.21 shows the PV power conversion efficiency of the IB solar cell based on quantum dot supra-crystal as a function of the dot size. The maximum efficiency obtained for QDS with L = 4.5 nm and H = 2 nm, which has the band structure parameters close to the "ideal" ones, is 51.2%. It is smaller than the value obtained in Ref. [25] but still significantly larger than the Shockley and Queisser limit of ~ 30% for bulk semiconductors [24].

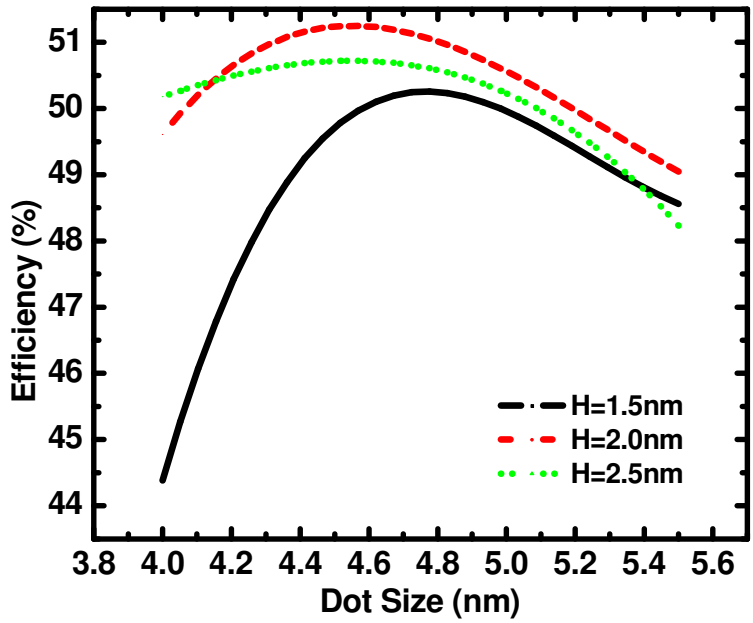

Fig. 3.21 Photovoltaic power conversion efficiency as a function of the quantum dot size in $InAs_{0.9}N_{0.1}/GaAs_{0.98}Sb_{0.02}$ quantum dot supra-crystal. The results are shown for several inter-dot separations. The structure parameters are the same as in Figs. 3.17 and 3.18.

Since the miniband is continuous in the whole reciprocal lattice space. During the process of photon absorption, electrons can probably move from [[100]] regime to other regimes, e.g. [[110]] or [[111]] quickly. In result, the energy of the following optical transition could be different from the one along [[100]] direction. The energy spacing and efficiency are changed consequently. The energy dispersions along other quasi-crystallographic directions besides [[100]] direction have to be investigated. Fig. 3.22 shows the electron energy dispersion relations along ΓX [[100]], ΓR [[111]], ΓM [[110]] and XM directions. The bandwidths and energy levels for optical transitions along these directions are shown in Table 3.1 and Table 3.2. The efficiencies for electron transport in these directions are also listed in Table 3.2. In conclusion, considering the effect of carrier transporting along unpredictable directions, the efficiency of IBSC is in the range of 49% ~ 53%. Our efficiency value along [[100]] is ~ 51%. Therefore, variable electron dispersions have no big influence on the efficiency which we calculated for the $InAs_{0.9}N_{0.1}/GaAs_{0.98}Sb_{0.02}$ quantum dot supra-crystal IBSC.

Table 3.1 Miniband data from energy dispersion relation spectrum

Direction	Miniband 111		Combined Band 211&112	
	Energy Range (eV)	Bandwidth Δ_1 (eV)	Energy Range (eV)	Bandwidth Δ_2 (eV)
ΓX (100)	0.613-0.645	0.032	1.22-1.42	0.20
ΓM (110)	0.613-0.678	0.065	1.25-1.46	0.21
ΓR(111)	0.613-0.712	0.099	1.29-1.39	0.10
XM	0.645-0.678	0.033	1.22-1.46	0.24

Table 3.2 Efficiency according to the particular direction

Direction	E_{12} (eV)	E_{23}(eV)	E_{13}(eV)	Δ_1(eV)	Eff. (η)
ΓX (100)	0.803	0.576	1.411	0.032	**51.24%**
ΓM (110)	0.803	0.572	1.44	0.065	**49.43%**
ΓR(111)	0.803	0.578	1.48	0.099	**53.26%**
XM	0.835	0.542	1.41	0.033	**53.02%**

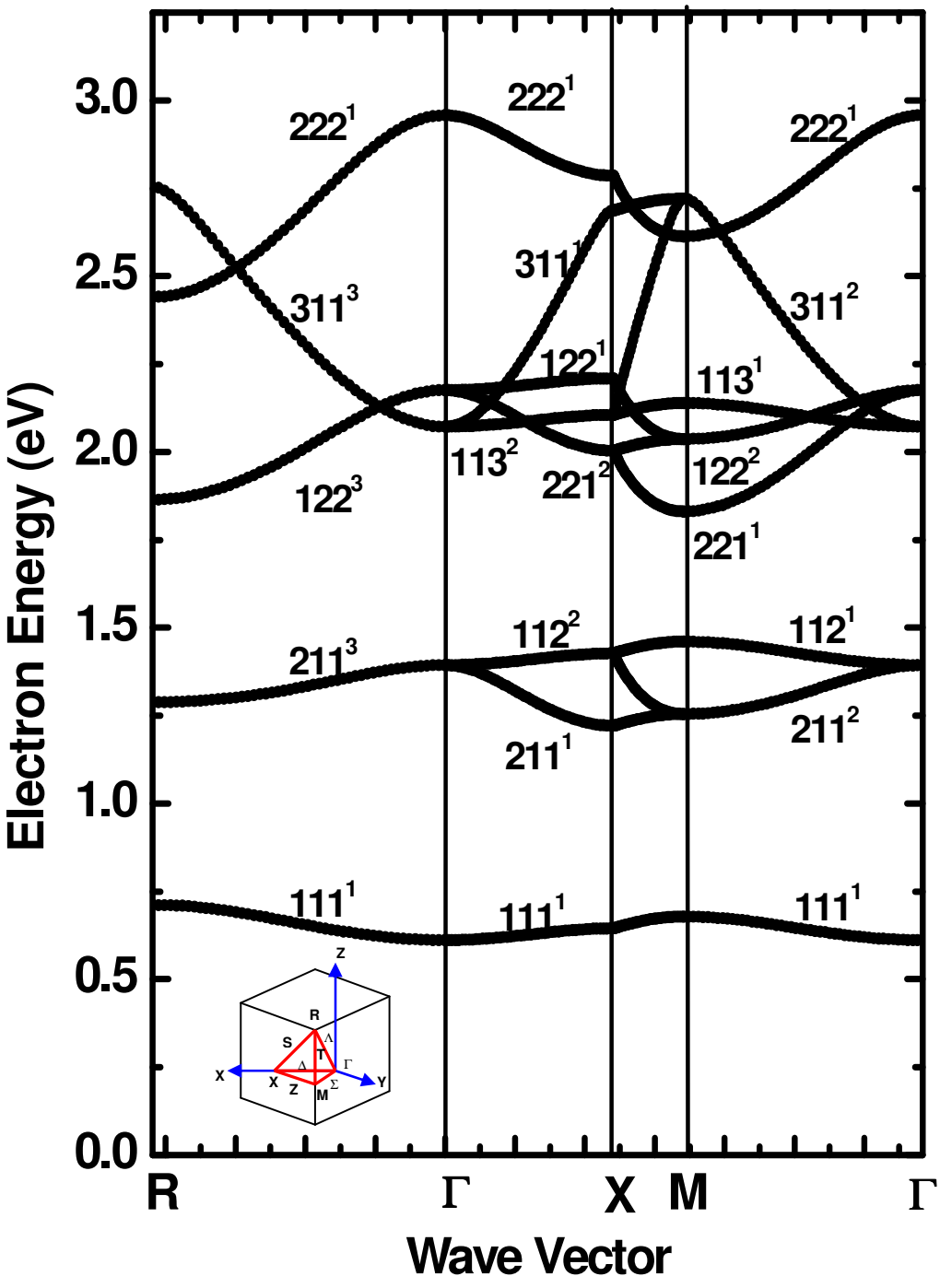

Fig. 3.22 Complete electron energy dispersion relation of InAsN/GaAsSb along directions of Γ*X* [[100]], Γ*R* [[111]], Γ*M* [[110]] and *XM*. The dot size is 4.5nm, and dot spacing is 2nm. Inset is the reciprocal lattice presenting specified wave vector directions.

The cubic quantum dots and equal dot spacing in 3D are assumed in the simulations shown above. We refined the model to allow us to accurately treat dot and spacing dimensions and provide meaningful feedback to the materials growers.

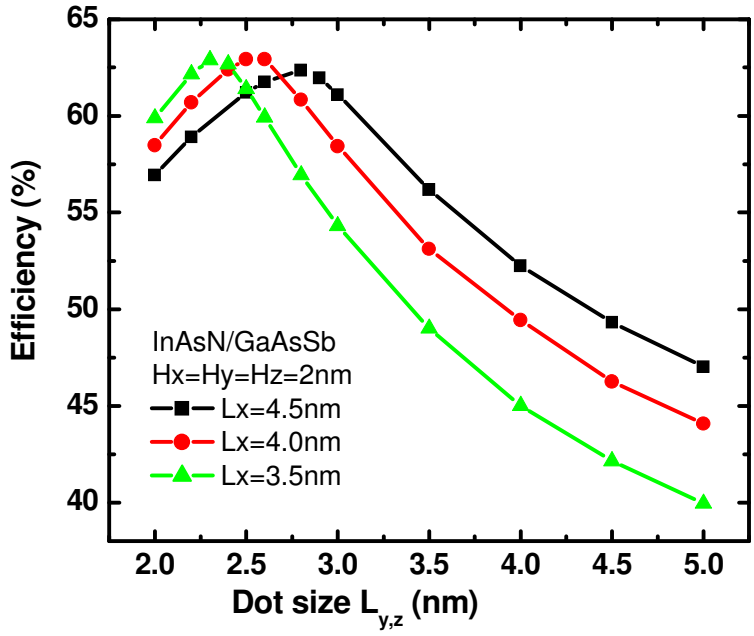

Fig. 3.23 Dot size dependent power efficiency in IBSC

Fig. 3.23 shows the power conversion efficiency along [[100]] quasi-crystallographic direction for tetragonal quantum dots based IBSC. The inter-dot distance are constants of *Hx = Hy = Hz = 2 nm*. In this case, the theoretical efficiency above 60% can always be reached with optimum size of quantum dot size. The modulation of dot size in y, z direction can change energy level position in y, z direction. Since the total energy is the sum of energy along three axes, the energy separation will also be modulated according

to the change of dot size. Therefore the conversion efficiency can be optimized by size modulation of tetragonal quantum dots.

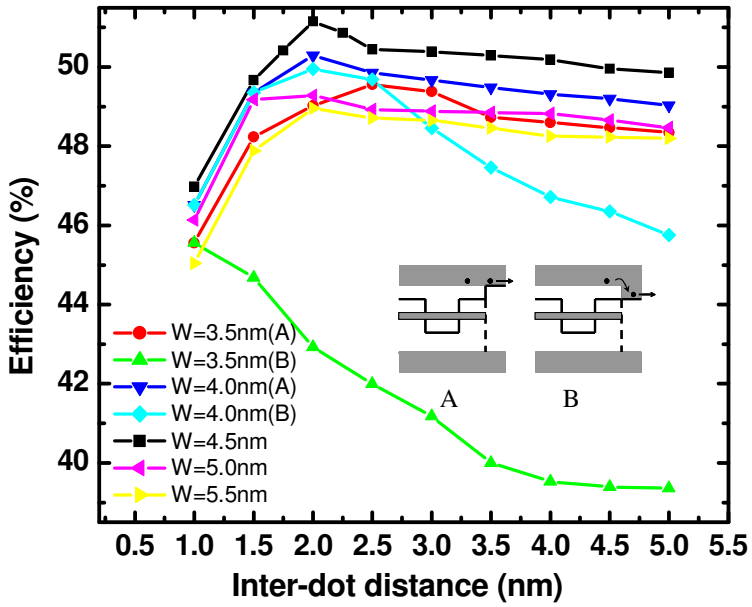

Fig. 3.24 Interdot distance dependent power efficiency in IBSC

Fig. 3.24 shows the effect of dot spacing modulation on power efficiency for different dot sizes. This figure shows two conditions:

A: the structure with band alignment layer (higher bandgap than that of host matrix)

B: structure without band alignment layer (the same material as the host matrix)

The purpose of the introduction of band alignment layer is to make photon-excited carriers to be extracted freely without quick relaxation to band edge by making its conduction band align to the second miniband in QDS region and making its valence band align to that of QDS. When the dot size is smaller than 4nm, the small quantum dots squeeze the second miniband out of the potential well. A band alignment layer is needed

to improve the efficiency by avoiding the quick thermal relaxation. Fig. 3.24 also shows efficiency difference of 3.5 nm and 4.0 nm interdot spacing with and without a band alignment layer. For 4.0 nm dot size, the efficiency is same with dot spacing smaller than 1.5 nm, since small dot spacing increases the bandwidth of the miniband to cover the barrier. When it is bigger than 1.5 nm, the second miniband is over the barrier height, and a band alignment layer is needed. With the band alignment layer, the efficiency has no big change (> 45%) as the dot spacing increases.

Solar concentrators use lenses or mirrors to concentrate sunlight onto solar cells. Concentrator systems increase the power output while reducing the size or number of cells needed. An additional advantage is that a solar cell's efficiency increases under concentrated light. Relatively inexpensive materials such as plastic lenses can be used to make concentrator to capture the solar energy shining on a fairly large area and focus that energy onto a smaller area, where the solar cell is. One measure of the effectiveness of this approach is the concentration ratio. There are several definitions of solar concentration ratio. The commonly accepted one is intensity concentration, or "suns". Since standard solar irradiance is set at 1 kW/m^2, the suns concentration is defined as the ratio of the average intensity of the focused light on the cell active area divided by 1 kW/m^2.

Detailed balance principle is based on the variation of number of photons in a mode with difference of the absorption and emission rates of photons. The variation of number of photons can be calculated as [27-28]

$$d\upsilon = -[\alpha_{CV}(\upsilon - \upsilon_{CV}) + \alpha_{IC}(\upsilon - \upsilon_{IC}) + \alpha_{VI}(\upsilon - \upsilon_{VI})]d\varsigma \qquad (3.8)$$

where α_{CV}, α_{CI} and α_{IV} are the absorption coefficients due to transitions VB to CB, IB to CB and VB to IB respectively, and υ_{CV}, υ_{CI} and υ_{IV} are the Bose-Einstein factors for the luminescent radiation caused by the transitions CB to VB, CB to IB and IB to VB respectively. These factors are related with the amount of quasi-Fermi level splitting, and can be expressed as

$$\upsilon_{XY} = \frac{1}{\exp(\frac{\varepsilon - \mu_{XY}}{kT}) - 1} \tag{3.9}$$

where X and Y are representing C, I or V. Finally, $d\varsigma$ is the element of length along the photon path. In this equation, the first expression in the parentheses refers to the absorption of photons and the second expression in the parentheses refers to the emission of photons. The inequality of absorption rate and emission rate in a semiconductor results in the variation of charge carrier concentration. Disregarding the nonradiative recombination process, the current density produced from the variation is given as folllows

$$-\nabla J_e / e = \frac{2}{h^3 c^2} \int_{\varepsilon,\Omega} [\alpha_{CV}(\upsilon - \upsilon_{CV}) + \alpha_{IC}(\upsilon - \upsilon_{IC})] \varepsilon^2 d\varepsilon d\Omega \tag{3.10}$$

where J_e is electron current density, e is electron charge, h is Planck constant, c is the speed of light, ε is energy and $d\Omega$ is the solid angle. Using continuity equations, the current density equation is obtained under assumption of constant μ_{CV}, μ_{CI} and μ_{IV} values.

$$J_e = J_{gen,e} - J_{rad,e} - J_{\text{int},e} + J_p(0) + J_n(w) \tag{3.11, a}$$

$$J_h = J_{gen,h} - J_{rad,h} - J_{\text{int},h} + J_p(0) + J_n(w) \tag{3.11, b}$$

J_e and J_h are the current densities of electrons and holes at the emitter interfaces, respectively. $J_p(0)$ and $J_p(W)$ are the minority current densities of the emitters that are

ignored in this study. $J_{gen,e}$ and $J_{gen,h}$ correspond to the generated current densities of electrons and holes due to photon absorption respectively. $J_{rad,e}$ and $J_{rad,h}$ correspond to the radiative recombination current densities of electrons and holes respectively. $J_{int,e}$ and $J_{int,h}$ are electron/hole current densities of internal recombination that are the results of the reabsorption of some generated photons in a band other than the one in which they were generated. All these current densities are given as follows:

$$J_{gen,e} = e\int_{\varepsilon} M_e F_{abs} d\varepsilon \, , J_{gen,h} = e\int_{\varepsilon} M_h F_{abs} d\varepsilon \tag{3.12}$$

$$J_{rad,e} = e\int_{e} M_e F_{emi} d\varepsilon \, , J_{rad,h} = e\int_{e} M_h F_{emi} d\varepsilon \tag{3.13}$$

$$J_{\text{int},e} = \frac{8\pi ew}{h^3 c^2}\int (\frac{\alpha_{CV}\alpha_{VI}}{\alpha_{tot}}(\upsilon_{CV} - \upsilon_{VI}) + \frac{\alpha_{IC}\alpha_{VI}}{\alpha_{tot}}(\upsilon_{IC} - \upsilon_{VI}))d\varepsilon \tag{3.14, a}$$

$$J_{\text{int},h} = \frac{8\pi ew}{h^3 c^2}\int (\frac{\alpha_{CV}\alpha_{VI}}{\alpha_{tot}}(\upsilon_{CV} - \upsilon_{VI}) + \frac{\alpha_{IC}\alpha_{VI}}{\alpha_{tot}}(\upsilon_{IC} - \upsilon_{VI}))d\varepsilon \tag{3.14, b}$$

M_e and M_h are defined as

$$M_e = \frac{\alpha_{CV} + \alpha_{IC}}{\alpha_{tot}} \, , M_h = \frac{\alpha_{CV} + \alpha_{VI}}{\alpha_{tot}} \tag{3.15}$$

$$\alpha_{tot} = \alpha_{CV} + \alpha_{IC} + \alpha_{VI} \tag{3.16}$$

F_{abs} and F_{emi} correspond to the spectral photon flux absorbed or emitted by the cell.

$$F_{abs} = X\frac{2\pi}{h^3 c^2}(1 - \sin^2\theta_S)(1 - \exp(-2w\alpha_{tot}))\upsilon(0) \tag{3.17}$$

$$F_{emi} = \frac{2\pi}{h^3 c^2}(1 - \exp(-2w\alpha_{tot}))(\frac{\alpha_{CV}\upsilon_{CV} + \alpha_{IC}\upsilon_{IC} + \alpha_{VI}\upsilon_{VI}}{\alpha_{tot}}) \tag{3.18}$$

where X is the sun concentration ratio and $\theta_S \approx 0.267^O$ is the semi-angle with which the solar disk is seen from the Earth [29]. As seen from equations (3.14, a) and (3.14, b), $J_{int,e}$

and $J_{int,h}$ are zero when there is no absorption overlap among three transitions. In order to obtain power conversion efficiency, J_e and J_h current densities are equalized. The output voltage V is calculated as the quasi-Fermi level splitting of electrons and holes:

$$eV = \mu_{IV} + \mu_{CI} = \mu_{CV} \tag{3.19}$$

The power conversion efficiency is calculated using the voltage and current density at the optimum operating point.

According to the equation (3.20), the V_{oc} increases resulting from the increase of I_{sc} by utilizing the solar concentrator, therefore, the power conversion efficiency of cell is increased.

$$V_{oc} = \frac{kT}{q}\ln(\frac{I_{sc}}{I_o}+1) \tag{3.20}$$

Fig. 3.25 shows the efficiencies of Si, GaAs and IBSC based on InAsN/GaAsSb with different solar concentration ratios. From equation (3.21), the PCE is almost linear depending on the concentration in logarithmic scale. There is no remarkable efficiency enhancement for IBSC as compared to single-junction cell under one sun. More concentrated sunlight, better efficiency improvement. Comparing single junction cell and IB cell, the PCE can increase by 10% under 1000 suns illumination. The cell temperature is maintained at 300K in the simulation. The increased temperature will degrade the solar cell performance.

$$\begin{aligned}\eta &\propto \frac{XI_{sc}V_{oc}}{XP_{in}} = \frac{kT}{qP_{in}} I_{sc}\ln(\frac{XI_{sc}}{I_o}) \\ &= \frac{kT}{qP_{in}} I_{sc}\ln(X) + \frac{kT}{qP_{in}}\ln(\frac{I_{sc}}{I_o})\end{aligned} \tag{3.21}$$

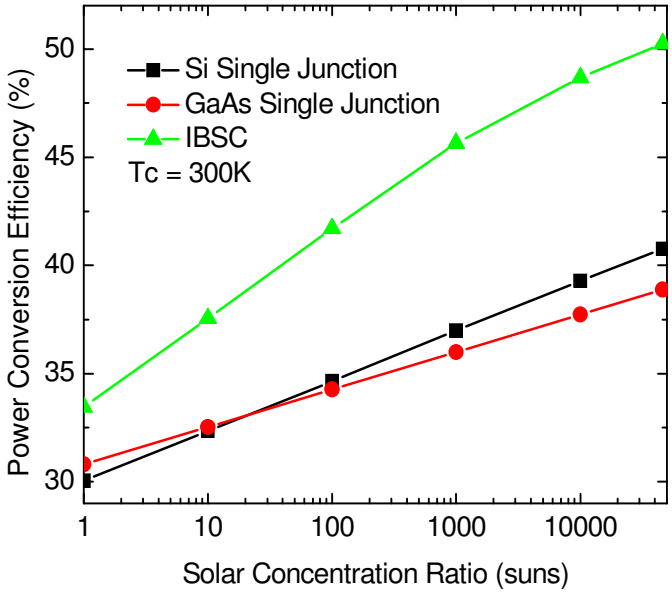

Fig. 3.25 Efficiency comparison of Si, GaAs solar cells and IBSC

The efficiency calculations of IBSC are performed under the assumption that PV cell is thick enough to assure full absorption of the photons with enough energy to induce any of the appropriate transitions. In practice, the cell thickness is usually around several microns according to the state-of-the-art thin film solar cell design and processing because the thick absorber can increase the production cost and also the internal recombination rate of photon-generated carriers. The cell efficiency as a function of the cell thickness is investigated.

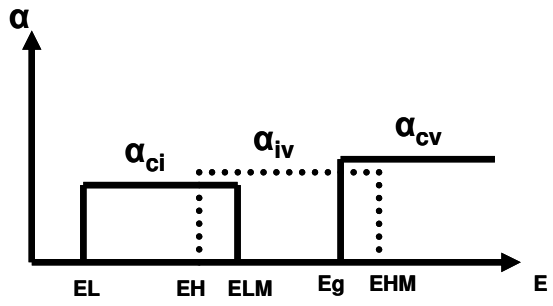

Fig. 3.26 Overlapping absorption coefficients in IBSC

The Fig. 3.26 is showing the absorption coefficient overlap for different transitions. Absorption coefficient a_{ci}, a_{iv}, and a_{cv} are corresponding to the transition from CB to IB, from IB to VB and from CB to IB respectively [30]. All of them are assumed to be equal to 4×10^4 cm^{-1} which is a typical value in GaAs. The overlap is defined by E_{LM}-E_H, and E_{HM}-E_g. Reflective index of 3.5 is used for GaAs. Fig. 3.27 represents the limiting efficiency of an IBSC with optimum energy level separations as a function of absorption energy overlap. The maximum efficiency for a single junction cell is also shown for concentration ratios of 1, 1000 and 46050 suns. The correspondingly optimized cell thickness for maximizing efficiencies has been indicted in micrometers. Note that, the when the overlap increases, the efficiency is reduced significantly from its ideal value of 62.9% (46050 suns) or 57.3% (1000 suns) for zero overlap to ~32.5% for a large overlap of 5 eV. It is found that when the overlap is increased, the optimum cell thickness is reduced and becomes almost a constant for a sufficiently large overlap.

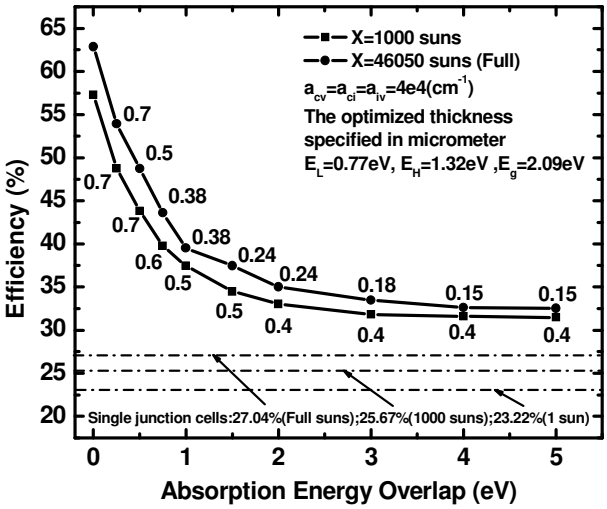

Fig. 3.27 Efficiency of IBSC with optimum energy level separations at 1000 suns and 46050 suns (E_L = 0.77 eV, E_H = 1.32 eV and E_g = 2.09 eV) as a function of absorption energy overlap

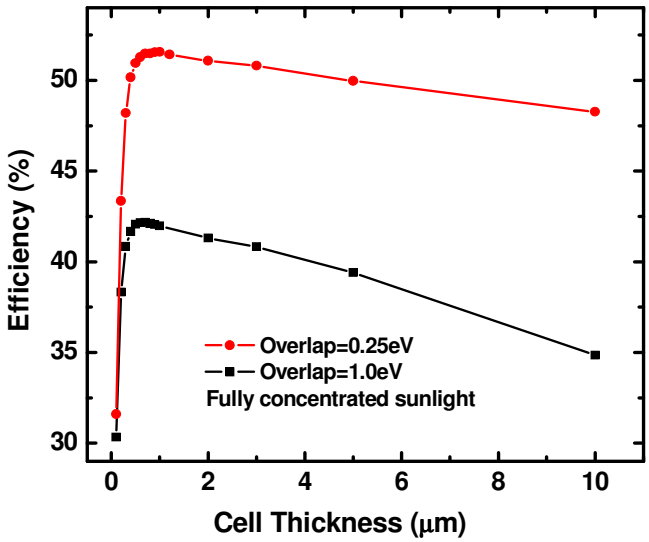

Fig. 3.28 Cell thickness dependent efficiency variation of IBSC based on InAsN/GaAsSb with varied absorption energy overlap

Fig. 3.28 shows the cell thickness dependent efficiency variation of IBSC based on InAsN/GaAsSb with varied absorption energy overlap. Given a certain cell thickness, the cell efficiency is considerably reduced by increasing the value of absorption energy overlap. Fig. 3.29 shows the cell thickness dependent efficiency variation of InAsN/GaAsSb IBSC with different concentration ratio. From this figure, one can notice that higher concentrated illumination gives higher power conversion efficiency. For fully concentrated illumination, it is interesting to see that the efficiency is not sensitive to the cell thickness once it surpasses a specific value of 0.8μm.

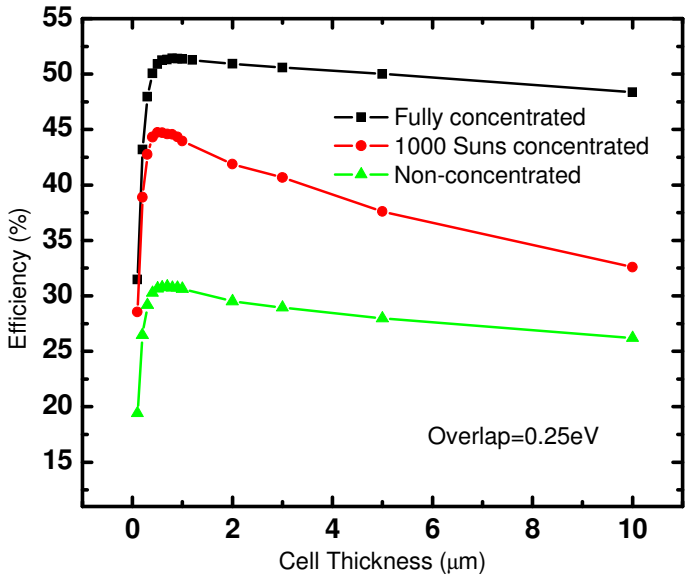

Fig. 3.29 Cell thickness dependent efficiency variation of IBSC based on InAsN/GaAsSb with varied concentration ratios

3.3 Design of intermediate band tandem solar cell

The conventional tandem junction solar cell is a configuration of two or more subcells in series, connected by a tunnel junction. Each subcell is sensitive to a different part of the solar spectrum. The subcell with the largest bandgap is placed on top to absorb the highest-energy photons and allow lower-energy photons to pass through and be absorbed by underlying subcells. The theoretically predicted maximum efficiency, e. g. the "detailed balance" limit, is ~ 55% for the two-junction tandem and ~ 87% for ideal infinite-junction tandem as compared to ~ 41% for the single junction cell under the fully concentrated sunlight [31-32]. The conventional tandem junction cells are used for a variety of practical applications and currently the most efficient solar cells on the market. However, the lattice match between subcells and degenerated doping in tunnel junctions as low resistance interconnects are remaining the technical challenge.

We report a novel type of the solar cell, which combined the benefits of the intermediate band concept and the tandem cell design. It is implemented on the basis of QDS and original layered structure envisioned by us. The novel device is referred as the intermediate-band tandem solar cell (IBTSC). It can substantially improve the solar cell power conversion efficiency and it is expected to perform better than the conventional intermediate band solar cell (IBSC) or two-gap tandem cell.

To implement IBTSC, the material systems with the negligible valence band offsets are chosen. The schematic of the device structure of IBTSC is shown in Fig. 3.30. The QDS in intrinsic layer consists of two parts. The top part has the smaller quantum dots and the bottom part has the lager quantum dots (or nanoparticles). The spacer materials and thickness in the top and the bottom parts are same. No tunnel junctions are required

for the connection in this particular structure. In each part, by tuning the dot size and dot spacing, the first miniband is designed to be inside the potential well so that it can act as an intermediate band (IB). The second and higher-index minibands are designed to be at the edge of the conduction band (CB) of the spacer material to act as the conduction band. An appropriate delta doping in the two parts makes both IBs half-filled to ensure the optical transitions through IB.

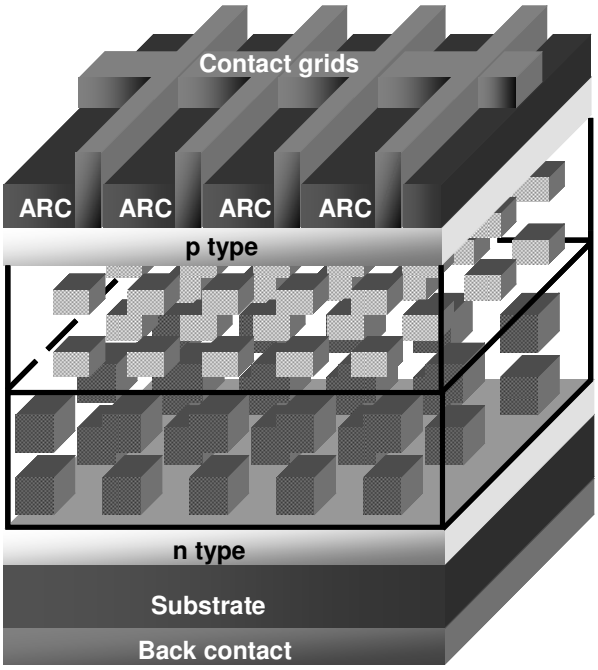

Fig. 3.30 Schematic illustration of quantum dot superlattices based IBTSC

Fig. 3.31 shows the energy band diagrams of IBTSC in the thermal equilibrium (a) and during the operation (b), respectively. In the thermal equilibrium (no sunlight illumination or applied bias), the Fermi level is a straight line throughout the whole device, which corresponds to the no-current flow condition. The bottom QDS has a shallow potential well as compared to the top QDS because of the lager dot sizes or different dot materials. Thus, there is a potential drop in the barrier layer between the two

QDS resulting from the IB alignment. Under sunlight illumination, the quasi-Fermi levels are separated by the population of photo-generated carriers. As a result, there are five available optical transitions for the photon absorption with different energies (Fig. 3.32). They are contributing to the short-circuit current. The open-circuit voltage, which is mainly determined by the band gap of barrier material, is maintained. This mechanism will help to harvest the low-energy photons, whose energies are even smaller than the lowest energy in conventional IBSC without degrading open-circuit voltage.

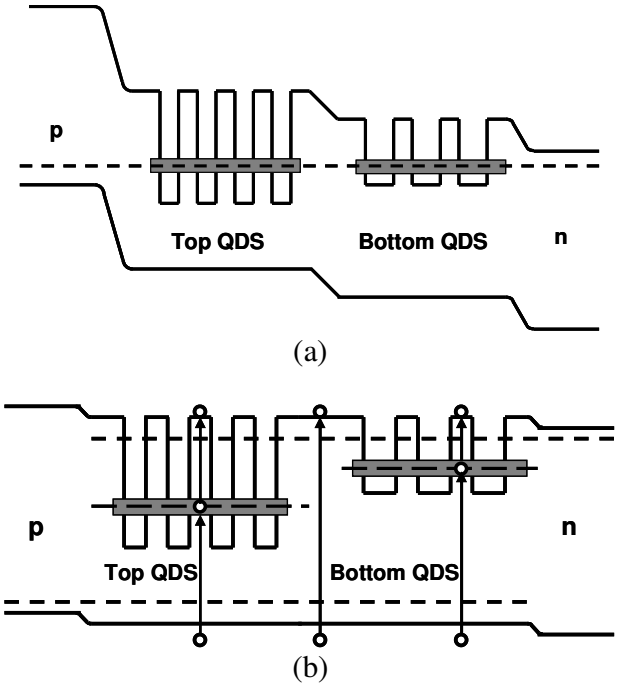

Fig. 3.31 Energy band diagrams of IBTSC without TJ in thermal equilibrium (a) and during operation (b).

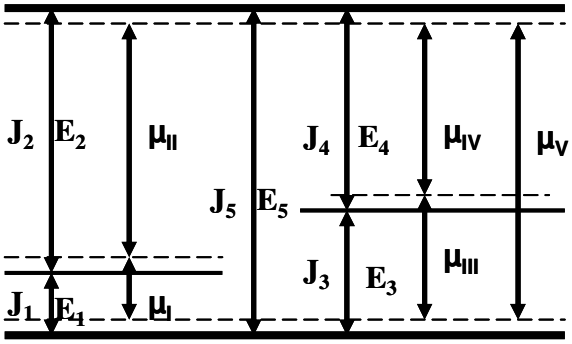

Fig. 3.32 Energy separations and current flow in IBTSC
$E_1+E_2=E_3+E_4=E_5$; $qV_{OC} = \mu_V = \mu_I + \mu_{II} = \mu_{III} + \mu_{IV}$; $J_1=J_2$; $J_3=J_4$; $J_{SC}=J_2+J_4+J_5$

Regarding the charge carrier transport (which defined the collection efficiency), the negligible valence band offset ensures that the holes transport freely in valence band and alignment of two high-index minibands (serving as the conduction band) by modulating the dot dimensions ensures the electrons transport freely in conduction band. Therefore, the efficiency of IBTSC is expected to be higher than that of IBSC. Note that this is not the four-band solar cell as proposed by Brown et al. [33], and there are no optical transitions between two IBs. The maximum efficiency of ~ 72% for the ideal four-band solar cell was reported by Green [34]. But the delta doping required in the four-band solar cell to make all the IBs half-filled would be extremely challenging technologically and the optical transitions between two IBs are considered to be extremely low. IBTSC can solve that problem by separating two IBs in top and bottom QDS and half-filling each IB. According to the detailed balance method, the theoretical upper bound efficiency of ~ 70.2% for IBTSC is obtained which is comparable to that in four bands solar cell.

We numerically simulated its operation and determined the upper bound efficiencies of ~ 70.2% which is much higher than that of the conventional IBSC (~ 63.2%) or conventional two-gap tandem cell (~ 55%) under fully concentrated light. The

efficiencies of IBTSC as a function of the energy level separation and chemical potential are listed in Table 3.3. Fig. 3.33 presents the maximum efficiency achievable with IBTSC structure vs the band-gap of the host matrix material under fully concentrated sunlight. The maximum efficiencies of two-gap tandem cell and IBSC are also shown as comparison. In this figure $GaAs_{0.98}Sb_{0.02}$ bandgap of 1.48eV is shown by dot dash line.

Table 3.3 Efficiencies for varied energy separations and chemical potentials in IBTSC

$E_5(eV)$	1.48	1.7	1.9	1.97	2.1	***2.2***	2.3	2.34	2.38	2.45	2.65
$E_2(eV)$	0.59	0.7	0.80	0.83	0.9	***0.95***	1.0	1.02	1.04	1.07	1.17
$E_1(eV)$	0.29	0.37	0.46	0.49	0.55	***0.60***	0.65	0.66	0.68	0.71	0.81
$\mu_{cv}(eV)$	1.39	1.59	1.77	1.84	1.96	***2.05***	2.14	2.19	2.22	2.29	2.48
Efficiency (%)	64.22	67.40	69.23	69.65	70.06	***70.17***	70.04	69.87	69.76	69.35	67.94

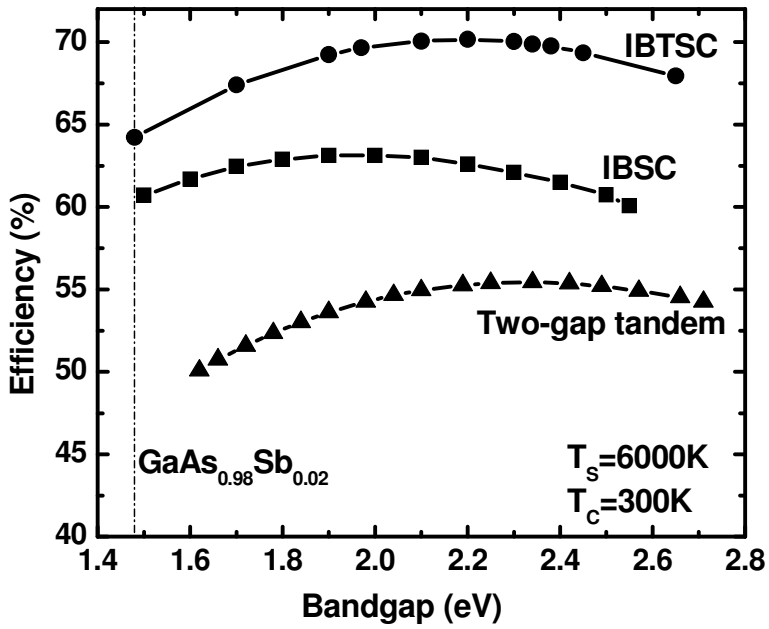

Fig. 3.33 Efficiency comparison among two-gap tandem cell, IBSC and IBTSC under fully concentrated sunlight, GaAsSb bandgap of 1.48eV is shown by dot dash line.

To physically implement IBTSC concept, we performed 3D analysis on an example of simple cubic QDS made of InAsN (quantum dots), InAsP (quantum dots) and GaAsSb (host matrix) materials system. $InAs_{0.9}N_{0.1}$, $InAs_{0.49}P_{0.51}$ and $GaAs0_{.98}Sb_{0.02}$ have negligible valence band offsets and the conduction band offsets are 1.29eV and 0.57eV for InAsN/GaAsSb (top QDS) and InAsP/GaAsSb (bottom QDS) respectively [25]. The values for the electron effective masses $m^*_{InAsN} = 0.0354m_0$, $m^*_{InAsP} = 0.0533m_0$ and $m^*_{GaAsSb} = 0.066m_0$ (m_0 is the electron rest mass) and other band parameters have been taken from Ref. [26]. Following the Lazarenkova and Balandin [12] semi-analytical approach, the electron dispersion in such structure is obtained by solving the Schrodinger equation. which gives the solution for 3D ordered QDS through the Kronig-Penny-type expression. The optimized dot sizes are 4.5 nm and 5.8 nm for InAsN and InAsP QDs respectively, and the dot spacing is 2nm for both subcells. The Fig. 3.34 shows the exact band diagram of the simple cubic QDS determined from the calculation of the energy separation and the bandwidth of the minibands following the semi-analytical approach. The dispersion is shown for the electron wave vector K along [[100]] quasi-crystallographic direction in the coordinate system formed by the quantum dots in QDS. The minibands are labeled by a symbol T (B) which means top cell or bottom cell and the quantum numbers $n_x n_y n_z$, which define the total energy of an electron as the sum of its component along three axes. The [[100]] direction is the most important one since it defines the charge carrier transport in the vertical direction to *n* and *p* type layers. One can see from Fig. 3.34 that the combined bands 211&112 are perfectly aligned and over

the barrier height V_B by tuning the quantum dot sizes to ensure the good transport performance of the charge carriers. The bandwidth of band 111 is 0.03 eV for both top cell and bottom cell.

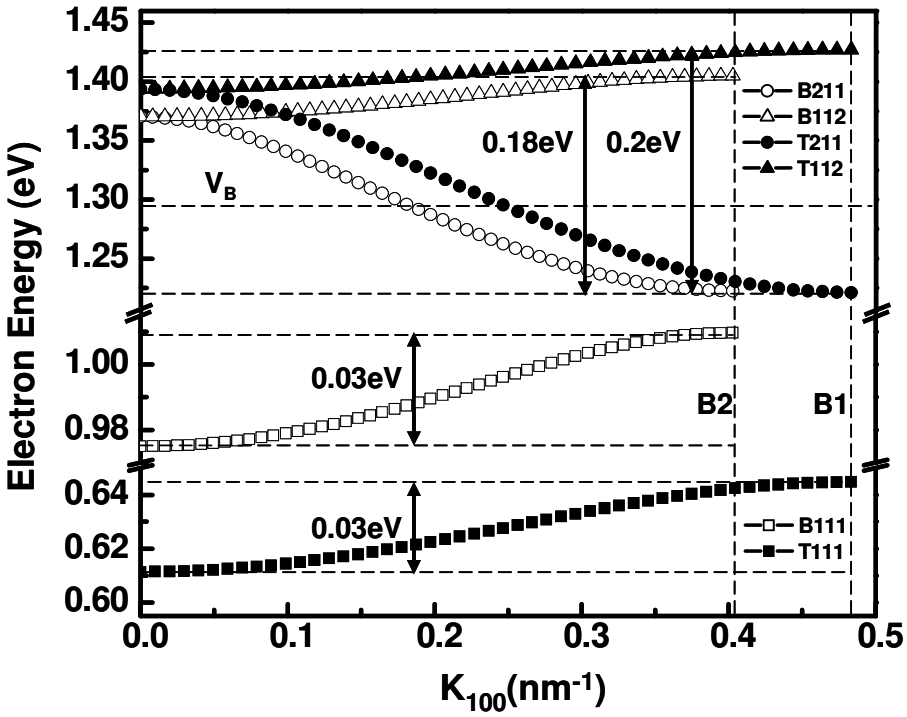

Fig. 3.34 Energy dispersion spectrum of the first three minibands in both top QDS (InAsN/GaAsSb) and bottom QDS (InAsP/GaAsSb). The energy is counted from the bottom of the potential well in top QDS. B1 and B2 are boundaries of quasi-Brillouni Zone for top QDS and bottom QDS respectively. V_B is barrier height. T(B)111, T(B)112 and T(B)211 denote the minibands 111, 112 and 211 in top (bottom) QDS respectively.

In Fig. 3.35, we depict the real-space band diagram for our structure with the calculated energies and miniband widths. Herein, the minibands 111 in both cells act as IBs while the overlapping minibands 211 and 112 act as the bands analogous to CB from where the generated electrons are extracted as a current flow. The higher-index

minibands whose energies are higher than barrier potential are mutually overlapping or very close to each other and be considered as a quasi-continuum CB. The VB in our structure is the same as in bulk semiconductors owing to the negligible valence band offsets.

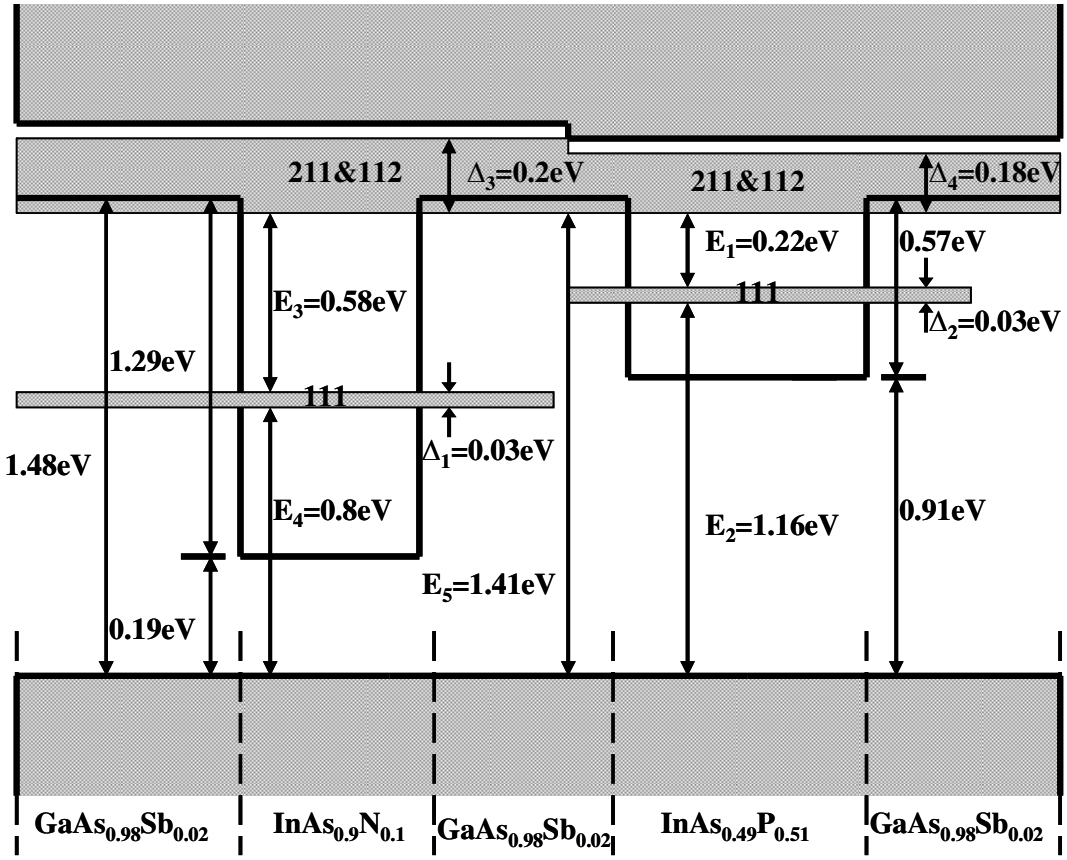

Fig. 3.35 Energy diagram of InAsN/InAsP/GaAsSb for implementation of IBTSC

In Fig. 3.33, the ideal-cell maximum efficiency of IBTSC based on $GaAs_{0.98}Sb_{0.02}$ system is ~ 64% based on the assumption that all the energy levels are in the optimum positions and can be tuned independently. In practical, when implemented by QDS structure, the both energy levels and bandwidth are associated with QDS dimensions and deviated from optimum ones. In our particular design, with the dimensions of 4.5 nm

InAsN QDs, 5.8 nm InAsP QDs and 2 nm dot spacing, the maximum efficiency of 61.05% is obtained with the following parameters: $E_1 = 0.22eV$; $E_2 = 1.16eV$; $E_3 = 0.58$ eV; $E_4 = 0.80$ eV; $E_5 = 1.41$ eV; $\Delta_1 = \Delta_2 = 0.03$ eV. The practical highest efficiency of conventional IBSC based on InAsN/GaAsSb is ~ 51% reported by the authors before [35]. Thus we demonstrate that the introduction of InAsP quantum dots layer to InAsN/GaAsSb based PV cell system can significantly increase the PV efficiency by 10% theoretically.

The introduction of tunnel junction between two subcells in IBTSC increases the power conversion efficiency further. In this design, the conduction bands of each subcell are not required to be aligned because the charge carriers can easily transport through tunnel junction. But, the quantum dot and the barrier material have to possess the negligible valence (conduction) band offsets in each subcell for the IB implementation. The barrier material of the bottom subcell can be selected different from that of the top subcell to ensure the wide spectrum absorption.

Figs. 3.36 (a) and (b) are the energy band diagrams of the IBTSC with TJ in the thermal equilibrium and during the operation. In the thermal equilibrium, the Fermi level is a straight line throughout the whole device, which corresponds to the no-current flow condition. During the operation, the top subcell can absorb the photons with an appropriate energy by either the direct excitation from VB to CB or the two-step excitation (VB to IB followed by IB to CB). The photo-generated carriers can tunnel through to the bottom subcell and be excited to CB again by either direct the excitation or the two-step excitation. In this way, both the open-circuit voltage and the short-circuit current are improved. The same or higher efficiency as compared to the first IBTSC embodiment (without the tunnel

junction) can be expected in the configuration. Fig. 3.37 shows the possible optical transitions of the charge carriers in IBTSC with TJ. The possible III-V materials combinations [25] are listed in Table 3.4 for embodiments of IBTSC with TJ. Note that each row of combinations in Table II is good for implementation of IBTSC without TJ.

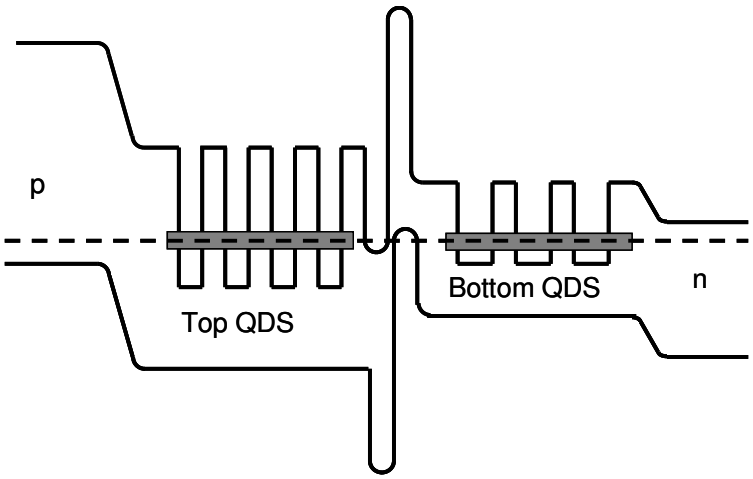

(a)

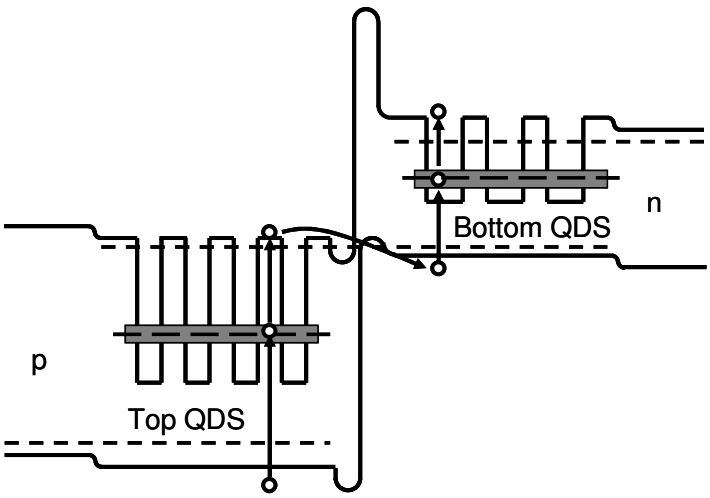

(b)

Fig. 3.36 Band diagram of the IBTSC with TJ in the thermal equilibrium (a) and during the operation (b)

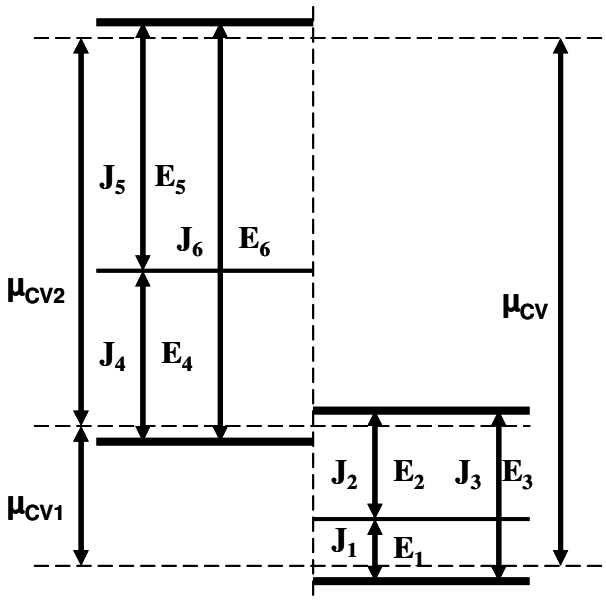

Fig. 3.37 Energy separation and current flow in IBTSC with tunnel junction

$E_1+E_2=E_3$; $E_4+E_5=E_6$; $J_4=J_5$; $J_1=J_2$; $J_2+J_3=J_5+J_6$; $J_{SC}=J_2+J_3$; $V_{OC}=\mu_{cv}$

Table 3.4 III-V materials combinations for implementation of IBTSC with TJ

Subcell Type	Barrier	$E_{g,barrier}$	Quantum Dot
Top Subcell	$AlAs_{0.56}Sb_{0.44}$	1.93eV	$InAs_{0.85}Sb_{0.15}$ $InP_{0.54}Sb_{0.46}$
Bottom Subcell	$GaAs_{0.98}Sb_{0.02}$	1.48eV	$InAs_{0.9}N_{0.1}$ $InAs_{0.49}P_{0.51}$ $InP_{0.82}Sb_{0.18}$

The difference of this design from IBTSC without TJ is that $AlAs_{0.56}Sb_{0.44}$ is selected for the barrier material in the top QDS instead of $GaAs_{0.98}Sb_{0.02}$, and $InAs_{0.85}Sb_{0.15}$ is selected for the quantum dot material in the top QDS instead of $InAs_{0.9}N_{0.1}$. The InAsSb/AlAsSb system has negligible valence band offsets, which is required for the IB

implementation. Two subcells are connected in series by the highly n (p)-type doped AlAsSb tunnel junction. The highly doped p-AlAsSb is used as an emitter in the top subcell. The obtained maximum efficiency of IBTSC with TJ is ~71% for the following combination of the band parameters: E_1=0.18eV; E_2=0.42eV; E_3=0.60eV; E_4=1.08eV; E_5=1.62eV; E_6=2.70eV; μ_{cv}=3.1eV; μ_{cv1}=0.552eV; μ_{cv2}=2.548eV.

3.4 COMSOL simulation of conical dots superlattices

COMSOL (FEMLAB) based on finite element method is applied to simulate 3D problems in QD solar cell. COMSOL multiphysics can solve coupled physics phenomena simultaneously, e.g. thermo-electrical coupling in solar cell when it is operated under concentrated sunlight. By solving Schrodinger equation and Poisson equation, one can get the electron wave functions for different energy states and potential profile. Based on them, energy dispersion, density of states, electrical conductivity, mobility, light absorption coefficient etc for this QDS layer could be calculated. Quantum dots may have many geometries including cylindrical, conical or pyramidal. Depending on the growth mechanisms of quantum dots, a 2D thin layer of material underneath quantum dots may or may not exist. In this part, I make the comparison of electron wavefunction ($\psi(\vec{r})$) and electron density ($\psi^*(\vec{r})\psi(\vec{r})$) in five-period quantum dot superlattices (QDS) structure with and without wetting layer. This work is focused on the physical properties in vertical direction since electron (hole) travel along this direction during solar cell operation. Fig. 3.38 is showing the schematic of InAs/GaAs quantum dot superlattices structure. The dots are separated far away from each other in X-Y plane, so there are no electron wavefunctions coupling. Coupling only takes place along the growth direction (z

direction). Technically, it is very difficult to make quantum dots well ordered in X-Y plane by self-assembly method. But, it is relatively easy to make them grow compactly and align along z direction because of the strain-driven growth.

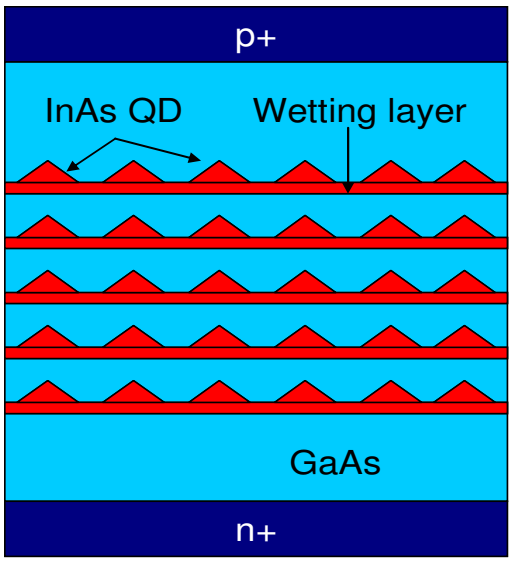

Fig. 3.38 Schematic of InAs/GaAs quantum dot superlattices solar cell

The major parameters used in this simulation are listed below:

Conical dot height: 4 nm;

Dot base (diameter): 24 nm;

Wetting layer thickness: 0.8 nm;

Dot spacing (z direction): 2 nm;

Effective mass (GaAs): 0.067 m_0;

Effective mass (InAs): 0.023 m_0;

Barrier height for electron: 0.697 eV;

Dielectric constant (GaAs): 12.9;

Dielectric constant (InAs): 15.15.

One band Schrodinger equation for electron can be expressed as:

$$-\frac{\hbar^2}{2}\nabla\cdot(\frac{1}{m_e^*(\vec{r})})\nabla\psi(\vec{r})+V_e(\vec{r})\psi(\vec{r})=E\psi(\vec{r}), \tag{3.22}$$

where $\hbar$ is reduced Planck's constant, $m_e^*(\vec{r})$, $\psi(\vec{r})$, $V_e(\vec{r})$, and E are position dependent electron effective mass, electron envelop function, potential energy, and electron total energy. Since quantum dot is assumed to have perfect cylindrical symmetry, one can separate wavefunciton $\psi(\vec{r})$ into

$$\psi(\vec{r})=\chi(z,r)\Phi(\phi), \tag{3.23}$$

where ϕ is the azimuthal angel and $\chi(z,r)$ is an envelop function.. Then rewrite equation Y.1 in cylindrical coordinates as:

$$\begin{aligned}&-\frac{\hbar^2}{2}\frac{\partial}{\partial z}(\frac{1}{m_e^*(z,r)}\frac{\partial\chi_n}{\partial z})-\frac{\hbar^2}{2}\frac{1}{r}\frac{\partial}{\partial r}(\frac{r}{m_e^*(z,r)}\frac{\partial\chi_n}{\partial r})+\frac{\hbar^2}{2m_e^*(z,r)}\frac{n^2}{r^2}\chi_n(z,r),\\&+V_e(z,r)\chi_n(z,r)=E\chi_n(z,r)\end{aligned} \tag{3.24}$$

$$\Phi(\phi)=\exp(in\phi), \tag{3.25}$$

where n is an integer for Φ to be a single-valued function: $\Phi(0)=\Phi(2\pi)$. Note that this is an instance of a Partial Differential Equation (PDE) on coefficient form,

$$\nabla\cdot(-c\nabla u-\alpha u+\gamma)+\alpha u+\beta\cdot\nabla u=d_\alpha\lambda u, \tag{2.26}$$

where the nonzero coefficients are $c=\frac{\hbar^2}{2m_e^*}$, $\alpha=\frac{\hbar^2}{2m_e^*}\frac{n^2}{r^2}+V$, $\beta=-\frac{\hbar^2}{2m_e^*}\frac{1}{r}$, $d_\alpha=1$ and $\lambda=E_n$.In this part, only n=0 case is considered since it is defining the electron/hole carrier transport direction. Detailed derivation is shown in reference [36].

3.4.1 QDS structure without wetting layer

The first ten eigenvalues for electron energy (eV) calculated are 0.355, 0.365, 0.380, 0.397, 0.412, 0.614, 0.626, 0.643, 0.665 0.685 eV respectively. Fig. 3.39, 3.40 show the envelop functions $\psi(\vec{r})$ (left panel) and electron densities $\psi^*(\vec{r})\psi(\vec{r})$ for ground state and the first excited state respectively. For low energy levels (e.g. the ground state and the 1st excited state), the electron is highly localized in the center of the quantum dot. The one dimensional electron envelop functions along z direction for ground state and the first excited state are shown in Fig. 3.41.

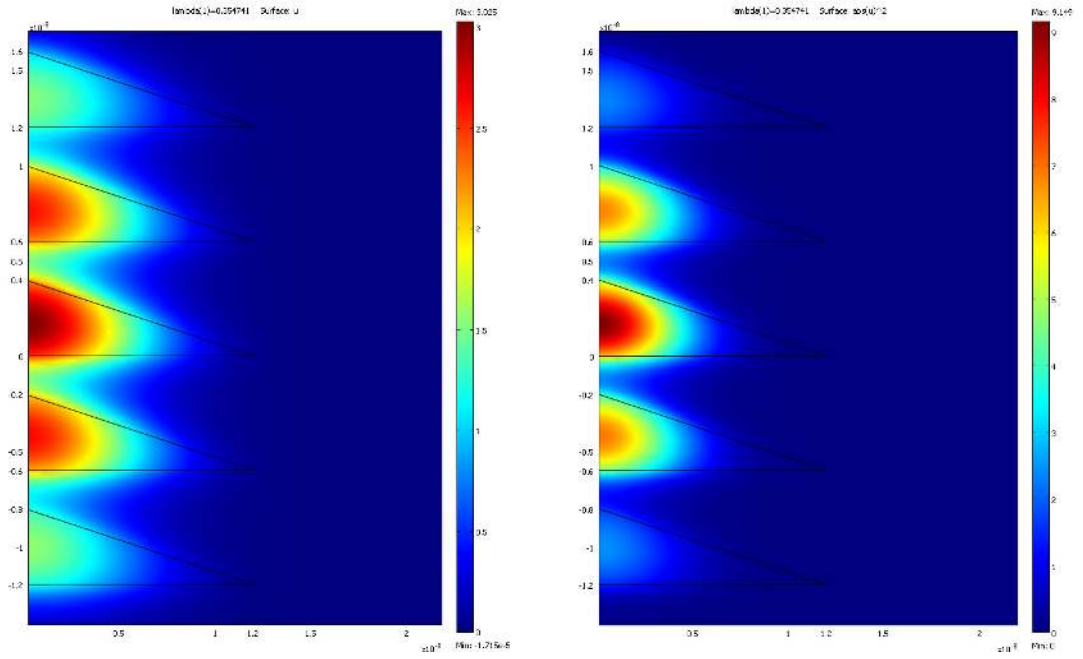

Fig. 3.39 The ground state envelop function (left) and electron density (E = 0.355 eV) without wetting layer

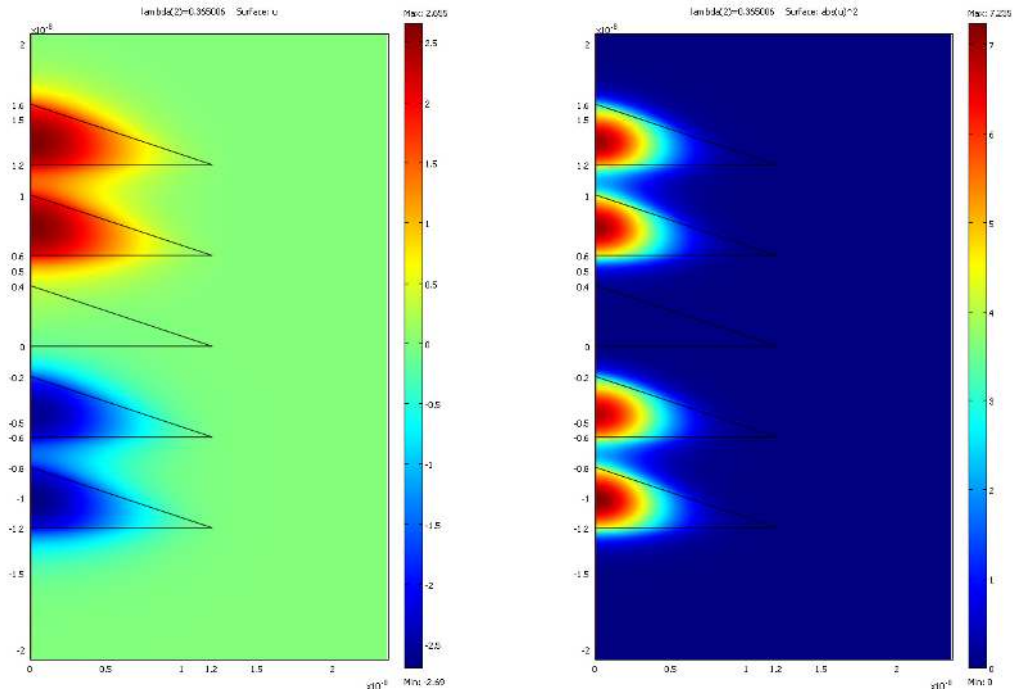

Fig. 3.40 1st excited state envelop function (left) and electron density (E = 0.365 eV) without wetting layer

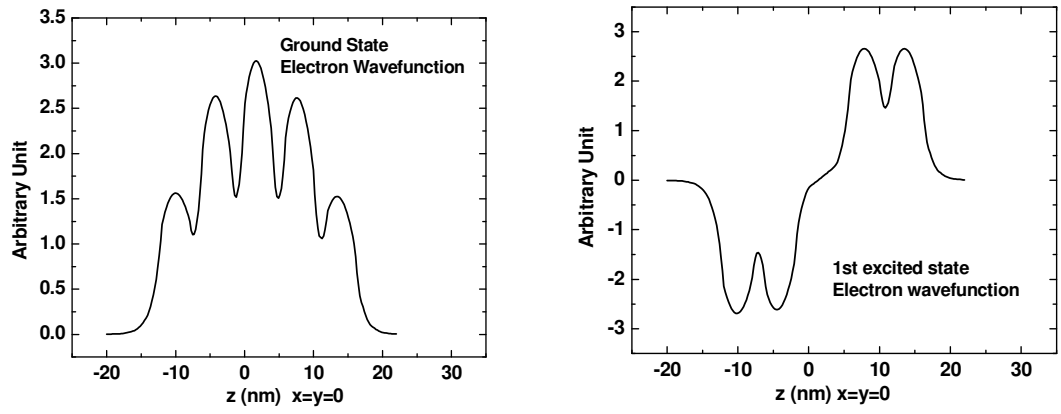

Fig. 3.41 1D electron envelop wavefunction along z axis (x = y = 0) for the ground state (left) and the 1st excited state without wetting layer

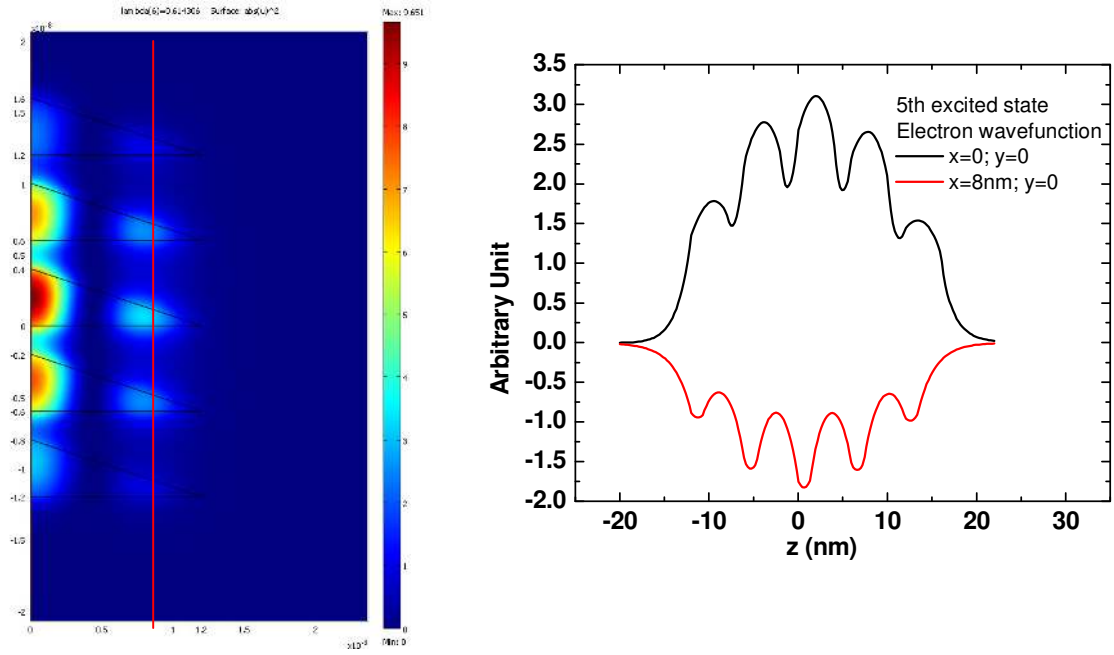

Fig. 3.42 5th excited state electron density (left) and 1D electron wavefunctions along z axis in the center and corner of QD without wetting layer (x = y = 0 and x = 8 nm, y = 0)

Fig. 3.42 shows the electron density for the 5th excited state (left panel) and 1D electron envelop wavefunctions along z axis in the center (x = y = 0) and corner (x = 8 nm, y = 0) in the structure. For higher energy levels (e.g. the 5th excited state), electron has chance to travel to the quantum dot corner. But it is still localized inside the quantum dot. The magnitude of wavefunction at corner (x = 8 nm) is smaller than that in the center (x = 0). Fig. 3.43 shows the electron envelop function (left panel) and electron density for energy of 0.70 eV which is higher than the electron barrier height: 0.697 eV. With high electron energy above the barrier height, the electron can not be localized inside quantum dot any more, and it starts to travel to the barrier materials regime.

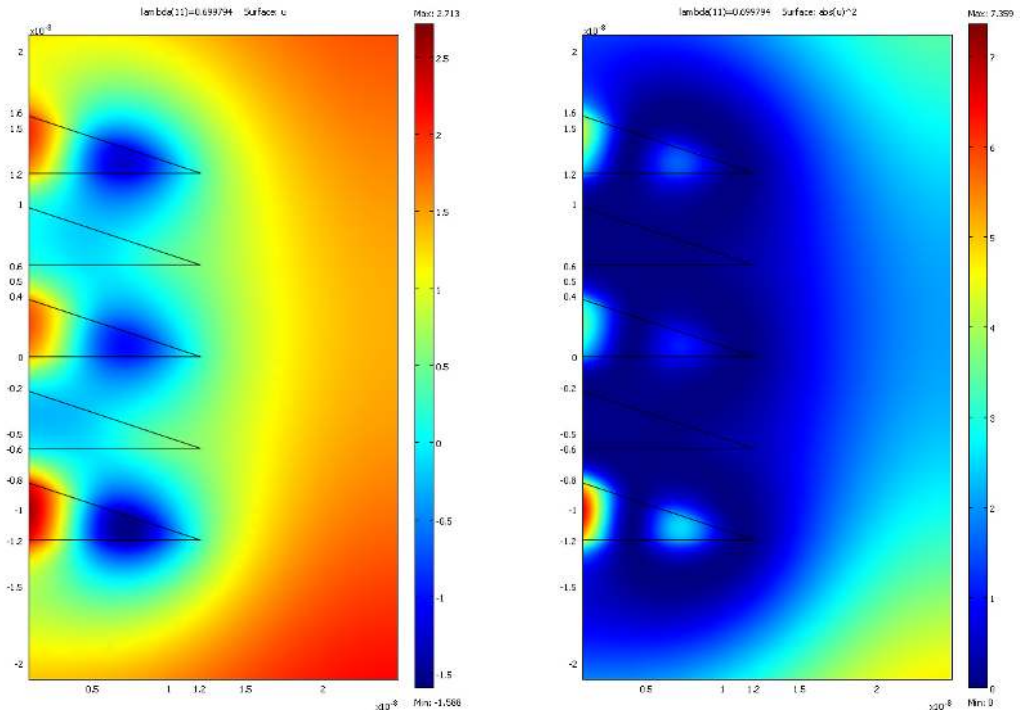

Fig. 3.43 Electron envelop function (left) and electron density with energy higher than barrier height (E = 0.70 eV) without wetting layer

3.4.2 QDS structure with wetting layer

The first ten eigenvalues for electron energy (eV) are calculated as: 0.319, 0.330, 0.347, 0.366, 0.382, 0.554, 0.565, 0.580, 0.581, 0.591 eV. Compared to those without wetting layer, the corresponding energy value is smaller. That is because the introduction of wetting layer makes the quantum confinement effect in quantum dot weaker. Fig. 3.44 is showing the electron envelop function and electron density for the ground state (0.319 eV). The electron is highly localized inside the quantum dot which is same as that in QDS without wetting layer. Fig. 3.45 is showing an excited state electron density (left) and the 1D electron wavefunction in wetting layer (x = 25 nm) at 0.608 eV. With higher

energy (e.g. 0.608eV), the electron is traveling to the corner of quantum dot and the wetting layer.

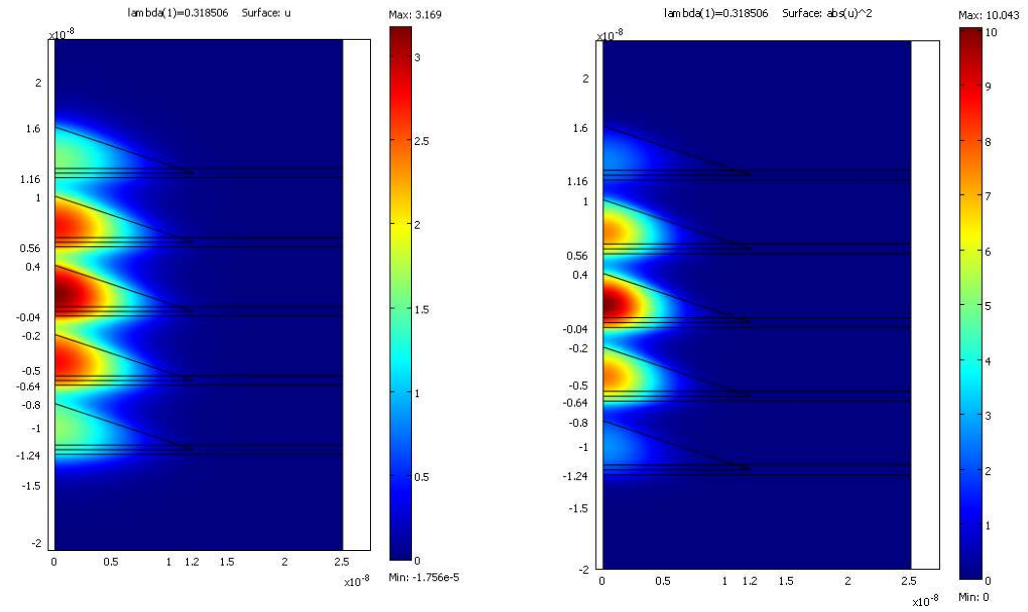

Fig. 3.44 The ground state electron envelop function (left) and electron density with wetting layer (E = 0.319 eV)

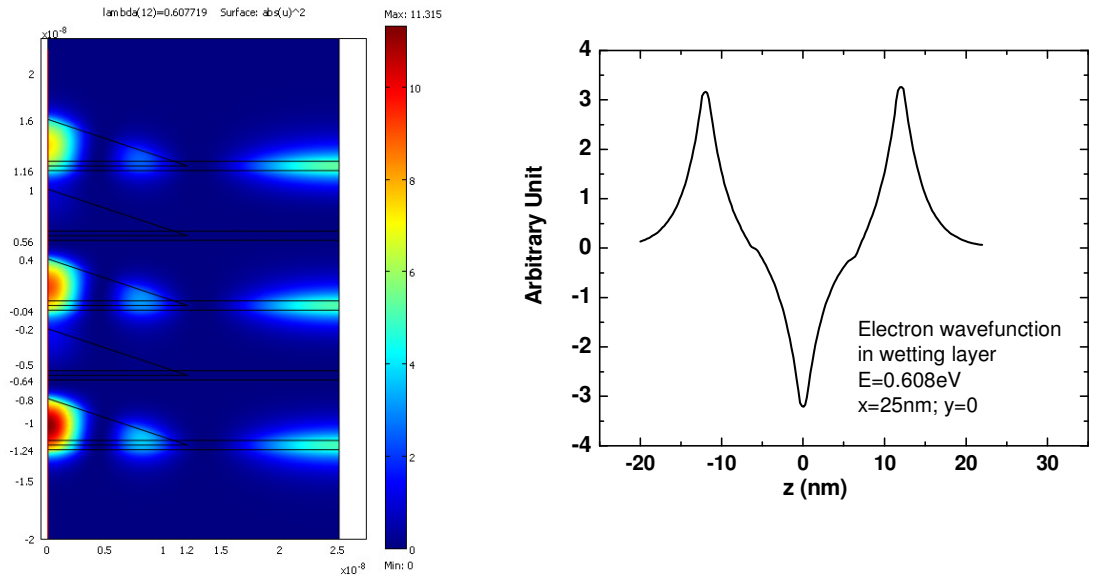

Fig. 3.45 An excited state electron density (left) and 1D electron wavefunction in wetting layer (x = 25 nm) (E = 0.608 eV)

3.4.3 PV efficiency calculation by COMSOL

Based on the calculation method for eigenvalues of electron energy in QDS by COMSOL, QDS structure for solar cell application is simulated and upper-bound efficiency is obtained. Fig. 3.46 shows the mesh generated by COMSOL in QDS structure. The total thickness of absorber is 100 nm. The major parameters used in this simulation are listed below: Conical dot height: 4 nm; Dot base (diameter): 10 nm; Dot spacing (z direction): 2 nm; Effective mass of quantum dot ($GaAs_{0.98}Sb_{0.02}$): 0.066 m_0; Effective mass ($InAs_{0.9}N_{0.1}$): 0.0354 m_0; Barrier height for electron: 1.29 eV.

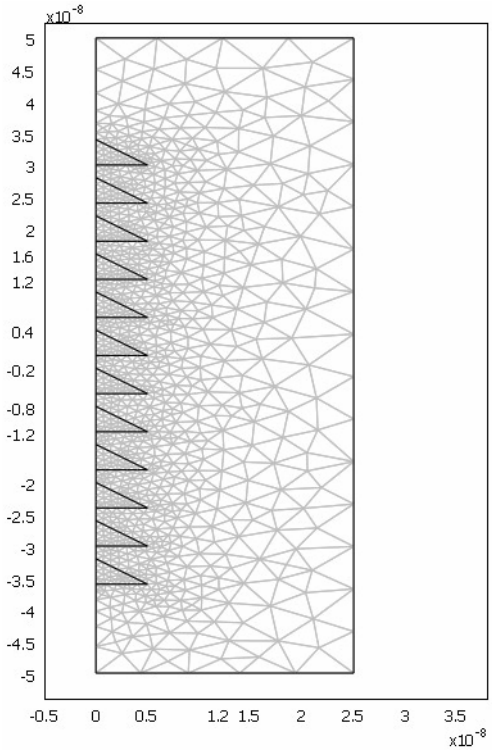

Fig. 3.46 Mesh generated by COMSOL in QDS structure

The electron densities are shown in Fig. 3.47 (a) and (b) for ground state and the state (1.290138 eV) just above the barrier height, respectively. The electron is totally confined in the QDS regime at the ground state and starts traveling out of QDS regime at the energy state which is higher than the barrier height (1.29 eV).

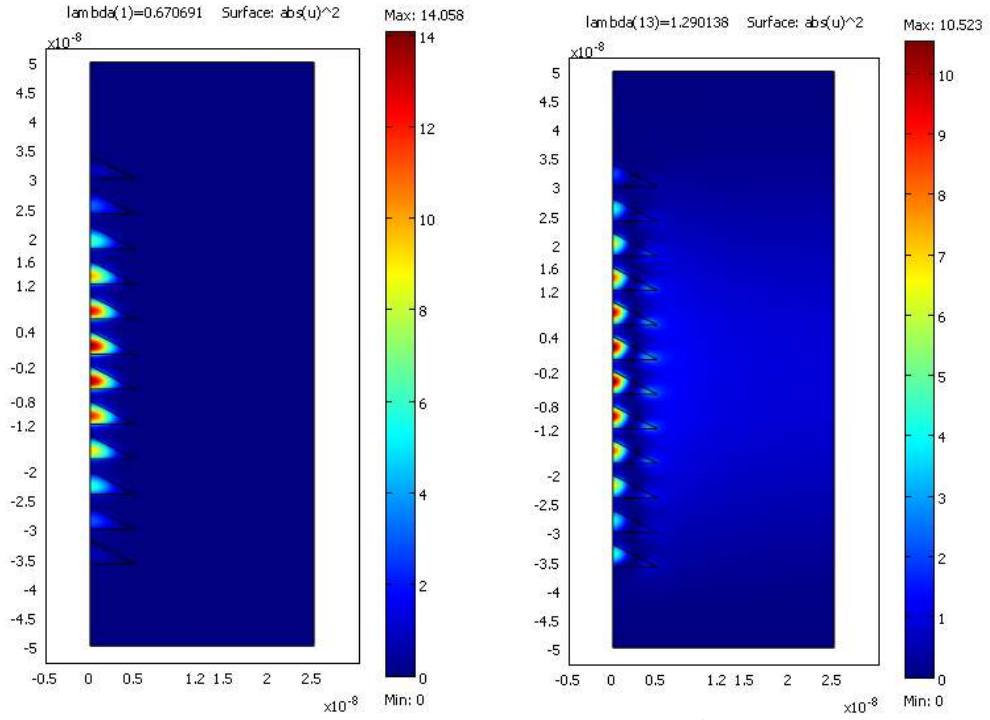

(a) (b)

Fig. 3.47 Electron densities for ground state (a) and the state just above the barrier height (b) in QDS structure

In Fig. 3.48, the energy separations and bandwidth of intermediate band are specified. The calculated power conversion efficiency is 51.21% under fully concentrated sunlight with V_m *1.39V*, and J_m 2.7×10^3 *A/cm*^{2} which is very close to the calculated efficiency of 51.24% based on the semi-analytical approach. The efficiency is 33.46% under one sun illumination with *Vm* of *0.95 V* and *Jm* of *56.6 mA/cm*^{2}.

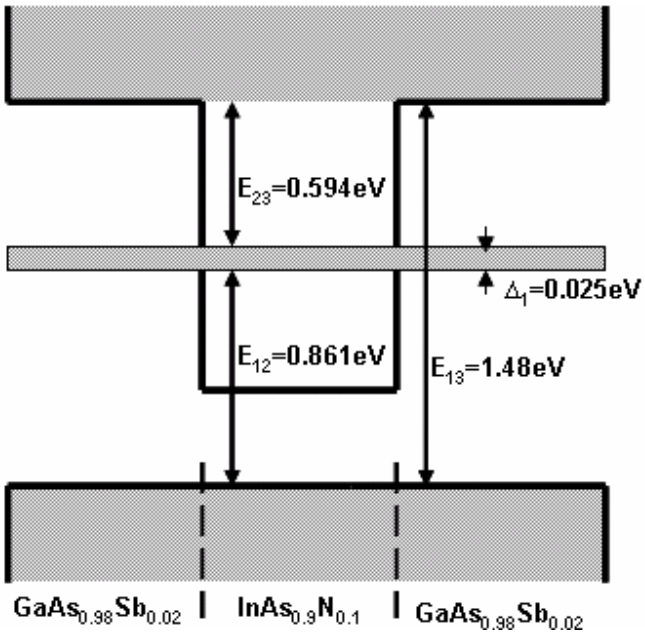

Fig. 3.48 Energy diagram in $InAs_{0.9}N_{0.1}/GaAs_{0.98}Sb_{0.02}$ quantum dot supra-crystal along [[100]] quasi-crystallographic direction

Reference

[1] J. F. Geisz, Sarah Kurtz, M. W. Wanlass, J. S. Ward, A. Duda, D. J. Friedman, J. M. Olson, W. E. McMahon, T. E. Moriarty, and J. T. Kiehl, "High-efficiency GaInP/GaAs/InGaAs triple-junction solar cells grown inverted with a metamorphic bottom junction," Appl. Phys. Lett. 91, 023502 (2007).

[2] K. Tanabe, A. F. Morral, H. A. Atwater, D.J. Aiken, and M.W. Wanlass, "Direct-bonded GaAs/InGaAs tandem solar cell," Appl. Phys. Lett. 89, 102106 (2006).

[3] C. S. Jiang, D. J. Friedman, J. F. Geisz, H. R. Moutinho, M. J. Romero, and M. M. Jassim, "Distribution of built-in electrical potential in $GaInP_2$/GaAs tandem-junction solar cells," Appl. Phys. Lett. 83, 1572 (2003).

[4] M. K. Herndon, W. C. Bradford, R. T. Collins, B. E. Hawkins, T. F. Kuech, D. J. Friedman, and S. R. Kurtz, "Near-field scanning optical microscopy cross-sectional measurements of crystalline GaAs solar cells," Appl. Phys. Lett. 77, 100 (2000).

[5] T. Soga, T. Jimbo, G. Wang, K. Ohtsuka, and M. Umeno, "Hydrogen plasma passivation of GaAs on Si substrates for solar cell fabrication," J. Appl. Phys. 87, 2285 (2000).

[6] J. Singh, Physics of Semiconductors and Their Heterostructures, McGraw-Hill Series in Electrical and Computer Engineering, New York (1993).

[7] T. Tiedje, E. Yablonovitch, G. D. Cody, and B. G. Brooks, "Limiting efficiency of silicon solar cells," IEEE Trans. Electron Devices 31, 711 (1984).

[8] P. T. Landsberg, and G. Tonge, "Thermodynamic energy conversion efficiencies," J. Appl. Phys. 51, R1-R20 (1980).

[9] A. Luque and A. Marti, "Increasing the efficiency of ideal solar cells by photon induced transitions at intermediate levels," Phys. Rev. Lett. 78, 5014 (1997).

[10] M. Wolf, "Limitations and Possibilities for Improvement of Photovoltaic Solar Energy Converters," Proceedings of *IRE* 48, 1246-1263 (1960).

[11] M. A. Green, Photovoltaic Applications of Nanostructures, in Handbook of Semiconductor Nanostructures and Nanodevices, (ASP, 2006; ISBN: 1-58883-077-2) Vol. 4, edited by A. A. Balandin and K. L. Wang, pp. 219-237.

[12] O. L. Lazarenkova, and A. A. Balandin, “Miniband formation in a quantum dot crystal,” J. Appl. Phys. 89, 5509 (2001).

[13] S. Facsko, T. Dekorsy, C. Koerdt, C. Trappe, H. Kurz, A. Vogt, and H. L. Hartnagel, “Formation of Ordered Nanoscale Semiconductor Dots by Ion Sputtering,” Science, 285, 1551 (1999).

[14] Y. I. Mazur, W. Q. Ma, X. Wang, Z. M. Wang, G. J. Salamo, M. Xiao, T. D. Mishima, and M. B. Johnson, “InGaAs/GaAs three-dimensionally-ordered array of quantum dots,” Appl. Phys. Lett. 83, 987 (2003).

[15] S. Kiravittaya, M. Benyoucef, R. Zapf-Gottwick, A. Rastelli, and O. G. Schmidt, “Ordered GaAs quantum dot arrays on GaAs(001): Single photon emission and fine structure splitting,” Appl. Phys. Lett. 89, 233102 (2006).

[16] J. S. Kim, M. Kawabe, and N. Koguchi, “Ordering of high-quality InAs quantum dots on defect-free nanoholes,” Appl. Phys. Lett. 88, 072107 (2006).

[17] A. A. Balandin, K. L. Wang, N. Kouklin and S. Bandyopadhyay, “Raman spectroscopy of electrochemically self-assembled CdS quantum dots,” Appl. Phys. Lett. 76, 137 (2000).

[18] A. A. Balandin, G. Jin and K. L. Wang, “Issues of practical realization of a quantum dot register for a quantum computer,” J. Electron Materials, 20, 549 (2000).

[19] J. L. Liu, W. G. Wu, A. A. Balandin, G. L. Jin, Y. H. Luo, S. G. Thomas, Y. Lu and K. L. Wang, “Observation of inter-sub-level transitions in modulation-doped Ge quantum dots,” Appl. Phys. Lett. 75, 1745 (1999).

[20] O. L. Lazarenkova, and A. A. Balandin, “Electron and phonon energy spectra in a three-dimensional regimented quantum dot superlattice,” Phys. Rev. B 66, 245319 (2002).

[21] A. Marti, N. Lopez, E. Antolin, E. Canovas, C. Stanley, C. Farmer, L. Cuadra and A. Luque, “Novel semiconductor solar cell structures: The quantum dot intermediate band solar cell,” Thin Solid Films, 511-512, 638-644 (2006).

[22] D. L. Nika, E. P. Pokatilov, Q. Shao, and A. A. Balandin, “Charge carrier states and light absorption in the ordered quantum dot superlattices,” Phys. Rev. B. 76, 125417 (2007).

[23] L. D. Landau and E. M. Lifchitz, Statistic Physics (Nauka, Moscow, 1989).

[24] W. Shockley and H. J. Queisser, “Detailed balance limit of efficiency of p-n junction solar cells,” J. Appl. Phys. 32, 510 (1961).

[25] M. Y. Levy, C. Honsberg, A. Marti, and A. Luque, “Quantum dot intermediate band solar cell material systems with negligible valence band offsets,” Proceedings of the 31st IEEE Photovoltaic Specialists Conference, pp. 90-93. (Jan. 2005).

[26] I. Vurgaftman, J. R. Meyer, and L. R. Ram-Mohan, “Band parameters for III-V compound semiconductors and their alloys,” J. Appl. Phys. 89, 5815 (2001).

[27] T. S. Navruz and M. Saritas, “Efficiency variation of the intermediate band solar cell due to the overlap between absorption coefficients,” Solar Energy Materials and Solar Cells 92, 273, (2008).

[28] A. Luque and A. Marti, “A metallic intermediate band high efficiency solar cell,” Prog. In Photovolt: Res. Appl. 9, 73, (2001).

[29] P. Campbell and M. A. Green, “The limiting efficiency of silicon solar cells under concentrated sunlight,” IEEE Trans. Electron Devices, 33, 234 (1986).

[30] L. Cuadra, A. Marti and A. Luque, “Influence of the overlap between the absorption coefficients on the efficiency of the intermediate band solar cell,” IEEE Trans. Electron Devices, 51, No.6, 1002, (2004).

[31] A. D. Vos, “Detailed balance limit of the efficiency of tandem solar cells,” J. Phys. D: Appl. Phys. 13, 839 – 846 (1980)

[32] A. S. Brown and M.A. Green, “Intermediate band solar cell with many bands: Ideal performance,” J. Appl. Phys. 94, 6150 (2003)

[33] A. S. Brown, M.A. Green and R.P. Corkish, “Limiting efficiency for a multi-band solar cell containing three and four bands,” Physica E 14, 121 – 125 (2002).

[34] M. A. Green, “Prospects for photovoltaic efficiency enhancement using low-dimensional structures,” Nanotechnology, 11, 401 (2000).

[35] Q. Shao, A.A. Balandin, A.I. Fedoseyev and M. Turowski, “Intermediate-band solar cells based on quantum dot supracrystals,” Appl. Phys. Lett. 91, 163507 (2007)

[36] R. Melnik and M. Willatzen, “Band structure of conical quantum dots with wetting layers,” Nanotechnology, vol. 15, pp. 1-8, (2004)

CHAPTER 4

TRANSPARENT GRAPHENE ELECTRODES FOR NEXT GENERATION LIGHT-WEIGHT SOLAR CELLS

Current solar array technologies provide specific energies in the range of 20 - 40 Watts/kg when the solar array deployment system and the solar array drive are considered. Future NASA deep-space exploration missions will require improvements in the photovoltaic efficiency of solar panels and power to weight ratio in order to reduce the spacecraft weight. Nano-structured semiconductors with excellent mechanical strength and light-weight are required to advance the current state of practice.

Optically transparent is also important for solar cell electrodes to extract power out and allow sunlight go through as much as possible. These electrodes are usually made from indium tin oxide (ITO), because of its high conductivity and good light transmittance. The indium element is becoming scarce and expensive because of the great demand by optoelectronic applications such as liquid crystal display (LCD), light-emitting diode (LED) and solar cell etc. It is expected to be exhausted in next decade. One other major problem of ITO is the migration of indium and oxygen into the active region of optoelectronic device to degrade the device performance. This has made the search for novel transparent electrode materials with good stability, high transparency and excellent conductivity a crucial goal for optoelectronic researchers.

4.1 Fabrication and characterization of graphene electrodes

A novel type of the transparent and light-weight electrodes can be made of single layer graphene (SLG), bi-layer graphene (BLG) or few-layer graphene (FLG) for solar cell applications and any other applications, which require transparent electrical conductors. The electrodes are expected to perform better in the solar cells than the conventional transparent conducting oxide (TCO) window electrodes. Graphene is a single layer of carbon atoms. It is extremely thin, i.e. only one atomic layer thick, optically transparent, chemically inert, thermally reliable and excellent conductor of electricity and heat. The extremely high thermal conductivity of graphene was reported by Dr. Balandin's group [1-2]. Graphene is expected to be stable at very high temperature up to few thousand degrees Celsius and at the same time be as hard as diamond similar to a one dimensional carbon nanotube. The simulated current density endurance of graphene can be as high as ~ 10^{12} A/m^2. It is extremely flexible, i.e. can be bent to different shapes, which is important for some specific electric connections. The uniqueness of graphene is that it is the only known strictly two-dimensional crystal. Graphene can be relatively easily integrated with other materials and devices structures due to its flat (planar) geometry and can form good Ohmic contacts.

The electron mobility of graphene is extraordinary high with the experimentally determined values of 15000 cm^2/Vs at room temperature (RT) and 10^6 cm^2/Vs at liquid-helium temperature [3]. These unique physical properties make this two-dimensional crystal ideally suitable for the optical window electrodes in optoelectronic devices. Narrow ribbons made of graphene preserve most of the transport

properties of graphene while also allow to open a band gap in this material, which changes its optical characteristics.

The resistivity of conventional ITO is around 0.7 - 1 mΩ·cm, thus the sheet resistance is around 47 - 67 Ω/□ for 150 nm ITO thin film which is the typical thickness in organic solar cell application [4]. At the same time, it is principally not possible to reduce the thickness of ITO to anything close to the atomic layer thickness of graphene. If one hypothetically reduced ITO thickness further down to 0.35 nm (the thickness of graphene), the sheet resistance would be around 20 - 30 kΩ/□ which is comparable to the reported sheet resistance value of the worst quality graphene made from thermal reduced graphene oxide [5]. The resistance of the mechanically exfoliated or epitaxially grown graphene is always much lower that that of the chemically produced from graphene oxide. This demonstrates the graphene has the resistivity smaller than that of ITO while being much superior in terms of chemical and thermal stability over conventional ITO.

Fig. 4.1 shows SLG, BLG and FLG mechanically exfoliated in our laboratory. The exact number of layers has been confirmed by the micro-Raman spectroscopy through the 2D-band deconvolution method reported by Dr. Balandin's group [6-9]. The accurate procedure for distinguishing the number of graphene layers on arbitrary substrates is done through the Raman spectrum features [8-9].

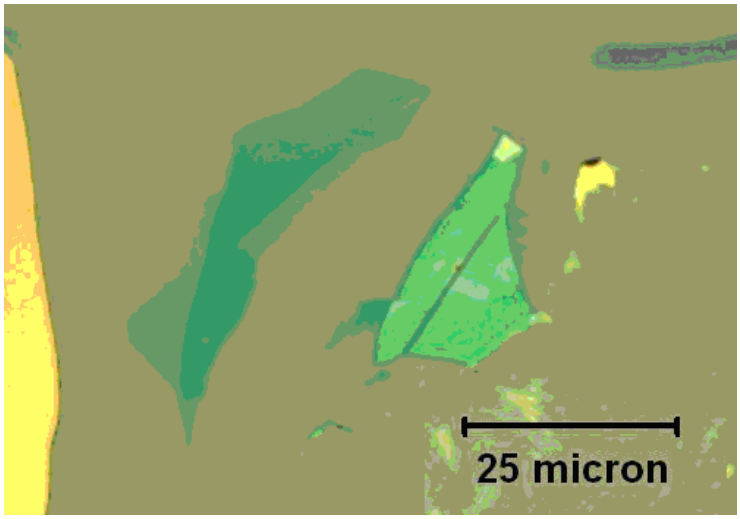

Fig. 4.1 Optical microscopy image of single layer, bilayer and few layer graphene

Micro-Raman spectrums were measured at RT using Renishaw instrument under 488 nm excitation wavelength in the backscattering configuration [7-9]. Fig. 4.2 shows characteristic Raman spectrum with clearly distinguishable *G* peak and *2D* band. The position of *G* peak and shape of *2D* band confirm that the examined flake is SLG. The disorder-induced *D* peak is absent in the scattering spectra from High Pressure High Temperature (HPHT) graphene (its expected position indicated by an arrow), which suggests a high quality of SLG material.

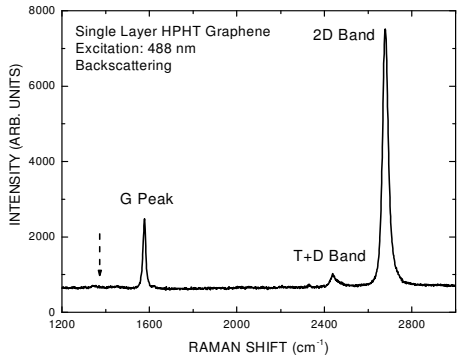

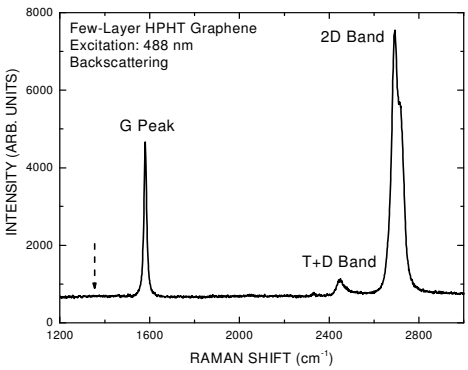

Figure 4.2 Raman spectra for identification of graphene and accurate counting of the number of atomic layers.

On top of being the most light-weight, excellent electrical conductor and extraordinary heat conductor, graphene offers excellent transparency to the solar spectrum. The latter is the crucial requirement for window electrodes, i.e., transparent electrodes. We tested the graphene transparency by measuring the Raman spectra from the suspended SLG and comparing it with those from the calibration graphite samples. The exact procedure for the measurements is outlined in our publications [1-2]. We found that the transmittance of suspended SLG test sample for the visible light with the wavelength of 488 nm was ~ 95%. This compares well with the conventional ITO. At the same time, the amount of conventional ITO material, which needs to be used to provide electrical conductance, is much larger than that for the graphene electrodes. Our experimental values are in line with the recently reported transmittance data for 10 nm thick graphite layers [10]. It was reported in Ref. [10] that the transmittance through the graphite layer of 10-nm thickness (corresponding to ~ 28 layers of graphene) is about 60%. The increase in the number of atomic layers (SLG → BLG → FLG) leads to some reduction of the optical transmittance but increased mechanical strength. Each specific design should use the optimum number of layers.

To test the electrical properties of graphene conductors, Graphene layers have been transferred to Si substrates with the electrically insulating oxide films of thickness W ≥0.3 μm grown on top of them. A set of SLG and BLG conductors contacted by platinum (Pt) electrodes have been fabricated using Leo XB1540 Focused Ion Beam (FIB) system. The absence of leakage current through the oxide layer was verified by applying very

high bias (up to ~20 V) between the top electrodes and back gate (metallization on the back side of the Si substrate) and ensuring the resulting current is negligibly small. The graphene conductors between two metal electrodes on insulating oxide layer, which can be considered as prototype graphene interconnects, have been electrically characterized in the temperature range T=300 – 500K. The temperature was controlled externally through the Signatone probe-station hot chuck. In Fig. 4.3 we present typical current-voltage (I-V) characteristics for SLG interconnect fabricated from Highly Ordered Pyrolytic Graphite (HOPG) material and BLG interconnect fabricated from HPHT material. Fig. 4.4 shows scanning electron microscopy (SEM) images of SLG conductor (a) and BLG conductor (b) between two Pt electrodes respectively. The electrical properties of interconnects made of HOPG and HPHT graphene were similar for the examined set of samples. As one can see the contacts are Ohmic and the current increases with increasing temperature. Such a behavior is characteristic for intrinsic semiconductors where the electrical conductivity σ_i obeys the following temperature dependence [11] $\sigma_I \sim exp\{-\Delta E_i/(2k_BT)\}$ (here ΔE_i is the band-gap and k_B is the Boltzmann's constant). The decreasing resistance of semiconductors with T is due to growing concentration of the thermally generated electron-hole pairs. It is influenced by the band-gap renormalization and carrier scattering on phonons as the temperature changes [11].

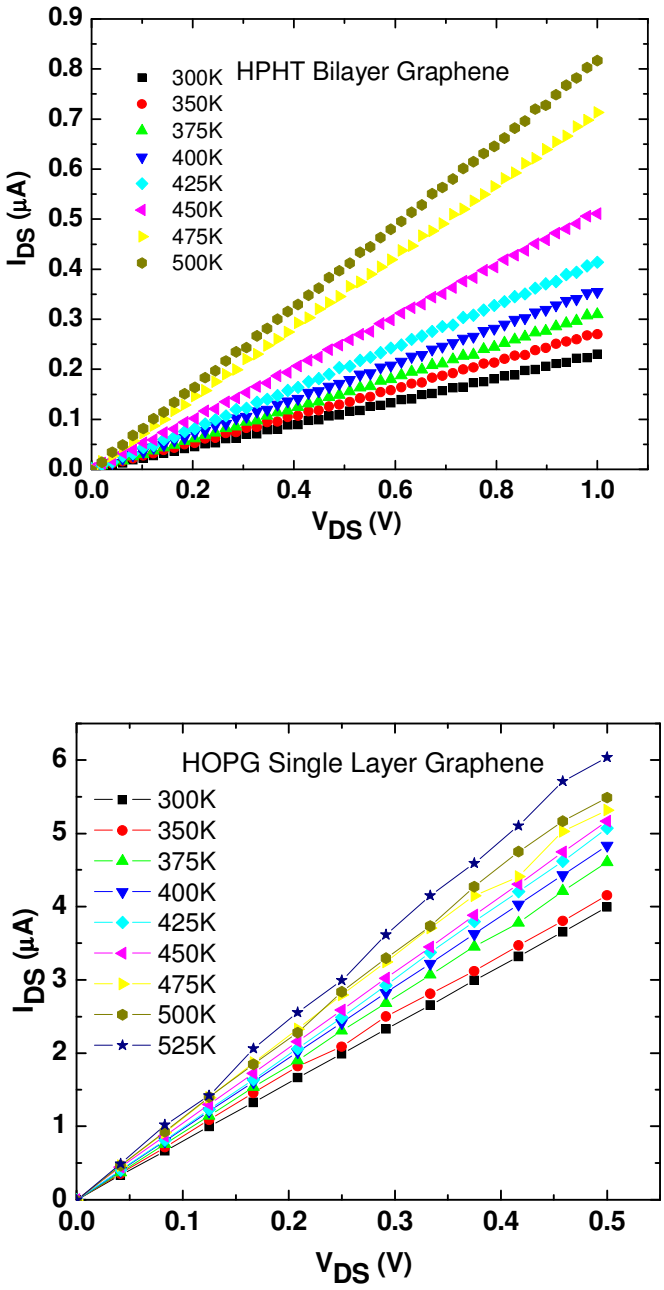

Figure 4.3 Current – voltage characteristics of graphene electrodes contacted by metal wires at different temperatures. The top panel shows the result for bi-layer graphene electrodes produced by HTHP method. The bottom panel shows the results for

single-layer graphene produced from HOPG graphite. The test results confirm that the contacts are Ohmic and that the resistance decreases with temperature.

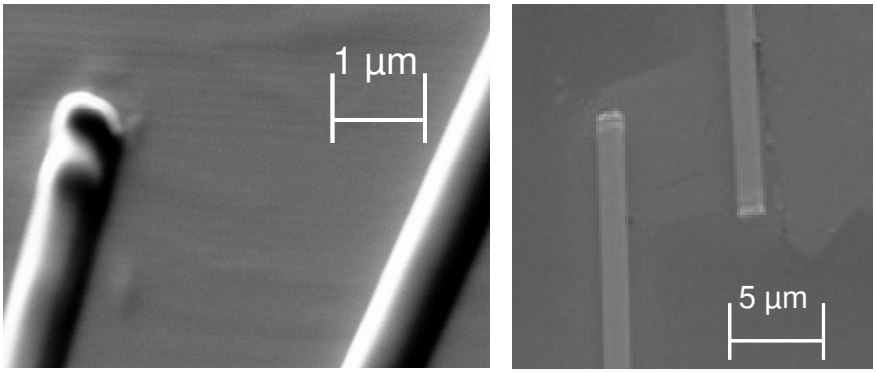

(a) (b)

Fig. 4.4 Scanning Electron Microscopy images of (a) single layer graphene conductor and (b) bi-layer graphene conductor

It is interesting to note that the measured trend in graphene is opposite of that in bulk semimetals of bismuth type (e.g. Bi_xSb_{1-x}, Bi-Ti, Bi-Sn) where resistivity ρ follows the law [12] $\rho=\rho_o+AT$ (here A is a positive constant between (2.3 – 14) x 10^{-7} Ωcm/K). Such dependence for semimetals and metals is explained by the increasing electron – phonon scattering at elevated temperature [13]. In metals the number of charge carriers does not change with temperature but the interaction with phonons increases. The latter results in the temperature dependence of the type $R=R_o[1+\alpha(T-T_o)]$, where α is the temperature coefficient of resistance. At low temperature resistance is limited by impurities, which leads to increasing mobility and decreasing resistance with T. The temperature dependence of resistance in bismuth near RT reverses when one makes a nanostructure out of it, e.g. nanowire, with the lateral dimensions below some critical value. In this case a semimetal – semiconductor transition is induced by quantum confinement, which

results in the experimentally observed change in the resistance temperature dependence [14].

The solar concentrators are frequently used with photovoltaic devices to improve the energy conversion efficiency. So the typical operating temperature for concentrator photovoltaic cells (CPV) is 100 K – 200 K higher than room temperature. The theoretical efficiency of the crystalline silicon solar cells with the solar concentrator can increase from ~ 30% to approximately ~ 40% with concentrated sunlight. However the concentrated light can generate additional amount of heat that will degrade the device performance. This explains an additional benefit of having the top transparent electrode with the improved electrical conductivity at elevated temperatures for the PV cells with solar concentrators. Thus graphene transparent electrodes might be particular useful for PV cells and modules with the solar concentrators. Moreover, when the amount of heat dissipated in solar cells increases the thermal conductivity of the window electrodes is becoming another crucial parameter. The graphene transparent electrodes are unique in this sense as well.

Fig. 4.5 presents the electrical resistance for SLG and BLG interconnects as a function of temperature. The resistances were normalized to their values at RT for better comparison. The plot also shows a theoretical curve for the SLG conductor obtained from the model recently proposed by Vasko and Ryzhii [15] and re-normalized to RT value for better comparison. Our experimentally obtained dependence for SLG is in excellent agreement with the calculations. According to the theory proposed in Ref. [15] the decrease in resistance at RT and above comes from the thermal generation of carriers while the values and shape of the resistance curve are determined by electron and hole

scattering on the long and short range disorder and acoustic phonons. Cheianov and Falko [16] also predicted a negative linear T dependence of resistivity $R(T)$ in graphene described by the expression $R(T)=R(0)-(h/e^2)(4TV_o/hv^2E_F\tau_o)$, where h is the Plank's constant, e is the charge of an electron, E_F is the Fermi energy, τ_o is a backscattering rate from atomically sharp defects in graphene lattice, which does not include Coulomb scatterers, v is the velocity, and V_o is a characteristic interaction constant [16]. For our samples we obtained the following linear analytical approximation for the high-temperature normalized resistance of SLG: $R(T)/R(T=300\text{K})=1.436 - 0.00147T$. From the known characteristic velocity in graphene of $V_F\sim10^8$ cm/s and the experimentally determined temperature when the resistance quenching sets up (~300 – 350K) we can estimate the correlation length for the disorder scattering in our graphene resistors [15], i.e., $l_c\sim V_Fh/(2\pi Tk_B)$, to be around 22 – 25 nm. The origin of the difference in the resistance temperature dependence for SLG and BLG requires further theoretical and experimental investigation. One should note here that the data in Ref. [15] was plotted for maximum R near the neutrality point while Ref. [16] considered the "heavily-doped" case.

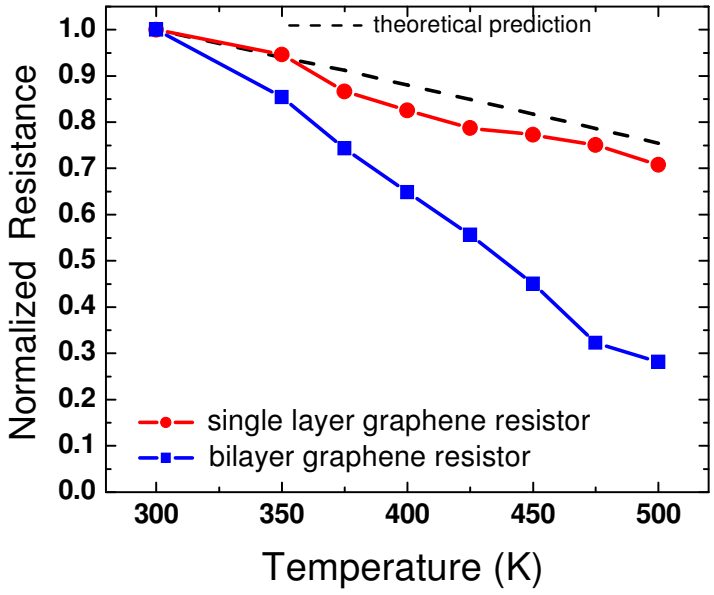

Fig. 4.5 Normalized resistances of SLG and BLG resistors at high temperature

It is illustrative to compare electrical resistance of graphene with that of bulk graphite and other carbon materials. It was known for a long time that single graphite crystals are good electrical conductors along the graphite planes and very poor ones across with the ratio of resistivities above ~10^4 [17]. There is substantial discrepancy for the reported temperature dependence of the electrical resistance in bulk graphite, which likely can be attributed to the variations in the material quality. From the data presented in Ref. [18-19], the resistance decreases with increasing temperature around RT although in one case the decrease in sub-linear while in another case it is superlinear. The high-temperature resistance decreases with temperature in the coke base carbon (T=300 – 800K) and graphitized lampblack base carbon (T=300 – 2000K) as summarized in Ref. [20] although the dependence is very different from what we have measured for graphene. In

some types of carbon, e.g. graphitized coke base carbon, the decreasing trend reverses to increasing resistivity around 400-500K [20].

Researchers in Balandin's group reported that the thermal conductivity of single layer graphene is in the range of 4800 – 5300 W/mK [1-2] at RT, which is around 4000 times larger than that of conventional ITO electrodes (~ 1.2 W/mK) [21]. It is also much larger than the thermal conductivity of diamond – the best bulk solid thermal conductor. The extremely high value of the thermal conductivity suggests that graphene can even outperform carbon nanotubes (CNTs) in heat conduction. In addition to transporting electrical current, the graphene electrodes can also serve as superb heat spreaders and remove the heat generated by high energy photons. The extremely high thermal conductivity of graphene window electrodes is extremely beneficial for the PV cells operated under the highly concentrated sunlight.

4.2 COMSOL simulation of thermal electrical properties of graphene electrodes

As the electronic industry aggressively moves towards nanometer designs thermal issues are becoming increasingly important for the high-end electronic chips. The integrated circuit (IC) performance is now limited by the maximum power, which can be dissipated without exceeding the maximum junction temperature setup by the reliability requirements [22-24]. According to the International Technology Roadmap for Semiconductors (ITRS) projections the volumetric heat generation rates within interconnects will be approaching $P=j^2\rho$ ~3.3 x 10^7 W/cm^3 assuming a current density j=3.9x10^6 A/cm^2 and a resistivity ρ=2.2 μΩcm. The self-heating problem is aggravated by the increased integration densities, faster clock speed, high dissipation power density,

increased total thermal boundary resistance of the chip layers, incorporation of the alternative dielectric materials with low thermal conductivity values as well as acoustic phonon confinement effects in nanometer scale structures [25-27].

Concentrated Photovoltaic (CPV) cells have been demonstrated to possess higher PV efficiency than those under one sun illumination. But severe self-heating problem is caused by the highly concentrated sunlight. One of the approaches to mitigate the problem is to incorporate into the solar cell design the materials with low electrical resistance and high thermal conductivity for electrodes. Graphene, a single layer of carbon atoms arranged in a hexagonal sp^2 lattice, was proposed for the transparent electrodes [28-29] as well as interconnect applications [30-35]. It manifests extremely high room temperature (RT) electron mobility as high as ~15000 $cm^2V^{-1}s^{-1}$. Graphene also has very low resistivity that can reach a value of ~10^{-6} Ohm-cm [36-37]. This value is comparable to that of silver, if not less. The resistivity of graphene is approximately twice less than the resistivity of copper, the most widely used material for interconnection metal wires. It was also recently discovered that the thermal conductivity of single layer graphene is very large and reaches the values of 3080 – 5300 $Wm^{-1}K^{-1}$ [1-2]. Such thermal conductivity is substantially higher than the thermal conductivity of copper, which is 400 $Wm^{-1}K^{-1}$. It adds validity to the proposed interconnect applications of graphene owing to potential benefit for thermal management. In this case, graphene interconnects may be used for high-heat flux cooling and help with lateral heat spreading and hot-spot removal. The very low resistivity of graphene, coupled with its very high thermal conductivity, can be the core of new interconnect technologies, where graphene ribbons-planes are used as components of interconnect lines. The interconnect lines,

made of graphene, can provide with shorter signal propagation times and, meanwhile, efficiently remove heat from devices.

Investigation of thermal and electrical properties of graphene ribbons is essential for advanced interconnect engineering. The electrical current passing through the graphene ribbon generates heat by Ohmic heating, which leads to the increasing temperature of the ribbon. At the same time, the rising temperature can alter the intrinsic electric conductivity of the ribbon. Thus the thermal and electrical properties of the graphene ribbon are functionally dependent. In this work we studied effects of Ohmic heating to see how the maximum temperature and resistance of the graphene ribbon can be modified by changing current densities and dimensions of the ribbon.

The design of graphene-based interconnect networks can definitely benefit from preliminary simulation studies in which some of basic current propagation phenomena are modeled. In this work we looked into in-plane direct current propagation through a single-layered graphene ribbon.

COMSOL Multiphysics software package [38] is used to simulate the direct current (DC) propagation in the graphene ribbon. The essence of the COMSOL package is that it applied a finite element analysis method to solve partial differential equations in closed structures. User of the software creates a model of an object with specific geometry, internal parameters and boundary conditions. COMSOL divides the modeled object into a set of components and solves the differential equation within each component through linearization. Specific physics phenomena is described and defined through specific software modules. The variables that correspond to the physics laws, characteristic to specific modules, can be functionally dependent one on another, thus different modules

can be mathematically linked. In our case we utilize physics equations described through two modules: Heat Transfer by Conduction and DC Conductive Media.

The graphene ribbon is simulated as a three-dimensional parallelepiped object with finite dimensions. In this simple object the current flows in one direction from one side to another, and those sides are thermally connected to heat sinks. The constant thickness of the ribbon is assigned to be 0.35 nm. While the geometry is essentially three-dimensional, it is assumed that the heat propagates isotropically in two dimensions, in plane parallel to the largest surfaces of the 3-D object. The direct current is flowing through the ribbon, also, parallel to the largest surfaces of the parallelepiped, but just in one direction from one short side to another. Fig. 4.6 shows the ribbon seen from top. *L* and *W* indicate the length and the width of the ribbon which has a rectangular shape, if seen from top. The surfaces are conventionally indexed as 1, 2, 3, and 4. The inward direct current *I* is shown as a plurality of right-to-left arrows directed toward the side 3.

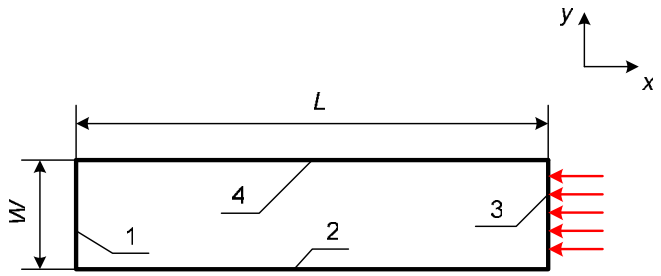

Fig. 4.6 Geometry of the modeled graphene ribbon, viewed from top, with shown direction of the inward current.

The direct current conduction in graphene ribbon is described by Ohm's law as

$$-\nabla \cdot d(\sigma \nabla V - J^e) = 0, \tag{4.1}$$

where d = 0.35 nm is the thickness of the ribbon, σ[S/m] is the electric conductivity, V [V] is the potential along the ribbon, and J^e [A/m^2] is the external current density. The electric field is tangential to the *xy*-plane, the electric potential varies in the *x* and *y* directions and is constant in the *z* direction.

For simplicity, to define a one-directional current flow, the boundary conditions are set in a way that the surfaces 2 and 4 are electrically insulated:

$$n \cdot J = 0, \tag{4.2}$$

the surface 1 is grounded to $V = 0$, and an inward current flow goes through the surface 3:

$$-n \cdot J = J_n, \tag{4.3}$$

where J_n [A/m^2] is the normal current density and n is the unit vector normal to a surface under consideration.

The heat conduction by diffusion in the ribbon is expressed using Fourier's law

$$-\nabla \cdot (k \nabla T) = Q, \tag{4.4}$$

where Q [W/m^3] is the heat source, T [K] is the temperature along the ribbon, and k [Wm^{-1}K^{-1}] is the thermal conductivity of graphene. Boundaries are set as the surfaces 2 and 3 are thermally insulated:

$$n \cdot (k \nabla T) = 0, \tag{4.5}$$

and the surfaces 1 and 3 are kept at the constant temperature of the heat sinks T_0 = 300 K.

The direct current creates a heat source Q in the ribbon. Thus, by changing the normal current density and the thermal conductivity, one can obtain simulated results for electrical and thermal components of the model.

We looked at different parameters that might be affected by the direct current and consequential Ohmic heating in the ribbon. Through all simulation runs the electric conductivity of single-layer graphene was assumed to be temperature dependent:

$$\sigma = \frac{\sigma_0}{1 + d(T - T_0)}, \tag{4.6}$$

where T_0 = 300 K, σ_0 = 8.35 x 10^5 S/m, and d = -0.00147 K^{-1}. The parameters $_0$ and d were calculated from fitting the experimental data of resistances of single-layered graphene resistors. That experiment was studying a temperature dependent modification of the resistances when the temperature of the resistor varied from 300 K to 500 K [39].

The thermal conductivity of single-layer graphene was measured to be approximately within the range of 3080 – 5300 $Wm^{-1}K^{-1}$ [1-2]. In that experiment the rectangular 5 x 23 μm graphene flake was used, and it was assumed, for simplicity, that the thermal conductivity is independent of the temperature and lateral dimensions of the flake. Recently it was theoretically shown that the expected value of the thermal conductivity of single-layer graphene is affected by temperature and dimensions of the flake [40]. For simulation studies of direct current propagation in graphene we chose two values of the thermal conductivity, 3500 $Wm^{-1}K^{-1}$ and 5000 $Wm^{-1}K^{-1}$, since they are well within the experimental range. We, first, fixed the dimensions of the graphene ribbon and set the length and the width to be L = 5 μm and W = 1 μm, respectively. According to the theory [40], we corrected the thermal conductivity of graphene for the temperature and width dependence as

$$k = k_0 \frac{T_0}{T} \frac{F}{F_0}, \tag{4.7}$$

where k is the corrected value of the thermal conductivity, k_0 is the uncorrected ("experimental reference") value of the thermal conductivity, which equals to either 3500 $Wm^{-1}K^{-1}$ or 5000 $Wm^{-1}K^{-1}$, T is the actual temperature at a particular point on the flake, and T_0 is the average temperature of the 5 x 23 μm rectangular ribbon, which was used when the thermal conductivity was measured experimentally [1-2]. The correction factors F_0 and F are

$$F_0 = -\ln\left\{\left|\exp\left(\frac{\hbar\omega_{\min}^0}{k_B T_0}\right)-1\right|\right\}+\frac{\hbar\omega_{\min}^0}{k_B T}\frac{\exp\left(\frac{\hbar\omega_{\min}^0}{k_B T_0}\right)}{\exp\left(\frac{\hbar\omega_{\min}^0}{k_B T_0}\right)-1}, \tag{4.8}$$

and

$$F = -\ln\left\{\left|\exp\left(\frac{\hbar\omega_{\min}}{k_B T}\right)-1\right|\right\}+\frac{\hbar\omega_{\min}}{k_B T}\frac{\exp\left(\frac{\hbar\omega_{\min}}{k_B T}\right)}{\exp\left(\frac{\hbar\omega_{\min}}{k_B T}\right)-1}, \tag{4.9}$$

where k_B is the Boltzmann constant, $\hbar$ is the Planck constant, and $\omega_{\min}^0$ and $\omega_{\min}$ are the minimum cut-off phonon frequencies [40].

The minimum cut-off phonon frequency depends on the temperature and the width of the ribbon, and it can be expressed as

$$\omega_{\min}^0 = \frac{v}{\gamma}\sqrt{\frac{Mv}{k_B T_0}\frac{\omega_{\max}}{d_0}}, \tag{4.10}$$

and

$$\omega_{\min} = \frac{v}{\gamma}\sqrt{\frac{Mv}{k_B T}\frac{\omega_{\max}}{d}}, \tag{4.11}$$

where d is the actual studied width and d_0 = 5 μm is the width of the graphene rectangular flake during the experiment. Note that in the equations (4.10) and (4.11) v is the average phonon velocity, γ is the Gruneisen parameter, M = 3.986 x 10^{-26} kg is the mass of a graphene unit cell, and $\omega_{\max}$ is the maximum cut-off phonon frequency.

Computing $\omega_{\min}^{0}$ and $\omega_{\min}$ can be simplified under an assumption that the cut-off frequency is approximately the same for both transverse and longitudinal phonon branches, thus only longitudinal branch numeric parameters for v, γ and $\omega_{\max}$ can be used. Those values are v = 21.3 km/s, γ= 1.8 and $\omega_{\max}$ = 238.5 THz [40]. Then, we can write

$$\omega_{\min}^{0} = \frac{1433}{\sqrt{d_0 T_0}}, \tag{4.12}$$

and

$$\omega_{\min} = \frac{1433}{\sqrt{dT}}. \tag{4.13}$$

In both (12) and (13) the frequency, the width and the temperature are expressed in THz, microns and Kelvins, correspondingly.

For every simulation run we corrected the original value of the thermal conductivity, 3500 $Wm^{-1}K^{-1}$ or 5000 $Wm^{-1}K^{-1}$, to account for its temperature dependence and dependence on the width of the ribbon. The average temperature T_0 was found to be 403 K and 372 K for the width d_0 = 5 μm and for the thermal conductivities 3500 $Wm^{-1}K^{-1}$ and 5000 $Wm^{-1}K^{-1}$, respectively [41].

Fig. 4.7 and Fig. 4.8 present the results of the simulated electric conductivity and temperature along the length of the ribbon. The current density is assigned to be constant and equal to J_n = 1.5 x 10^{11} A/m^2. It is seen that the passing current causes heating in the ribbon. Subsequently, the heating affects the electric conductivity of the ribbon. The temperature of the ribbon has the maximum in the middle of the ribbon, which is reasonable, since surfaces 1 and 3 are connected to the heat sinks. The maximum temperature of the ribbon is approximately 339 K and is 13 % higher compared to the temperatures of the heat sinks (T_0 = 300 K). The electric conductivities at the heat sinks and in the middle of the ribbon are approximately 8.35 x 10^5 S/m and 8.86 x 10^5 S/m, correspondingly. The electric conductivity in the middle of the ribbon is 6.1 % larger compared to the electric conductivity at the heat sinks.

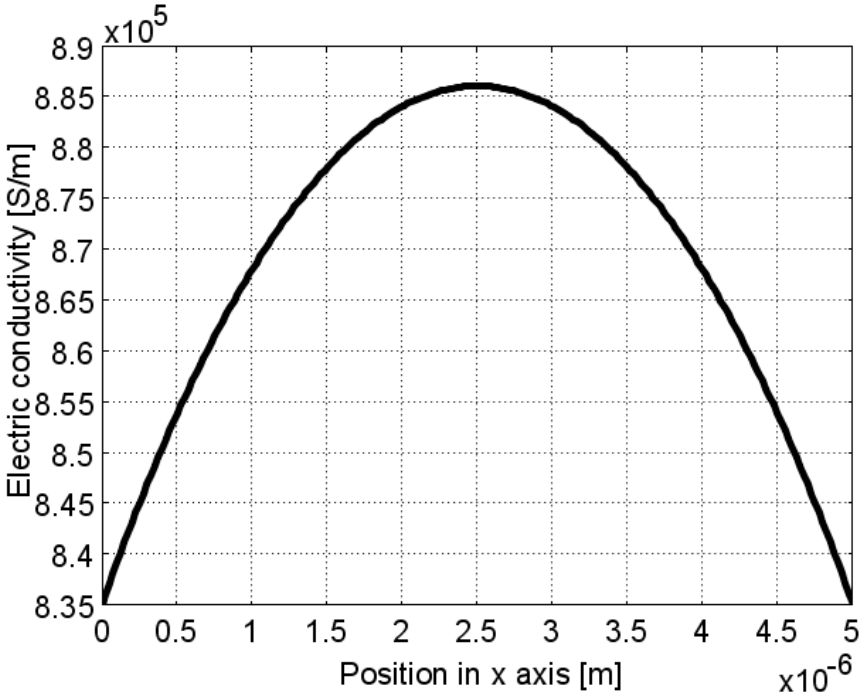

Fig. 4.7 Electric conductivity of the graphene ribbon along the length. The thermal conductivity k_0 is equal to 5000 $Wm^{-1}K^{-1}$ and the current density is equal to 1.5 x 10^{11} A/m^2.

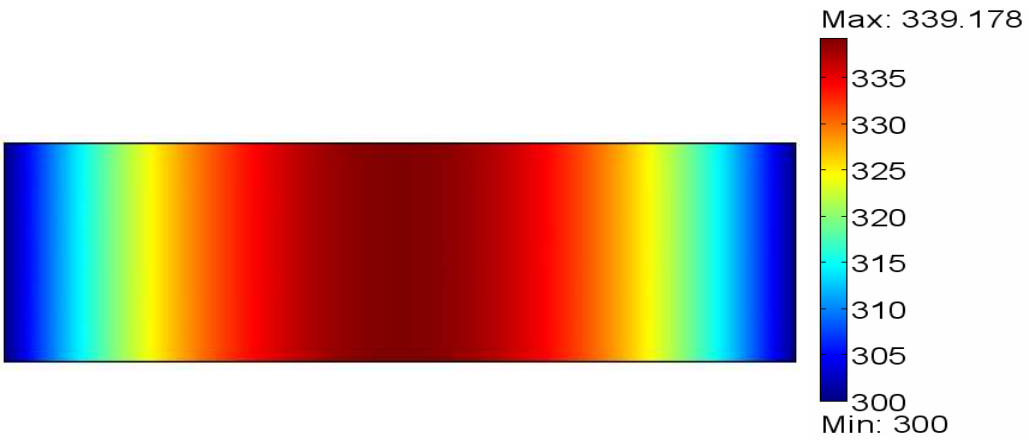

Fig. 4.8 Temperature of the graphene ribbon along the length. The thermal conductivity k_0 is equal to 5000 $Wm^{-1}K^{-1}$ and the current density is equal to 1.5 x 10^{11} A/m^2.

We also looked at how the current density affects the temperature and the resistance of the ribbon. Fig. 4.9 shows the maximum temperature (in the middle of the ribbon) as a function of the current density. Fig. 4.10 shows the resistance of the ribbon, also, as a function of the current density. The minimum value of the current density was set to 1.0 x 10^{11} A/m^2. We used 11.0 x 10^{11} A/m^2 as the maximum value for the current density. As it is seen from the plots, the thermal conductivity does not affect either the maximum temperature or the resistance as strong as the current density does; the graphs, corresponding to the uncorrected thermal conductivity values of 3500 $Wm^{-1}K^{-1}$ and 5000 $Wm^{-1}K^{-1}$ are fairly close. The current density has a profound effect on both the maximum temperature and the resistance. For example, for k_0 = 3500 $Wm^{-1}K^{-1}$ the temperature is

nearly triples by increasing approximately from 325 K to 880 K when the current density increases from 1.0 x 10^{11} A/m^2 to 11.0 x 10^{11} A/m^2. Contrary to the temperature, for the same range of the current density the resistance drops. For k_0 = 3500 $Wm^{-1}K^{-1}$ the resistance decreases by approximately a factor of three from 16.8 kOhm to 6.3 kOhm.

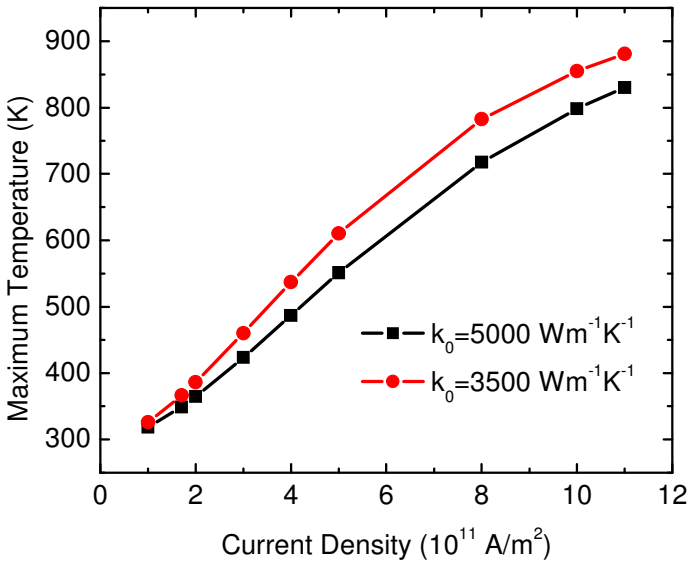

Fig. 4.9 Maximum temperature in the middle of the graphene ribbon as a function of the current density

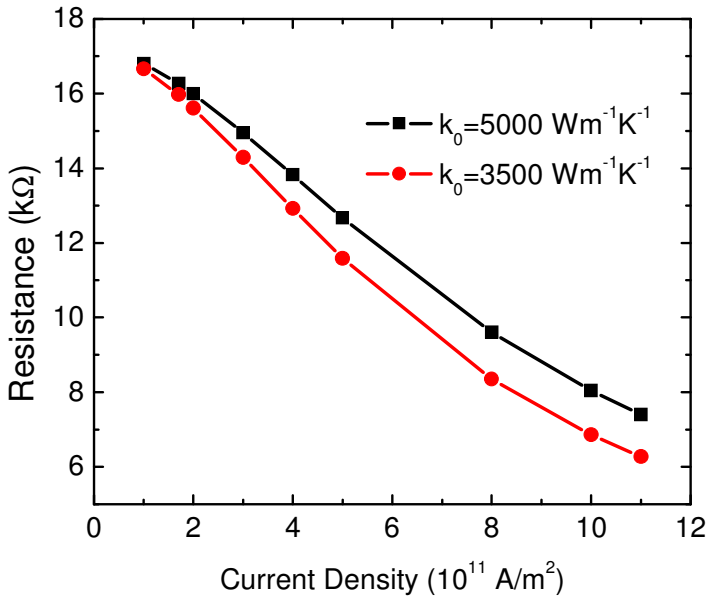

Fig. 4.10 Resistance of the graphene ribbon as a function of the current density

The breakdown current density of ~20 nm wide graphene ribbons was measured to be on the order of ~10^{12} A/m^2 [14]. If the 5 μm wide graphene ribbon breaks down at the same current density, the maximum temperature does not exceed 900 K even at the breakdown point. This maximum temperature is well below of the breakdown temperature of carbon nanofiber. That temperature was measured to be 1260 K for ~5 μm wide nanofiber, which breaks when the current density equals ~10^{10} A/m^2 [42].

We decided to investigate how the shape of the ribbon, together with the current density, affects the maximum temperature and the resistance of the ribbon. Particularly, it was interesting to see how the temperature and the resistance are modified with the changing ratio *L*/*W*. For those simulation runs the width of the ribbon was fixed to 5 μm and the uncorrected thermal conductivity of single-layer graphene was fixed to 5000 Wm^{-1}K^{-1}. Three values of the current density were studied: 1 x 10^{11} A/m^2, 2 x 10^{11} A/m^2

and 3 x 10^{11} A/m^2. Fig. 4.11 and Fig. 4.12 show the simulated maximum temperature and resistance of the graphene ribbon as functions of the length of the ribbon. The length increases from 5 μm to 20 μm. Higher current density results in higher temperature and lower resistance. The difference between maximum temperatures increases, as the ribbon becomes longer. For the 5 x 5 μm square ribbon, the maximum temperature corresponding to the 3 x 10^{11} A/m^2 current density is 35 % higher compared to the maximum temperature corresponding to the 1 x 10^{11} A/m^2. When the length reaches 20 μm, the maximum temperature with the 3 x 10^{11} A/m^2 current density is 80 % higher compared to the maximum temperature with current density of 1 x 10^{11} A/m^2. As the length of the ribbon increases, the temperature increases faster with a higher current density. When the length of the ribbon changes from 5 μm to 20 μm and the current density is 1 x 10^{11} A/m^2, the temperature increases by 45%. For the 3 x 10^{11} A/m^2 current density and the same change of the length, the temperature doubles.

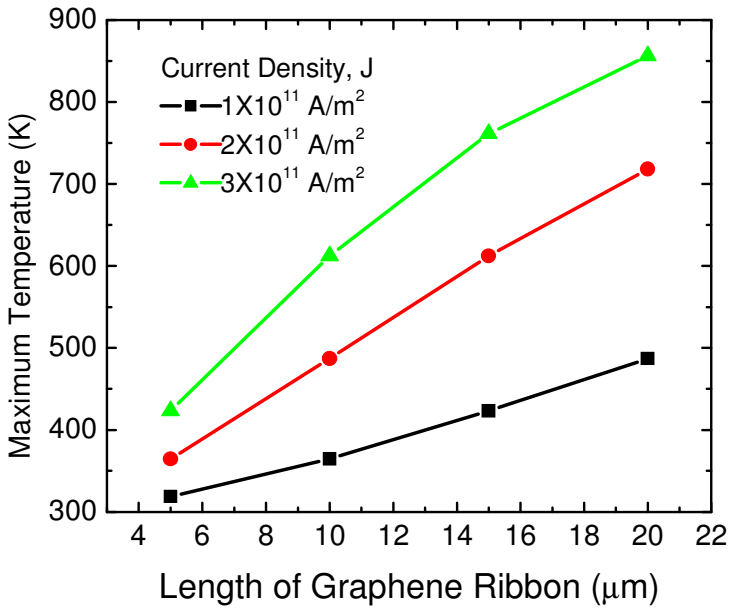

Fig. 4.11 Maximum temperature in the middle of the graphene ribbon as a function of the length of the ribbon. The thermal conductivity k_0 is equal to 5000 $Wm^{-1}K^{-1}$.

As for the resistance, it is approximately 3.2 kOhm for the all chosen current densities at L = 5 μm. When the current density is 3 x 10^{11} A/m^2, the resistance increases by 55% and tends to saturate when the length reaches 20 μm. For the 1 x 10^{11} A/m^2 current density, when the length is 20 μm, the resistance is 3.4 times higher compared to the resistance at L = 5 μm, but, as it is seen from the plot, the resistance likely saturates at longer lengths.

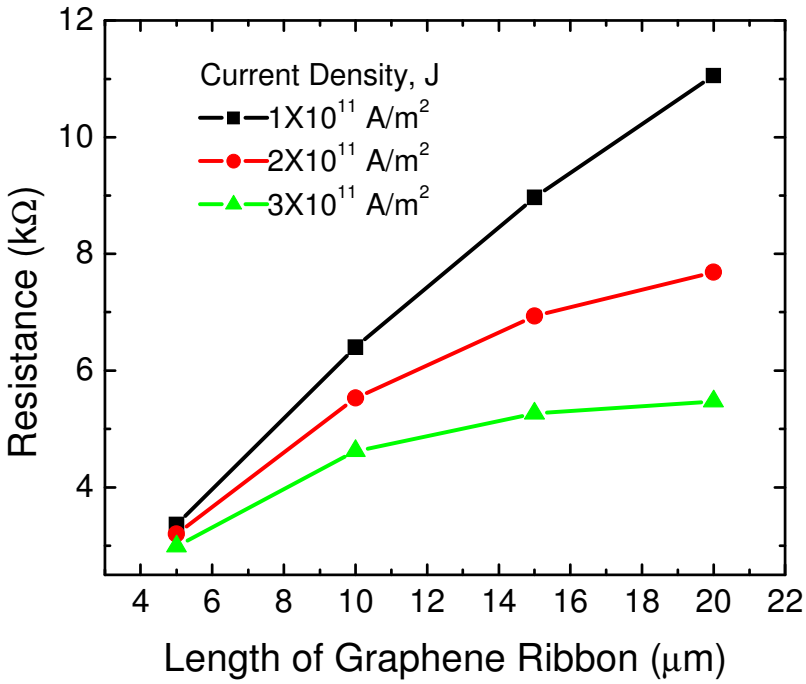

Fig. 4.12 Resistance of the graphene ribbon as a function of the length of the ribbon. The thermal conductivity k_0 is equal to 5000 $Wm^{-1}K^{-1}$

To summarize, electrical resistance of graphene, which is a semi-metal with zero band-gap [43], undergoes strong quenching as the temperature exceeds RT. Interestingly, this behavior is opposite of that manifested by some technologically important bulk semimetals such as bismuth telluride or related alloys widely used in thermoelectrics [12]. We have produced a large number of graphene layers by mechanical exfoliation from the bulk highly oriented pyrolitic graphite (HOPG) and from the high-pressure high-temperature (HPHT) grown material [44]. The single-layer graphene (SLG) and bi-layer graphene (BLG) were found with the help of micro-Raman spectroscopy through the 2D-band deconvolution procedure [7-9, 45]. We experimentally investigated the high-temperature electrical resistance of graphene single and bi-layer conductors. It was found that as the temperature increases from 300 to 500K the resistance of the single- and bi-layer graphene interconnects drops substantially. In this sense, despite being semimetal with zero-band gap, graphene resistors behave more like intrinsic semiconductors. The high-temperature normalized resistance of SLG resistor can be approximated as $R(T)/R(T=300K)=1.436 - 0.00147T$. The observed resistance quenching in graphene resistors may have important implications for the proposed applications in interconnects and thermal management. The resistance quenching in the relevant temperature rage (100-200K above RT) by 30-70% may lead to significant reduction in power dissipation.

Using COMSOL finite element analysis software, we were able to simulate direct current propagation in a single-layer graphene ribbon. Such studies are essential for design of graphene-based thermal and electrical interconnect networks. The electric conductivity in the graphene ribbon is affected by Ohmic heating. Both the maximum

temperature and the resistance of the graphene ribbon, when modified by a changing current density, weakly depend on graphene thermal conductivity, for its experimentally reported range of values. When the width and the length of the graphene ribbon are comparable, the resistance weakly depends on the current density. The resistance of the ribbon tends to saturate with the increasing current density and length of the ribbon.

References

[1] S. Ghosh, I. Calizo, D. Teweldebrhan, E.P. Pokatilov, D.L. Nika, A.A. Balandin, W. Bao, F. Miao and C. N. Lau, "Extremely high thermal conductivity of graphene: Prospects for thermal management applications in nanoelectronic circuits," Appl. Phys. Lett. 92, 151911 (2008)

[2] A.A. Balandin, S. Ghosh, W. Bao, I. Calizo, D. Teweldebrhan, F. Miao and C.N. Lau, "Superior thermal conductivity of single-layer graphene," Nano Letters 8, 902 (2008)

[3] K.S. Novoselov, A.K. Geim, S.V. Morozov, D. Jiang, M.I. Katsnelson, I.V. Grigorieva, S.V. Dubonos and A.A. Firso, "Two-dimensional gas of massless Dirac fermions in graphene," Nature 438, 197-200 (2005)

[4] J.C. Scott, J.H. Kaufman, P.J. Brock, R. DiPietro, J. Salem and J.A. Goitia, "Degradation and failure of MEH-PPV light-emitting diodes," J. Appl. Phys. 79, 2745 (1996)

[5] G. Eda, G. Fanchini and M. Chhowalla, "Large-area ultrathin films of reduced graphene oxide as a transparent and flexible electronic materials," Nature nanotechnology 3, 270 (2008)

[6] I. Calizo, A.A. Balandin, W. Bao, F. Miao and C.N. Lau, "Temperature dependence of the Raman spectra of graphene and graphene multi-layers," Nano Letters 7, 2645 (2007)

[7] I. Calizo, F. Miao, W. Bao, C.N. Lau and A.A. Balandin, "Variable temperature Raman microscopy as a nanometrology tool for graphene layers and graphene-based devices," Appl. Phys. Lett. 91, 071913 (2007)

[8] I. Calizo, W. Bao, F. Miao, C.N. Lau and A.A. Balandin, "The effect of substrates on the Raman spectrum of graphene: Graphene-on-sapphire and graphene-on-glass," Appl. Phys. Lett. 91, 201904 (2007)

[9] I. Calizo, D. Teweldebrhan, W. Bao, F. Miao, C.N. Lau and A.A. Balandin, "Spectroscopic Raman nanometrology of graphene and graphene multilayers on arbitrary substrates," J. Physics C 109, 012008 (2008)

[10] X. Wang, L. Zhi and K. Mullen, "Transparent, conductive graphene electrodes for dye-sensitized solar cells," Nano Letters 8, 323 (2008)

[11] G. Busch and H. Schade, Lectures on Solid State Physics (Pergamon Press, New York, 1976), pp. 289

[12] G. Kuka, W. Kraak, H. –J. Gollnest, R. Herrmann, "Temperature dependence of the resistivity in semimetals of the Bismuth type," Phys. Stat. Sol. (b) 89, 547 (1978)

[13] A. Seeger and K. Clausecker, "A new method for solving the Boltzmann equation for electrons in crystals," Phys. Stat. Sol. (b), 46, 137 (1971)

[14] D.S. Choi, A.A. Balandin, M.S. Leung, G. Stupian, N. Presser, S.W. Chung, J.R. Heath, A. Khitun, K.L. Wang, "Transport study of a single bismuth nanowire fabricated by the silver and silicon nanowire shadow masks," Appl. Phys. Lett. 89, 141503 (2006)

[15] F. T. Vasko and V. Ryzhii, "Voltage and temperature dependencies of conductivity in gated graphene," Phys. Rev. B 76, 233404 (2007)

[16] V. V. Cheianov and V. I. Fal'ko, "Friedel oscillations, impurity scattering, and temperature dependence of resistivity in graphene," Phys. Rev. Lett. 97, 226801 (2006)

[17] S. Mrozowski, "Electric resistivity of polycrystalline graphite and carbons," Physical Review, Vol. 77, No. 6, 838 (1950)

[18] J. M. Reynolds, H.W. Hemstreet and T. E. Leinhardt, "The electrical resistance of graphite at low temperatures," Physical Review, Vol. 91, No. 5, 1152 (1953)

[19] J. M. Skowronski, "Unusual temperature dependence of the electrical resistance of compacted CrO_3 graphite," Carbon Vol. 26, No. 5, 613-618 (1988)

[20] Standard Handbook for Electrical Engineers (McGraw-Hill, Inc., New York, 1993), pp. 4-84.

[21] T. Yagi, K. Tamano, Y. Sato, N. Taketoshi, T. Baba and Y. Shigesato, "Analysis on thermal properties of tin doped indium oxide films by picosecond thermoreflectance measurement," J. Vacuum Sci. & Tech. A: Vacuum, Surfaces, and Films 23, 1180 – 1186 (2005)

[22] A. Vassighi, and M. Sachdev, Thermal and Power Management of Integrated Circuits (Chap. 1, Springer Science and Business Media, Inc., New York, 2005)

[23] S. P. Gurrum, S. K. Suman, Y. K. Joshi and A. G. Fedorov, "Thermal issues in next-generation integrated circuits," IEEE Trans. Dev. Mater. Reliability 4, 709 (2004)

[24] Y. Joshi, K. Azar, D. Blackburn, C.J.M. Lasance, R. Mahajan and J. Rantala, "How well can we assess thermally driven reliability issues in electronic systems today?

Summary of panel held at the Therminic 2002," Microelectronics Journal, 34, 1195 (2003)

[25] A. A. Balandin and K. L. Wang, "Significant decrease of the lattice thermal conductivity due to phonon confinement in a free-standing semiconductor quantum well," Phys. Rev. B 58, 1544 (1998)

[26] A. A. Balandin, E. P. Pokatilov, and D.L. Nika, "Phonon engineering in hetero- and nanostructures," J. Nanoelectronics and Optoelectronics, 2, 140 (2007)

[27] E. P. Pokatilov, D. L. Nika, and A. A. Balandin, "Acoustic-phonon propagation in rectangular semiconductor nanowires with elastically dissimilar barriers," Phys. Rev. B 72, 113311 (2005)

[28] X. Wang, L. Zhi and K. Mullen, "Transparent, conductive graphene electrodes for dye-sensitized solar cells," Nano Lett. 8 (1), pp. 323-327 (2008)

[29] J. Wu, H. Becerril, Z. Bao, Z. Liu, Y. Chen and P. Peumans, "Organic solar cells with solution-processed graphene transparent electrodes," Appl. Phys. Lett. 92, 263302 (2008)

[30] R. Murali, K. Brenner, Y. Yinxiao, T. Beck, J. D. Meindl, "Resistivity of graphene nanoribbon interconnects," IEEE Electron Device Lett. Vol. 30, pp. 611-613, Jun. 2009.

[31] A. Naeemi and J. D. Meindl, "Conductance modeling for graphene nanoribbon (GNR) interconnects," IEEE Electron Device Lett. Vol. 28, pp. 428-431, May 2007.

[32] R. Murali, Y. Yang, K. Brenner, T. Beck, and J. D. Meindl, "Breakdown current density of graphene nanoribbons," Appl. Phys. Lett. 94, 243114 (2009)

[33] S. Hong, Y. Yoon, and J. Guo, "Metal-semiconductor junction of graphene nanoribbons," Appl. Phys. Lett. 92, 083107 (2008)

[34] D. A. Areshkin and C. T. White, "Building blocks for integrated graphene circuits," Nano Lett., Vol. 7, pp. 3253-3259 (2007)

[35] Z. Xu and Q.-S. Zheng, "Elementary building blocks of graphene-nanoribbon-based electronic devices," Appl. Phys. Lett. 90, 223115 (2007)

[36] J.-H. Chen, C. Jang, S. Xiao, M. Ishigami and M. S. Fuhrer, "Intrinsic and extrinsic performance limits of graphene devices on SiO_2," Nature Nanotech. Vol. 3, pp. 206-209 (2008)

[37] S. V. Morozov, K. S. Novoselov, M. I. Katsnelson, F. Schedin, D. C. Elias, J. A. Jaszczak, and A. K. Geim, "Giant intrinsic carrier mobilities in graphene and its bilayer," Phys. Rev. Lett. 100, 016602 (2008)

[38] http://www.comsol.com

[39] Q. Shao, G. Liu, D. Teweldebrhan, and A. A. Balandin, "High-temperature quenching of electrical resistance in graphene interconnects," Appl. Phys. Lett. 92, 202108 (2008)

[40] D. L. Nika, S. Ghosh, E. P. Pokatilov, and A. A. Balandin, "Lattice thermal conductivity of graphene flakes: Comparison with bulk graphite," Appl. Phys. Lett. 94, 203103 (2009)

[41] S. Subrina and D. Kotchetkov, "Simulation of heat conduction in suspended graphene flakes of variable shapes," J. Nanoelectron. Optoelectron. Vol. 3, pp. 249-269 (2008)

[42] H. Kitsuki, T. Yamada, D. Fabris, J. R. Jameson, P. Wilhite, M. Suzuki, and C. Y. Yang, "Length dependence of current-induced breakdown in carbon nanofiber interconnets," Appl. Phys. Lett. 92, 173110 (2008)

[43] A. K. Geim and K. S. Novoselov, "The rise of graphene," Nature Mater. 6, 183 (2007)

[44] F. Parvizi, D. Teweldebrhan, S. Ghosh, I. Calizo, A. A. Balandin, H. Zhu and R. Abbaschian, "Properties of graphene produced by the high pressure – high temperature growth process," Micro & Nano Lett. 3, 29 (2008)

[45] A.C. Ferrari, J.C. Meyer, V. Scardaci, C. Casiraghi, M. Lazzeri, F. Mauri, S. Piscanec, D. Jiang, K. S. Novoselov, S. Roth, and A. K. Geim, "Raman spectrum of graphene and graphene layers," Phys. Rev. Lett. 97, 187401 (2006)

CHAPTER 5 CONCULSIONS

Intermediate band solar cells with the efficiency exceeding Shockley- Queisser limit for a single junction cell have attracted significant attentions recently. Three-dimensional regimented array of semiconductor quantum dots, e.g. quantum dot crystal has been shown to be capable of implementing the concept of intermediate band solar cells. The strong electron wave function overlap resulting in miniband formation allows one to tune the band structure and enhance the light absorption and carrier transport. A first principles model is used to calculate the electrical properties including carrier energy dispersion, electrical conductivity, carrier density of states etc for InAs based quantum dots in GaAs based host material. By changing the size of quantum dots, inter-dot distances, barrier height, regimentation and doping level, one can tune the electric conductivity in this artificial quantum dot crystal over a wide range of values to optimize the carrier transport. Meanwhile, miniband separations and miniband bandwidth can also be engineered to optimize the photon absorption process. Detailed balance principle is used to calculate the power conversion efficiency of intermediate band solar cells. It is shown that in InAsN/GaAsSb material system one can achieve a maximum efficiency about 50% under fully concentrated sunlight. This efficiency is also confirmed by a three dimensional simulation by COMSOL for conical quantum dots.

A novel configuration of intermediate-band tandem solar cell is proposed. The light absorption and carrier transport in the structure are optimized in a way, which is different from either the conventional intermediate band solar cells or conventional tandem solar cell designs. The physical implementation of the design requires material systems with

the negligible valence band offsets and two types of the quantum dot superlattices to form the top and bottom subcells. In each subcell, the first electron mini-band is designed to be inside the potential well to act as an intermediate band, and the second or higher order mini-bands are designed to be at the edge of the conduction band of the spacer semiconductor to act as the conduction band. The maximum efficiency of ~ 61% is obtained which is much higher than that of conventional IBSC or two-gap tandem cell.

Graphene as an emerging alternative for transparent electrode in photovoltaic applications has been investigated. Single and bi-layer graphene were produced by mechanical exfoliation method from highly ordered pyrolytic graphite and high temperature high pressure graphite. Micro-Raman spectrum is used to identify the number of atomic layers. It is found that as temperature increases from 300 to 500K the resistance of the single- and bi-layer graphene electrodes drops down by 30% and 70%, respectively. The quenching and temperature dependence of the resistance are explained by the thermal generation of the electron-hole pairs and carrier scattering by acoustic phonons. The electric current propagation and effects of Ohmic heating in single-layer graphene ribbons were simulated by COMSOL. The maximum temperatures and resistances of graphene ribbons were studied as functions of graphene's thermal conductivity, electric current density and the geometry of the ribbons. Both the maximum temperature and the resistance of the graphene ribbon, when modified by a changing current density, weakly depend on graphene thermal conductivity for its experimentally reported range of values. The resistance of the ribbon tends to saturate with the increasing current density and length of the ribbon. The unique optical, electrical and

thermal properties of graphene make it a promising material for transparent electrical conductor, heat spreader as well as interconnect material for integrated circuits.